

SHAPE MEMORY NEUROENDOVASCULAR MEDICAL DEVICES FOR THE
TREATMENT AND PREVENTION OF STROKE

A Dissertation

by

ANDREA DENISE MUSCHENBORN

Submitted to the Office of Graduate and Professional Studies of
Texas A&M University
in partial fulfillment of the requirements for the degree of

DOCTOR OF PHILOSOPHY

Chair of Committee,	Duncan J. Maitland
Committee Members,	John C. Criscione
	Michael R. Moreno
	Matthew W. Miller
Head of Department,	Gerald L. Cote

December 2013

Major Subject: Biomedical Engineering

Copyright 2013 Andrea Denise Muschenborn

ABSTRACT

Stroke is a cardiovascular disease that results in the abnormal blood supply to the brain either by the lack thereof (i.e., ischemia), or hemorrhage, both causing a rapidly developing loss of brain function. It affects millions of people worldwide, resulting in long-term disability and death. This work is an effort to reduce the morbidity and mortality rates associated with stroke through the implementation of shape memory materials in the design of medical devices used in its treatment and prevention.

Shape memory materials have the ability to recover predetermined deformation upon exposure to stimuli such as heat. These volume changing capabilities make them excellent candidate materials for stroke interventions. Such interventions require the accessing of blood vessels in the brain, which over the past fifty years has shifted from a direct surgical approach, to less invasive endovascular procedures.

The majority of this work is devoted to developing an endovascular thrombectomy device for the treatment of acute ischemic stroke. This device evolves from a SMP-based device into a hybrid device made of a combination of SMP foam and nitinol. The respective increase in success rate of thrombus removal in a bench-top model was from 67% to 100%. This hybrid device is then tested in a porcine model, in which it is able to restore blood flow in an artery occluded with a thrombus nearly 3 times its working length.

In addition to being utilized as a component of the hybrid thrombectomy device, SMP foam is being investigated as an embolic aneurysm filler for the prevention of hemorrhagic stroke

because of its flow arresting properties. The rest of this dissertation deals with the characterization of such properties through the implementation of porous media theory. A system is constructed for the measurement of the porous media properties of SMP foam as well as coils mimicking the geometry of embolic coils, which are the state-of-the-art treatment of aneurysms. Results show that SMP foams impose a higher resistance to fluid flow compared to mock embolic coils, suggesting that aneurysms treated with SMP foams will have flow conditions more favorable for blood stasis than those treated with embolic coils.

Dedicado a mi gente Salvadoreña, siempre tenaz, valiente y luchadora.

Gracias por servirme de ejemplo y motivación.

ACKNOWLEDGEMENTS

None of this work would have been possible without the support and guidance from my graduate advisor, Dr. Duncan Maitland, who gave me the opportunity to be a part of this project. I am grateful for all the times he challenged and pushed me to think beyond my comfort zone. I am not the same person I used to be when I first started my Ph.D., and a vast majority of my metamorphosis was influenced by working with Dr. Maitland. Not only did he teach me about designing and fabricating medical devices, but also about the leader that I aspire to become. I would also like to thank my committee members, Drs. John Criscione, Michael Moreno and Matthew Miller, as well as our external collaborators Drs. Jason Ortega, Jonathan Hartman, Thomas Wilson and Ward Small for their contributions to this work, patience and advice.

I was fortunate to have worked with a team of such talented individuals, my Biomedical Device Laboratory peers. I am personally grateful for their camaraderie and team work, especially from the brilliant undergraduate students whom I supervised (Daniel Petty, David Szafron, Jason Szafron, Taraz Nosrat and Sara Muldoon—parts of this work are as much yours as they are mine). I would also like to acknowledge Brian Sauer, Carl Johnson and Troy Stepan for sharing their machining expertise; Barbara Slusher for always placing my orders and making sure they arrived on time; and Dr. Fidel Fernandez, Maria Pate, Barry Jackson, Andy Deuel and Dr. Julie King for their support and guidance in handling administrative affairs.

Finally, I would like to thank my family for having believed in me and for being an endless source of encouragement in all my endeavors, especially this one. Thank you to my parents for having instilled in me strength, courage, compassion, and discipline, which have been very useful tools particularly during these last four years. I am also grateful for the support and countless moments of hysteric laughter that my siblings, Ariane, Peter and Gaby have provided. Those memories brought me back to my feet numerous times when I thought I could no longer walk. I would also like to thank my nanny, Edi for her unconditional help, love and attention. Thank you to all my friends, especially The Team, Cube, Mushenys, Redroom and the 202s, for becoming my family away from home. No words can express my gratitude towards Ana and Marty Abrahams for having been the utmost catalyzers of my arrival to the United States to pursue my higher education; they changed my life. And last but not least, I would like to thank the National Institutes of Health and the state of Texas for funding.

NOMENCLATURE

BPA	Bisphenol A ethoxylate diacrylate
BzMA	Benzyl methacrylate
C	Form factor (m^{-1})
CNC	Computer numerically controlled
DMA	Dynamic mechanical analysis
DMPA	2,2-dimethoxy-2-phenylacetophenone
DSC	Differential scanning calorimetry
f	Friction factor
FDA	Food and Drug Administration
FHDD	Forchheimer-Hazen-Dupuit-Darcy
GDCs	Guglielmi detachable coils
ISA	Intracranial saccular aneurysm
K	Permeability (m^2)
LLNL	Lawrence Livermore National Laboratory
MEC	Mock embolic coil
$\frac{\partial P}{\partial x}$	Pressure gradient across porous medium (Pa/m)
PMMA	Polymethylmethacrylate
PTFE	Polytetrafluoroethylene
Q	Volumetric flow rate (m^3/s)

Re	Reynolds number
SEM	Scanning electron microscopy
SMA	Shape memory alloy
SMP	Shape memory polymer
SNF	Shape memory nitinol flower
T_g	Glass transition temperature (°C)
tPA	Tissue plasminogen activator
v_0	Darcy velocity (=Q/cross-sectional area of sample) (m/s)
η	Mock embolic coil packing density (%)
μ	Dynamic viscosity of working fluid (Pa·s)
ζ	Post-mechanical reticulation hole density of shape memory polymer foams (E+05 holes/m ²)
ρ	Density of the working fluid (kg/m ³)

TABLE OF CONTENTS

	Page
ABSTRACT.....	ii
ACKNOWLEDGEMENTS.....	v
NOMENCLATURE.....	vii
TABLE OF CONTENTS.....	ix
LIST OF FIGURES.....	xi
LIST OF TABLES.....	xiv
CHAPTER I INTRODUCTION.....	1
Need for neuroendovascular medical devices: stroke.....	2
Acute ischemic stroke.....	2
Hemorrhagic stroke.....	3
History and evolution of thrombectomy and filling devices.....	5
Current thrombectomy and filling devices.....	9
What are shape memory materials?.....	11
Purpose of research.....	14
CHAPTER II SMP THROMBECTOMY DEVICE.....	16
Introduction.....	16
Materials and methods.....	18
Polymer synthesis.....	19
Dynamic mechanical analysis.....	20
Tensile testing.....	21
Device fabrication.....	21
Device crimping.....	22
Device constrained recovery.....	23
Bench-top thrombus removal.....	24
Results.....	26
Material properties of copolymers.....	26
Device crimping.....	32
Device constrained recovery.....	33
Bench-top thrombus removal.....	34
Discussion.....	38
Conclusion.....	41

CHAPTER III SMP-SMA THROMBECTOMY DEVICE.....	43
Introduction.....	44
Design requirements	45
Design selection.....	49
Materials and methods.....	54
Proof of concept.....	54
Device fabrication.....	56
Bench-top testing.....	59
Animal testing.....	63
Results.....	64
Proof of concept.....	64
Bench-top testing.....	69
Animal results.....	75
Discussion.....	77
Conclusion.....	83
 CHAPTER IV SMP FOAM FILLING DEVICE: POROUS MEDIA PROPERTIES CHARACTERIZATION	 84
Introduction.....	84
Materials and methods.....	86
Flow system and measuring apparatus	86
Sample preparation	89
Sample characterization.....	92
Results.....	93
Discussion.....	100
Conclusion.....	102
 CHAPTER V CONCLUSIONS AND FUTURE WORK.....	 104
 REFERENCES	 109
 APPENDIX A NITINOL COMPONENT DESIGN ITERATIONS: FROM MECHANICAL NITINOL FLOWER (MNF) TO SNF	 115
 APPENDIX B POROUS MEDIA CHARACTERIZATION SYSTEM MANUAL	 123

LIST OF FIGURES

	Page
Figure 2.1. Drawing of the flower-shaped thrombectomy device designed in SolidWorks (dimensions are in mm).....	19
Figure 2.2. Sketch of custom-made apparatus for crimping compatible with Instron tensile tester (not drawn to scale).....	23
Figure 2.3. Sketch of Blockwise radial tester (not drawn to scale).....	24
Figure 2.4. Bench-top thrombotic stroke model constructed to test the feasibility of the SMP flower-shaped devices for endovascular thrombectomy. WB: water bath (37 °C); PP: peristaltic pump; TT: tensile tester (extension rate= 75 mm/min); Q; experimental flow rate (=57 ml/min); TB: Touhy Borst valve; CD: crimped device location; VM: vessel model; TP: thermocouple probe; HW: hot water syringe; DV: discharge valve; DC: discharge container.....	25
Figure 2.5. Dynamic mechanical response of four copolymers, namely storage modulus (a), loss modulus (b) and tan delta (c).....	27
Figure 2.6. Tensile properties of the four copolymers measured at each copolymer's loss modulus peak a) and tan delta peak b) temperatures.....	30
Figure 2.7. Force measurements of devices crimped at loss modulus peak temperature (a). Example of one device with 35 mole % BPA crimped at loss modulus peak temperature (scale bar= 1 mm) (b). Images taken at 2.5× magnification.....	34
Figure 2.8. Force measurements of devices crimped at tan delta peak temperature (a). One 35 mole % BPA device crimped at tan delta peak temperature (scale bar= 1 mm) (b). Images taken at 2.5× magnification. White arrow points at failure site.....	35
Figure 2.9. Recovery stress of devices during constrained recovery.....	36
Figure 2.10. Crack development in devices with 25 and 35 mole % BPA during constrained recovery test at different temperature points.....	37
Figure 2.11. Actuation and thrombus removal with 15 mole % BPA device. Q: experimental flow rate.....	38
Figure 3.1. Flower-shaped thrombectomy device off-centered after actuation. Device was painted with a black marker for better visualization.....	44

Figure 3.2.	Design concept of new hybrid thrombectomy device.	48
Figure 3.3.	Preliminary results of radial expansion of the SMP foam as a function of axial compression.	51
Figure 3.4.	SMP foams considered in the selection of the final design of the hybrid thrombectomy device.	51
Figure 3.5.	Shape recovery in 37 °C water of foams F44, F68 and F110 (n=3).	52
Figure 3.6.	Diameter expansion in 37 °C water of foams F44, F68 and F110 (n=3).	53
Figure 3.7.	Aluminum fixture for SNF shape setting.	55
Figure 3.8.	Guidewire assembly (A) showing a picture of an actual device acquired at 1.25× magnification (scale bar= 5 mm), and delivery system construction showing a crimped device inside the PTFE tube (1.25× magnification, scale bar= 5 mm) (B).	58
Figure 3.9.	Experimental setup for device-catheter friction force measurements.	62
Figure 3.10.	Bench-top thrombus removal results showing still images of thrombus removal procedure at different locations of the vessel model for devices with 1 and 2× sized SMP foams.	66
Figure 3.11.	SMP foam adhesion to bovine thrombus after being incubated in a vial filled with bovine blood for 4 minutes.	67
Figure 3.12.	Shape recovery of tungsten-doped (4% by weight concentration) SMP foams in 37 °C water.	68
Figure 3.13.	Diameter expansion as a result of axial compression and resulting compression load for tungsten-doped (concentration of 4% by weight) SMP foams while in rubbery state.	69
Figure 3.14.	Laser welding of nitinol tube and actone flat braided wire at the edge of the tube (center edge weld) (A), on the tube only without contacting the actone flat (center tube weld) (B) and at the end of the flush nitinol tube-actone flat interface (end weld) (C).	70
Figure 3.15.	Load required to pull and push the assembled device through a 5 F catheter.	71
Figure 3.16.	Load required to pull and push the assembled device through a 6 F catheter.	72

Figure 3.17.	Example of one tungsten-doped actuating SMP foam sample push experiment in water at $\sim 70^{\circ}\text{C}$.	73
Figure 3.18.	Average force required to push three actuating tungsten-doped SMP foam samples (6 mm diameter, 5 mm length) through the 18 AWG lightweight wall, medical grade PTFE tube.	74
Figure 3.19.	Control angiogram prior to injecting the clot (A) and after the clot was injected followed by contrast (B) (white arrows point at blood clots). Deployed device distal to the clot (C) (arrow points at SNF and actuated SMP foam), and device-clot interface during removal (D-F).	76
Figure 4.1.	Flow system constructed to measure the pressure gradient across SMP foam and MEC samples for a given flow rate range.	88
Figure 4.2.	Exploded view of SMP foam chamber with arrows showing how pieces are assembled (A) and assembled MEC chamber (B).	88
Figure 4.3.	SMP foams prior to mechanical reticulation ($2.5\times$ magnification) and true-scaled overlaid illustrations of the four scenarios of mechanical reticulation and their corresponding hole densities.	91
Figure 4.4.	Pattern of holes pierced in each of the four scenarios of mechanical reticulation.	91
Figure 4.5.	Packed MECs in measuring chamber.	92
Figure 4.6.	Pressure gradient versus Darcy velocity (v_0) of SMP foam S (a) and L (b) (hole density (ζ) with units $\text{E}+05$ holes/ m^2).	94
Figure 4.7.	Pressure gradient versus Darcy velocity (v_0) of MECs (packing density (η)).	96
Figure 4.8.	Permeability of SMP foams and MECs.	98
Figure 4.9.	Form factor of SMP foams and MECs.	99
Figure 4.10.	Friction factor versus Re for SMP foam samples and MECs.	100

LIST OF TABLES

	Page
Table 2.1. Rubbery modulus and mechanical transition temperature values.	29
Table 2.2. Average stress-at-failure, strain-to-failure, and toughness at loss modulus peak and tan delta peak temperatures ery modulus and mechanical transition temperature values.	32
Table 3.1. Summarized design inputs for hybrid thrombectomy device.	48
Table 3.2. Properties of SMP foams.	52
Table 3.3. Laser welding parameters for the assembly of nitinol components.	60
Table 3.4. Performance specifications and verification tests for the SMA-SMP thrombectomy device.	80

CHAPTER I

INTRODUCTION

Stroke is a disease of the neurovasculature that affects 15 million people in the world each year, making it the second most common cause of death and the leading cause of adult long-term disability [1-3]. Over the last century, its treatment shifted from a direct surgical access approach to a less invasive endovascular method, thanks to parallel growth in the fields of imaging and materials science [4, 5]. The endovascular method exploits the interconnected nature of our vascular system, which enables the delivery of drugs and navigation of devices via a catheter inside the blood vessels. Therefore, the design and fabrication of neuroendovascular devices is challenging primarily because of the size constraints imposed by the catheter delivery of a device from the groin area to the brain. Shape memory materials can exhibit the volume changes necessary for catheter delivery because they have the ability to store a temporary shape and recover their primary shape when exposed to a stimulus, which makes them ideal materials for neuroendovascular devices.

While there has been progress in the endovascular treatment and prevention of stroke, areas of improvement remain. The reason is because the mortality and morbidity rates, as well as the cost associated with this disease remain high. In 2009, the U.S. indirect and direct costs due to stroke were estimated at \$68.9 billion and increased to \$73.3 billion by 2010 [6]. General knowledge of the etiology, pathophysiology and complications of stroke is necessary to comprehend the need for improved neuroendovascular medical devices for its treatment and prevention.

Need for neuroendovascular medical devices: stroke

Stroke is the rapidly developing loss of brain function due to abnormal blood supply to the brain tissue. It can be caused by a blockage in the blood flow resulting in ischemia—lack of oxygen and glucose supply—or by a hemorrhage. Depending on the cause, stroke is classified into two types: acute ischemic stroke and hemorrhagic stroke.

Acute ischemic stroke

The loss of blood supply to the brain tissue due to a blockage in an artery of the neurovasculature by a thrombus or embolism is called acute ischemic stroke. This type of stroke comprises 85% of all stroke cases in the U.S. [2, 7]. It is an etiological heterogeneous disease and common risk factors are hypertension, diabetes mellitus, hyper cholesterolemia, cigarette smoking, oral contraceptive and high alcohol intake, and for the most part, atherosclerosis [6, 8-10]. This heterogeneity renders young adults, ages between 15 and 45, also susceptible to this disease. In fact, they comprise 2-12% of the cases in western countries. The most common risk factors for this group are non-atherosclerotic vasculopathies, i.e., migraine, dissection of extracranial arteries, HIV, and drug abuse; cardioembolisms, e.g., due to mitral valve disease and patent foramen ovale; atherosclerosis and other hematological disorders [11]. Given that atherosclerosis is a major contributor to the pathophysiology of ischemic stroke, it is not surprising that infection and inflammation are also linked to ischemic stroke, particularly in younger populations [8]. Additionally in developing countries, neurocysticercosis, cerebral malaria, tuberculosis and infective endocarditis are infectious diseases considered to cause ischemic stroke [12].

Approximately every minute in the U.S. a person experiences an ischemic stroke each year. Of all cases, 8-12% are fatal. Of those who survive, 50% have some hemiparesis, 30% are unable to walk without assistance, 19% have aphasia, and 26% are institutionalized [6]. The degree of brain damage is strongly related with the amount of time that the brain is in ischemic state. For example, each hour the ischemic brain remains untreated, it loses as many neurons as in 3.6 years of normal aging [13]. Likewise, the success of the treatment by the only drug approved by the Food and Drug Administration (FDA), tissue plasminogen activator (tPA), is limited by time. TPA can only be administered to those patients who arrive at the hospital within 4.5 hours of stroke onset. Because of this treatment time window and other exclusion criteria, only 2-5% of the patients are eligible to receive it [14].

The limited patient eligibility for treatment with tPA is largely responsible for the need of mechanical thrombectomy devices. More information about the history of these devices and the devices that are currently on the market will be provided in the following sections. For now, let us finish our brief overview on stroke.

Hemorrhagic stroke

It is estimated that 5 to 15% of all strokes are caused by the rupture of intracranial aneurysms resulting in hemorrhagic stroke [15]. Intracranial aneurysms are vascular malformations characterized by abnormal dilatations of the intracranial arteries. Depending on their shape, they can be classified into saccular or fusiform. Intracranial saccular aneurysms (ISAs) account for 90% of all intracranial aneurysms and are balloon-shaped, while fusiform aneurysms take on an elongated spindle-shape [16]. Fusiform lesions usually remain

asymptomatic until they press on adjacent tissue. Saccular lesions, on the other hand, become symptomatic after they rupture resulting in spontaneous subarachnoid hemorrhage (SAH). Although the rupture potential of aneurysms is only between 0.1-1.0% per year, the consequences when they do rupture are devastating. Approximately 35 to 50% of the patients die, and of those who survive, 50% regain functional independence, while 30% are permanently disabled and 20% require institutional care [17-19]. Because there is a much higher prevalence and fatality rates associated with saccular lesions compared to fusiform lesions, the remainder of this work will primarily focus on ISAs.

ISAs develop in or near bifurcations of the primary network of arteries that supply the brain with blood, called the circle of Willis. The majority form in the anterior circulation, particularly in the anterior communicating artery, the internal carotid artery at the posterior communicating artery origin and the middle cerebral artery (MCA) bifurcation. The most common site in the posterior circulation is the basilar artery bifurcation [20].

There is little agreement on the pathogenesis of ISAs; however, major role players are: distinct geometrical features of the cerebral vasculature, genetic and environmental risk factors and hemodynamics. The most relevant geometrical features of the cerebral arteries that may contribute to the initiation of ISAs are the lack of an external elastic lamina, scarcity of elastin in the media, and structural irregularities at the apex of vessel bifurcations [20]. Among the environmental and genetic risk factors are hypertension, smoking, and gender. Finally, hemodynamics plays a role in the growth and remodeling of ISAs because it affects

mainly the regulation of protease activity and collagen production within the aneurysm wall [18, 21-23].

With a general understanding of the causes and consequences of stroke, we will move onto a brief history of the devices that have been developed in an attempt to treat and prevent this disease.

History and evolution of thrombectomy and filling devices

The surgical treatment of vascular lesions of the head and neck began in the early 20th century. This was a time during which an array of different treatment techniques were attempted [4]. Some techniques were more successful than others; however, all of them in some way laid the groundwork for the conception and development of the devices that are used today.

The beginning of the 20th century was marked by the development of different clips coated with thrombogenic materials intended to slowly occlude the patent vessel of a vascular malformation (i.e., cerebral aneurysm, fistula or arteriovenous malformation) to prevent its future rupture. The Neff clamp, developed in 1904, was one of such first devices. The main feature of this device was that the clamp's rubber bands, which were responsible for the squeezing action, were coated with absorbable catgut for a slow yet progressive occlusion of arteries [4, 24]. While this device intended to isolate the vascular malformation by “extra” vascular means (i.e., clipping), there were also efforts to achieve this by surgical “intra”

vascular means (i.e., filling). The first such attempt took place in 1930 when Brooks implanted harvested muscle inside a carotid-cavernous fistula. This procedure laid the foundation for the much later development and progression of surgery that was more focused on less invasive and intravascular approaches [25]. However, until then, clamping methods continued to be developed. In 1937 Walter Dandy placed a silver clip at the base of an aneurysm, an effort which marked a new era in the surgical treatment of cerebrovascular malformations [26, 27].

While surgical clipping became the standard for the treatment of cerebral aneurysms, much work was done to find alternative ways of embolizing vascular malformations similar to Brooks' attempt. By the 1960s, different particulates and materials had been explored as potential filling agents, ranging from methylmethacrylate spheres and metal pellets to horse hair [28-30]. Additionally, the feasibility of utilizing magnets for the endovascular navigation of metallic pellets as well as the use of direct current for thrombosis were explored [31-35].

Up until this point, significant advancements had been made in the development of devices and treatment methods for vascular malformations such as aneurysms, fistulae and arteriovenous malformations. On the contrary, this was not the case for the development of treatment techniques for cerebrovascular occlusions. In 1961, Dr. Wolff, professor of Neurology, raised the following statement during the Princeton Conference on Cerebrovascular Disease [36]:

“Surgeons have made rapid and dramatic advances in the treatment of people with occlusive vascular diseases in the upper chest and neck. Perhaps we could encourage them to think of ways of going inside the head and modifying the circulation there, for at present even those individuals who have occlusive disease in the vertebral canal are not surgically approachable.”

The concept of revascularization (i.e., the re-establishment of blood flow in an occluded vessel) was introduced in the early 1950s, when Dr. Henschen, professor of Surgery at the University of Basel in Switzerland, transplanted a graft of temporalis muscle to the cerebral cortex of a patient with bilateral carotid stenosis [37]. The years that followed were marked by numerous attempts of revascularizing ischemic areas of the brain by different surgical means. Examples include the development of collateral circulation by a graft, the reversal of cerebral circulation by carotid-jugular anastomosis, and the resection of the thrombosed portion of the vessel followed by its replacement by a vascular graft [38]. Unfortunately, all of these surgical approaches had little success, suggesting that the missing link in the successful surgical treatment of cerebrovascular occlusions was the ability to access occluded vessels by means of endovascular navigation.

Endovascular navigation was not possible until the capability to visualize the vascular tree in real time was available. Therefore, it is not surprising that true catheter-based approaches did not begin until the 1960s, when catheter-cerebral angiography was brought to America, nearly thirty years after being developed in Europe [4, 39, 40]. This decade was a revolutionary period of great technological advancements in endovascular neurosurgery.

In the following decades, the endovascular approach became the gold standard for the treatment of cerebrovascular lesions. However, specifically for the revascularization of

thrombotic occlusions, this did not happen until the early 21st century. The 1970s was characterized by the competency to highly purify proteins for biochemical studies, which enabled the exploration of biochemical means of dissolving thrombi, also known as thrombolysis. Although it was known since 1947 that animal tissues contain an agent that can activate plasmin, it was not until the late 1970s that tPA was discovered to be fibrin-specific. This rendered tPA as superior compared to other available non fibrin-specific plasmin activators (e.g., urokinase and streptokinase) for thrombolytic therapy, given that thrombi are rich in fibrin [41]. Based on these facts and numerous other clinical studies, the FDA approved tPA in 1996, and up to date, it remains as the only FDA-approved drug for the treatment of acute ischemic stroke [42].

The treatment of vascular malformations on the other hand, never took a pharmacological route. Instead, the area of exploration focused on endovascular filling devices. A major breakthrough in the history of endovascular filling devices was the insertion of platinum coils into a cerebral aneurysm in the late 1980s by Hilal et al. [43]. This technique was modified by Guido Guglielmi, who collaborated with Target Therapeutics to launch the first generation of electrolytically detachable coils, also known as Guglielmi Detachable Coils, (GDCs) in 1990 [4]. GDCs are still in the market and they are the precursors of the multiple variations of embolic coils that are commercially available up to present.

Current thrombectomy and filling devices

Current thrombectomy devices used in the neurovasculature and peripheral circulation can be classified into 5 major types: snare devices (e.g., Amplatz Goose Neck Snare, ev3, California), laser-based systems (e.g., Endovascular Photo-Acoustic Recanalization System, EndoVasix Inc., California), ultrasound-based devices (e.g., MicroLysUs Catheter, EKOS Corp., Washington), retrieval devices (e.g., Merci Retriever®, Stryker, California), and aspiration devices (e.g., AngioJet, Possis Medical Inc., Minnesota). Some use a combination of two or more types, like the Penumbra System® (Penumbra Inc., California), which mechanically disrupts and aspirates the fragmented thrombus [2]. The majority of these have not made it past the research and development stage, and some are used off-label.

The first thrombectomy device to get cleared by the FDA for the treatment of acute ischemic stroke was the Merci Retriever® in 2004. This device primarily consists of a nitinol wire of approximately 50 mm in length, with a pre-programmed corkscrew shape. Its 510(k) application was based on a series of devices that in turn, were cleared based on substantial equivalence to precursor devices. Some of these precursor devices include the Concentric Retriever (Concentric Medical, California) and the Attractor Endovascular Snare (Target Therapeutics, California), both intended for the removal of emboli and foreign bodies in distal peripheral vessels [44]. Four years after the launch of the Merci Retriever®, a second device got 510(k) clearance. This device was the Penumbra System®, which consists of a separator at the tip that disrupts the thrombus as it is moved back and forth, and suction applied to the catheter to aspirate the thrombus fragments. The devices that followed were very different from the aforementioned ones, primarily because they took on a stent-like

shape. These were the SolitaireTM FR (ev3, California) and the Trevo[®] (Stryker, California), which were cleared to market in 2012. Both of these are self-expandable nitinol stents roughly 30 mm long.

Stents are not only used in the treatment of acute ischemic stroke, but they are also used to treat hemorrhagic stroke. They are usually placed in the parent artery across the neck of the aneurysm, generally when the aneurysm has a wide neck (i.e., when the aneurysm neck opening diameter is greater than the dome diameter), either by themselves or along with an aneurysm filler [45]. Stents provide important stabilization to the parent vessel and to the filler as they prevent it from potentially migrating out of the aneurysm dome. Examples of commonly used nitinol stents for this application include the NeuroformTM (Stryker, California), the EnterpriseTM (Cordis, Florida), and the WingspanTM (Stryker, California).

There are different types of aneurysm fillers, including embolic liquids (e.g., Onyx[®], ev3, California), embolic particles (e.g., Embozone[®] Microspheres, CeloNova Biosciences, Texas), and embolic coils. Helical platinum coils are now the standard for endovascular treatment of aneurysms and other malformations [5]. When the first version of platinum embolic coils were developed, platinum was the material of choice primarily because of its sensitivity to low electrical current, which made them easily detachable from steel guidewires. Additional reasons were that platinum is a soft metal that can be easily bent, it has been shown to recover its shape, and is biocompatible when implanted [46]. However, significant changes have been made to the design of embolic coils in order to increase treatment success rates. Some of these changes involve the design of non-helical, complexly

shaped coils (e.g., GDC® 360° (Stryker, California)) and the addition of polymer coatings in order to increase the bioactivity of the coils and their filling capacity.

Despite the improvements that have been made to embolic coils up to date, there are still challenges and complications that arise from their use in the treatment of aneurysms. The most important are impartial filling of the aneurysm resulting in low coil packing densities, coil compaction over time, and coil migration to the parent artery [47-49]. For example in aneurysms with diameter greater than 10 mm the maximum packing density is usually below 24% [50]. Likewise, the thrombectomy devices that are commercially available have limitations. Major ones are poor device flexibility and thrombus hold during thrombectomy, but more importantly, restricted placement due to the length of some devices required to be advanced past the thrombus [2, 51-53]. In order to overcome these challenges, researchers are investigating shape memory materials with superior volume expansion capabilities than the ones that are used in available devices up to date. In the next section, a general overview of what shape memory materials are is given, and the two shape memory materials that were used in the devices presented in this work are introduced.

What are shape memory materials?

Shape memory materials, or smart materials, possess the ability to store a temporary shape(s) and then actuate to a primary geometry upon exposure to stimuli such as electric field changes, heat or moisture [54-58]. This phenomenon is called the shape memory effect, and it is exhibited by certain classes of ceramics, alloys and polymers. In ceramics, such as the

ones based on antiferroelectric lead zirconate titanate for example, the shape memory effect is triggered by electric field-induced phase transitions. Shape memory ceramics generate recovery forces of roughly 100 MPa and are characterized by responses on the order of milliseconds and strains on the order of 10^{-3} mm/mm [57]. Thus, these materials are excellent candidates for applications requiring a fast response and only one small strain state such as for latching relays, where the ceramic is capable of maintaining the “on” state even without the recurring application of electricity [57].

Shape memory alloys (SMAs) have two phases that correspond to the structure of their atoms. The first one is the high-temperature austenite or parent phase (characterized by a cubic crystal structure) and the second one is the low-temperature martensite phase with a lower symmetry. The atomic movement from one phase to the other triggered by temperature and stress changes is what results in the shape memory effect in these type of smart materials. Phase transformation takes place when the free energy difference between the two phases reaches a critical value [58]. When the temperature of the SMA decreases below its martensitic transformation temperature, the atoms move in a cooperative and shear-like manner resulting in the so called martensitic transformation. As a result, the crystal structure changes into the twinned configuration. If a load is applied to the material in the twinned configuration while at a low temperature, detwinning occurs and the material retains its deformed (or secondary) shape even after the load is removed. If the material is heated to a temperature above the austenitic transformation temperature, the crystal structure returns to the parent phase and the original shape is recovered [58].

In addition to the shape memory effect, SMAs also possess pseudoelastic capabilities, i.e., the ability to transform from one phase to another as a result of induced stress at a constant temperature [57, 58]. When a load is applied to the SMA while in the austenitic phase (at a temperature above the martensitic transformation temperature), it can result in the direct transformation to the detwinned martensite if the induced stress is above a certain threshold. However, the martensite is not stable at temperatures above its transformation temperature, which is why when the load is removed, the crystal structure transforms back to the austenite and the original shape is recovered. This effect is responsible for the ‘spring-like’ behavior of SMAs, which is limited by a maximum strain, above which plastic deformation occurs [59]. Examples of SMAs are AgCd, AuCd, CuAlNi, CuAlBe, CuSn, CuZn, NiAl, and NiTi. NiTi, also called nitinol in honor of the Naval Ordnance Laboratory (NOL) where it was discovered in the 1960s, is characterized by recoverable forces of approximately 1000 MPa and strains on the order of 10^{-1} mm/mm [57, 59].

The last type of smart materials that we include in this section are shape memory polymers (SMPs). The term ‘polymer’ refers to a molecule made by repeating units of monomers. Polymers are viscoelastic, which means that they exhibit the combined viscous and elastic responses of materials that behave intermediately between liquids and solids when a stress is applied, like Silly Putty [57, 60]. For example, when Silly Putty is formed into a ball and then left in a container for a long period of time, it will flow to conform to the shape of the container, dissipating energy (viscous response). Conversely if it is rapidly stretched and one end is released, it will partially return to its original dimensions as a result of the temporary energy storage (elastic response) [60].

Thermoplastic polymers with physical crosslinks and thermoset polymers with chemical crosslinks have the ability to exhibit shape memory [61]. When these materials are heated above their glass transition temperature (T_g), their polymer segments undergo conformational motion that enables mechanical deformation into a secondary metastable state when a load is applied [54, 56]. As the temperature is lowered, the rearranged intermolecular conformations are locked and the new shape is fixed. Heating the material above T_g provides the system with activation energy that enables polymer chain mobility. The polymer chains relax back to their original geometry in an attempt to minimize free energy, which results in the recovery of the material's primary shape [61]. SMPs are characterized by the ability to tune their thermomechanical properties to meet specific application demands. However, they have been reported to exhibit maximum recoverable forces less than 1/100 times those reported for SMAs, with maximum strains on the order of 10 mm/mm [54, 57, 61].

The aforementioned properties of SMAs and SMPs make them excellent candidate materials for applications requiring high volume expansion and high recovery force. One such application is the catheter delivery and subsequent actuation of the neuroendovascular devices developed in this work. Thus, these devices benefit from the use of each, and the combination, of these two types of shape memory materials.

Purpose of research

Through this work we intend to contribute to the improvement of the neuroendovascular treatment and prevention of stroke via the characterization and implementation of SMPs and

SMA as components of neuroendovascular devices. The next two chapters document the design process of a thrombectomy device, which starts with a design involving SMP alone, and evolves to a hybrid design that explores the combination of SMP foam and SMA. The penultimate chapter describes the experimental measurement of the porous media properties of the new SMP foam embolic aneurysm filler that is being developed in the Biomedical Device Laboratory for the treatment of ISAs.

CHAPTER II

SMP THROMBECTOMY DEVICE

In 2007, scientists at Lawrence Livermore National Laboratory (LLNL) developed a corkscrew-shaped thrombectomy device made of a commercially available thermoplastic SMP (MM5520, DiAPLEX Company, Ltd., a subsidiary of Mitsubishi Heavy Industries, Ltd., Tokyo, Japan). The device was successfully delivered by a catheter, but encountered two problems upon testing in a rabbit animal model [62]. First, similar to previously mentioned commercially available devices, the portion of the device required to be advanced past the thrombus was too long and thus limited device access. As a result, the same group at LLNL proposed a flower-shaped SMP thrombectomy device. The new design reduced the deployment length to less than half of that required by commercially available mechanical thrombectomy devices [63]. However, the second problem was related to the recovery force of the corkscrew device, as it was not sufficient to achieve complete actuation when the device was pushed against the vessel wall.

This chapter presents the results of a study in which a thrombectomy device, modeled after the flower-shaped design developed at LLNL, was fabricated from crosslinked thermoset acrylic SMP. The goal was to evaluate different crosslink densities to tailor the thermomechanical properties that would result in the highest achievable recovery force.

Introduction

While the SMP-based flower-shaped thrombectomy device exhibited limited recovery force, the ability to tune the thermomechanical properties including modulus and recovery stress of

SMPs offered a solution to this problem. One effective, demonstrated way of tailoring thermomechanical properties of SMPs is controlling crosslink density [64, 65]. Increasing crosslink density of SMP systems has been generally shown to increase recovery stress, which is desirable for thrombectomy devices because it reduces the likelihood of incomplete shape recovery, which could result in thrombus dislodgement [56, 66, 67]. Acrylate assemblages provide a stable backbone that allows the incorporation of chemical crosslinks into the polymer matrix by varying the ratio of linear builder (monofunctional monomer) to crosslinker (multi-functional monomer). However, the caveat of increasing crosslink density for this type of materials is that it also results in unfavorable changes such as increased brittleness and decreased strain capacity [64].

The objective of this study was to fabricate a set of SMP-based thrombectomy devices that offered improved access and thrombus hold than comparable available devices. To improve device access we selected a design that reduced the length required to go beyond the thrombus, such as the flower-shaped design developed at LLNL [63]. We incorporated chemical crosslinks into the polymer structure to improve thrombus hold via increasing the device recovery stress. However, increases in recovery stress come at the expense of reduced strain capacity, which is particularly important for devices that undergo large deformations. For our desired applications, these large deformations were required for catheter delivery, and consisted of crimping the device to a cylindrical shape and then actuating it back to its primary flower-shape. Since arteries of stroke patients are generally diseased and therefore stiffer than healthy arteries, we tested the recovery force of the devices under constrained conditions. As such, this work investigates the thermomechanical performance of the

devices with various material properties during crimping and constrained recovery. We took the following approach:

- i. Designed a system of cross-linked acrylate SMPs with varying rubbery moduli;
- ii. Machined devices and measure the forces required for crimping and constrained recovery; and
- iii. Performed thrombus removal experiment in a bench-top thrombotic model to determine the success rates of the proposed devices.

Materials and methods

All the devices have the same design, which is illustrated in Figure 2.1. After thrombectomy devices were CO₂ laser machined, they were subjected to custom device-specific experiments, in which the forces required to crimp the devices at two temperatures (DMA loss modulus peak, theoretical maximum toughness, and tan delta peak, theoretical maximum strain) and the recovery forces of the devices under constrained conditions were measured [60, 68].

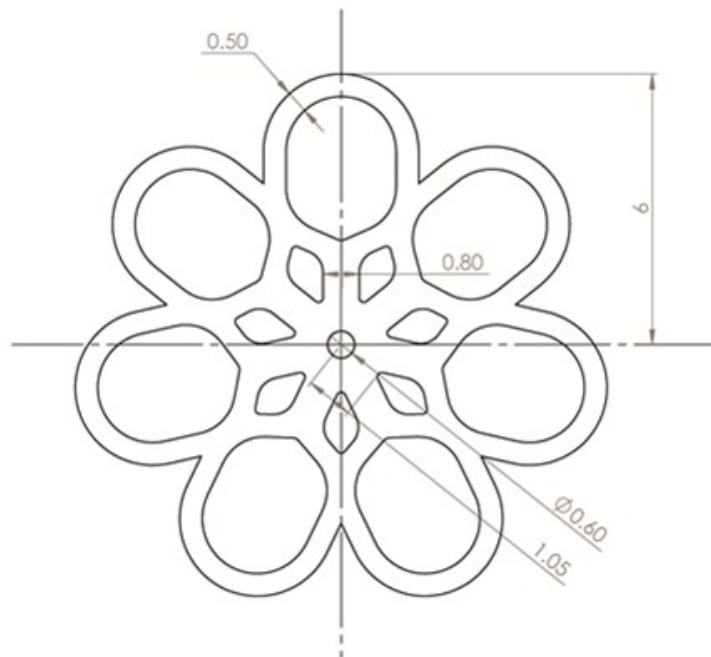


Figure 2.1. Drawing of the flower-shaped thrombectomy device designed in SolidWorks (dimensions are in mm).

Polymer synthesis

We prepared four thermoset acrylic copolymers containing the monomer benzyl methacrylate (BzMA), the crosslinker bisphenol A ethoxylate diacrylate (Mn~512, BPA), and the photoinitiator 2,2-dimethoxy-2-phenylacetophenone (DMPA). All three chemicals were purchased from Sigma Aldrich and used as received without further purification. This monomer and difunctional crosslinker combination, which is similar to that reported by Safranski, et al. (2008), was selected because it enables the synthesis of a series of SMPs with tailorable crosslink densities and glass transitions above body temperature in the range of 65 to 75 °C. BzMA was also selected because Safranski, et al. demonstrated that

poly(benzyl methacrylate) thermoset SMPs have higher toughness than numerous other thermoset acrylics [69].

The four compositions contained 5, 15, 25 and 35 mole % BPA and 0.5 wt. % DMPA and were prepared in 51×76×0.4 mm sheets by bulk UV curing. After massing, the monomer, crosslinker and photoinitiator mixtures were injected between 51×76 mm glass slides coated with Rain-X and separated by 0.4 mm spacers. These slides were cured for 99 minutes using 365 nm UV irradiation inside a UVP CL-1000 crosslinking chamber. The cured thermoset films were then post-cured at 130 °C with vacuum at 1 torr for 12 hours and subsequently stored under desiccation.

Dynamic mechanical analysis

Dynamic Mechanical Analysis (DMA) experiments were carried out in tension using a TA Instruments Q800 dynamic mechanical analyzer in 4×30×0.4 mm rectangular specimens (n=5). The rectangular specimens were machined with a 40 W Gravograph LS100 CO₂ laser machining device using a 38.1 mm lens, a speed setting of 5, a power setting of 10, and a laser resolution of 1200 dots per inch. Specimens were cleaned with a methanol damp Kimwipe and dried at 90 °C prior to being tested and subsequently stored under desiccation. DMA experiments were carried out from -20 to 140 °C in the DMA Multi-Frequency/Strain instrument mode utilizing a frequency of 1 Hz, a strain of 0.1%, a preload force of 0.01 N, a force track of 150%, and a heating rate of 2 °C/min. Data were recorded using TA Instruments Q-series software and analyzed using TA Instrument Universal Analysis software.

Tensile testing

Uniaxial tensile testing experiments were conducted to failure on ASTM Type V dog bone samples (n=5) using a dual-column Instron model 5965 tensile tester with a 500 N load cell, 1000 N high temperature pneumatic grips, and a temperature chamber thermally controlled by forced convection heating. The dog bone samples were cut using the Gravograph LS100 CO₂ laser cutter with the same instrument parameters used in the machining of DMA specimens. Specimens were cleaned with a methanol damp Kimwipe and dried at 90 °C under vacuum at 1 Torr prior to being tested and subsequently stored under desiccation. Specimen deformation was measured optically using an Instron Advanced Video Extensometer with a 60mm field-of-view lens. Specimens were heated to target temperatures under zero load (unclamped bottom grip) and held isothermally for 30 minutes to allow for thermal equilibrium to be reached. The bottom grip was then clamped, and the strain-to-failure experiments were subsequently begun using a deformation rate of 10 mm/min. Data were recorded utilizing Instron Bluehill 3 software.

Device fabrication

The post-cured 51×76×0.4 mm sheets of the four different copolymers were cut with the flower-shape design pattern (Figure 2.1) using the Gravograph CO₂ laser machining device with the same parameters used to cut the DMA specimens. Machined devices were carefully cleaned with a methanol damp Kimwipe and dried at 90 °C under vacuum at 1 Torr prior to being tested, and subsequently stored under desiccation.

Device crimping

A custom fixture compatible with the Instron tensile tester was fabricated with a mini computer numerically controlled (CNC) milling machine (MDX540, Roland). As depicted in Figure 2.2, it consisted of a removable portion fabricated from polytetrafluoroethylene (PTFE) with a funnel-like geometry on the inside, and a stationary portion made of poly(methyl methacrylate) (PMMA) that attached to the bottom pneumatic grip of the tensile tester. The maximum diameter of the funnel was 12.5 mm and it contracted gradually to 3.5 mm (the portion with the smallest diameter is 1 cm long and served to fit the crimped device and allow it to cool down). The stationary portion had a cap with a 0.3 mm hole machined with an excimer laser (RapidX, Resonetics) that helped center the wire that held the devices throughout the crimping process. This wire had roughly a 2 mm diameter ball of 96.5 Sn 3.5 Ag solder (Indium Corporation) at the tip to hold the devices as they were pulled during crimping. By inserting a thermocouple inside the funnel of the assembled crimping fixture, it was determined that in order to achieve the target temperature inside the funnel within 45 minutes, the temperature chamber was required to be set 4 °C higher. Thus, devices were allowed to thermally equilibrate inside the funnel for a minimum of 1 hour prior to testing. The tensile tester had a 50 N load cell (resolution of 0.00025 N) and was set to extension mode at a strain rate of 5 mm/min. Data were recorded using Instron Bluehill 3 software. The crimping experiments were performed at temperatures corresponding to the mechanical transition temperature of each copolymer's composition (n=5).

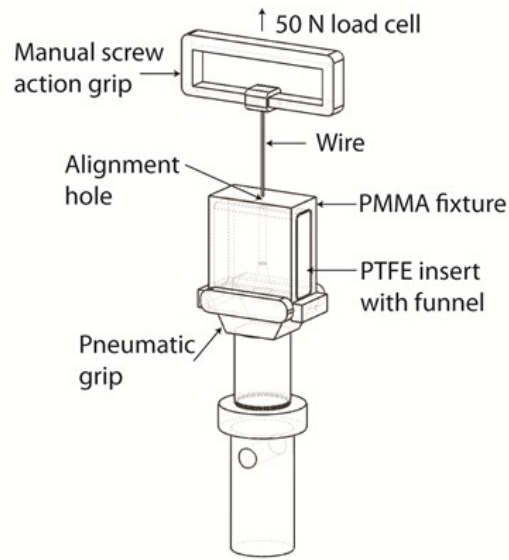


Figure 2.2. Sketch of custom-made apparatus for crimping compatible with Instron tensile tester (not drawn to scale). The device is inserted in the PTFE insert through the funnel, and as it is displaced upwards by the crosshead, it gets crimped to a cylindrical shape.

Device constrained recovery

A radial tensile tester (Blockwise Engineering), also compatible with the Instron tensile tester, was utilized to perform constrained recovery measurements of the crimped devices (see Figure 2.3). The radial tester temperature was ramped from 30 °C to 55 °C and the recovery force of the devices that had been successfully crimped was measured at 1 Hz using Instron Bluehill 3 software. A thermocouple was installed in close proximity of each device, and temperature was also recorded at 1 Hz using LabView. The diameter of the radial tester was kept constant at 3.75 mm after setting it with a high accuracy gage pin. The blade heating effects of the radial tester were accounted for by subtracting data measured with the empty tester from the data of all devices for the same temperature range.

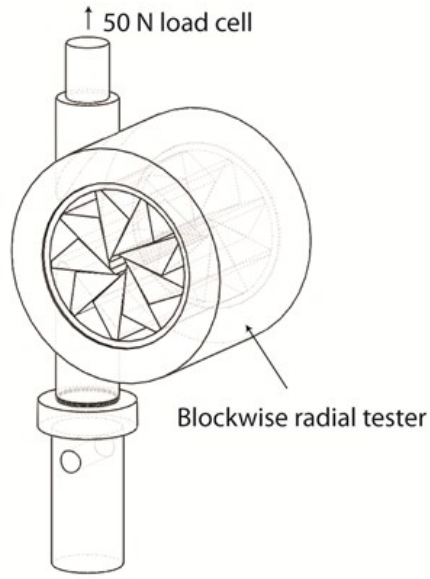


Figure 2.3. Sketch of Blockwise radial tester (not drawn to scale). The crimped device is placed in the center of the blades. As the temperature is ramped from ambient to 55 °C, the recovery of the device applies a load on the blades which is sensed by the load cell to which the radial tester is connected.

Bench-top thrombus removal

Figure 2.4 shows the bench-top thrombotic stroke model that was constructed to test the feasibility of the SMP flower-shaped devices for thrombectomy. The bovine thrombi that were utilized in the experiments were prepared following the protocol described by Gralla et al. (2006), with 10 ml of bovine blood acquired from Vet Med Park (College Station, TX), 1 g of barium sulphate and 25 IU of bovine thrombin both purchased from VWR. The mixture was injected into a silicone tube with 10 mm inner diameter, and gently agitated for approximately 1 minute. Thrombi were subsequently incubated at room temperature overnight and were sliced with a scalpel into approximately 2 cm long pieces prior to the experiments [70].

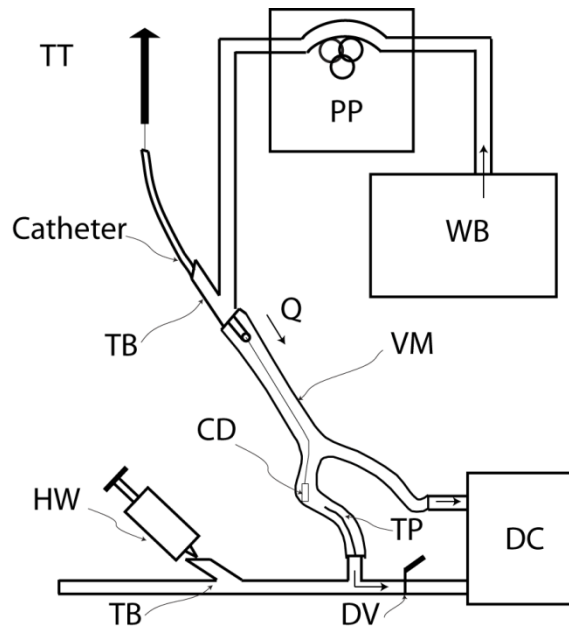


Figure 2.4. Bench-top thrombotic stroke model constructed to test the feasibility of the SMP flower-shaped devices for endovascular thrombectomy. WB: water bath (37 °C); PP: peristaltic pump; TT: tensile tester (extension rate= 75 mm/min); Q; experimental flow rate (=57 ml/min); TB: Touhy Borst valve; CD: crimped device location; VM: vessel model; TP: thermocouple probe; HW: hot water syringe; DV: discharge valve; DC: discharge container.

Each crimped device and a thrombus were inserted into the silicone bifurcated vessel model (Shelley Medical Imaging Technologies, Ontario, Canada) shown in Figure 2.4. Water at 37 °C was pumped into the main vessel segment (lumen diameter= 8 mm) at a flow rate of 57 ml/min via a peristaltic pump. The *in vivo* dynamically similar flow rate that corresponds to the experimental flow rate is within the range of flow rates recorded in the MCA, a common site for thrombotic occlusion in the neurovasculature [71]. The device was actuated by injecting water near boiling temperature with a syringe while shutting the valve that connects one of the bifurcations of the vessel model to the discharge container. The device was attached to a guidewire, which was connected to a tensile tester (MTS, Synergie) through a catheter. The device was pulled at an extension rate of 75 mm/min in the direction contrary

to that of the flow, to remove the thrombus. The temperature before and during actuation were recorded at 1 Hz by placing a thermocouple near the location of the device.

Results

Material properties of copolymers

Plots of storage modulus, loss modulus and tan delta for the four copolymers containing 5, 15, 25 and 35 mole % BPA in Figure 2.5(a-c) and numerical values for rubbery modulus, loss modulus peak temperatures and tan delta peak temperatures are provided in Table 2.1. Rubbery modulus values were taken at the minimum rubbery storage modulus points for all four chemical compositions. As the crosslinker increased from 5 to 35 mole %, rubbery modulus increased from 1.6 to 15.6 MPa. Loss modulus peak temperatures ranged from 50.8 to 62.3 °C, tan delta peak temperatures ranged from 61.5 to 72.3 °C, and both mechanical transition temperatures decreased with increasing BPA crosslinker composition. Strain-to-failure experiments were carried out on samples of all four BPA compositions at both mechanical transition temperatures. All stress-strain curves are shown in Figure 2.6, and average data of stress-at-failure, strain-to-failure, and toughness (i.e., the area under the stress-strain curves) are listed in Table 2.2. For strain-to-failure experiments conducted at loss modulus peak temperatures, increasing the BPA crosslinker from 5 to 35 mole % resulted in an average stress-at-failure increase from 11.9 to 23.0 MPa and an average strain-to-failure decrease from 1.43 to 0.47 mm/mm. For strain-to-failure experiments conducted at tan delta peak temperatures, increasing BPA crosslinker composition resulted in an average stress-at-failure increase from 2.7 to 7.7 MPa and an average strain-to-failure decrease from 1.41 to 0.37 mm/mm. For both the loss modulus peak temperature and tan delta peak

temperature strain-to-failure series, toughness decreased as BPA composition was increased from 5 to 15 to 25 mole %, and then increased for the 35 mole % BPA samples. One possible explanation for this increase in toughness for the most highly crosslinked samples is that bisphenol A groups have been shown to be capable of undergoing π - π stacking, which increases toughness in materials such as poly(bisphenol A carbonate) [72]. It is possible that at high enough BPA compositions, π - π stacking became predominant enough to improve toughness.

(a)

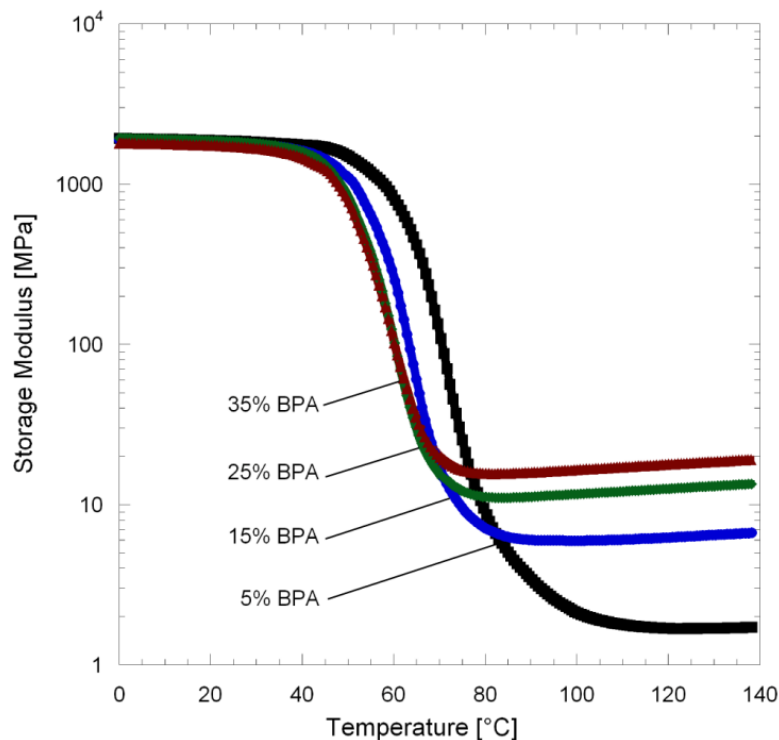


Figure 2.5. Dynamic mechanical response of four copolymers, namely storage modulus (a), loss modulus (b) and tan delta (c). By increasing the amount of crosslinker, the rubbery modulus (i.e., the lowest point of the storage modulus curve) also increases. The temperatures at loss modulus and tan delta peak decrease as a result of increasing crosslinker composition.

(b)

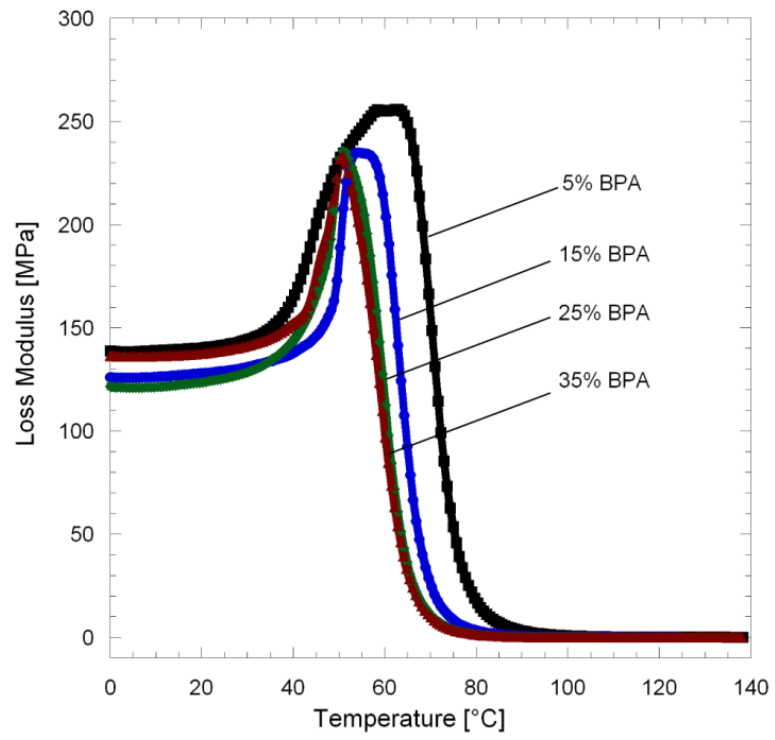


Figure 2.5. Continued.

(c)

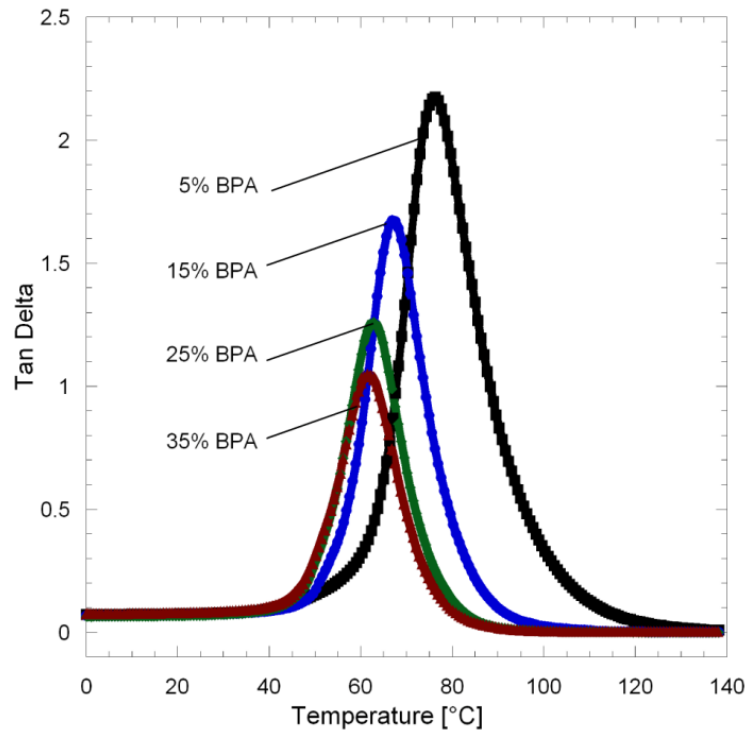


Figure 2.5. Continued.

Table 2.1. Rubbery modulus and mechanical transition temperature values.

Composition	Rubbery modulus (MPa)	Loss modulus peak temperature (°C)	Tan delta peak temperature (°C)
5% BPA	1.67 + 0.18	62.3 + 0.16	72.3 + 0.16
15% BPA	5.92 + 0.08	53.6 + 0.17	66.9 + 0.16
25% BPA	11.0 + 0.32	50.8 + 0.25	62.8 + 0.24
35% BPA	15.6 + 1.02	50.8 + 0.11	61.5 + 0.12

(a)

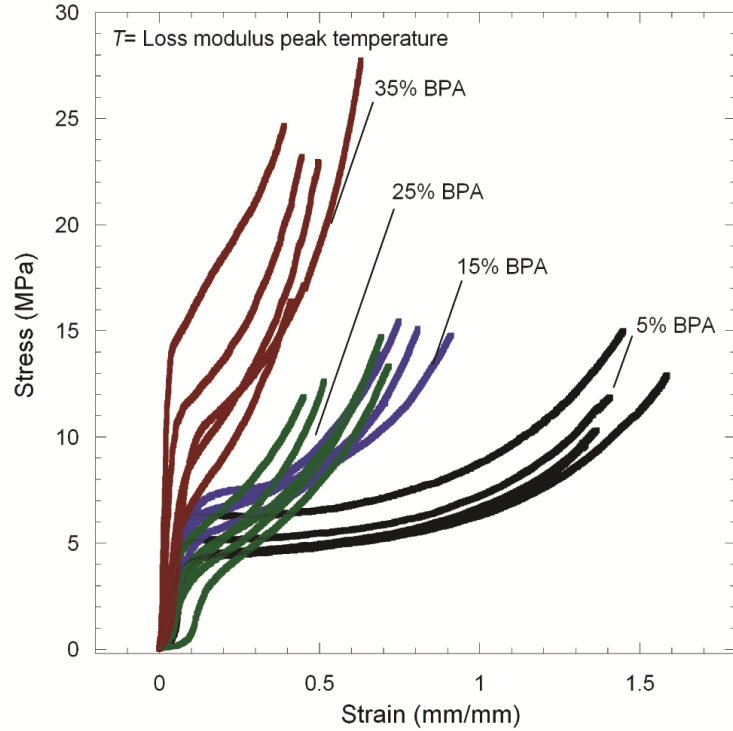


Figure 2.6. Tensile properties of the four copolymers measured at each copolymer's loss modulus peak a) and tan delta peak b) temperatures. For both temperatures, the effect of crosslinker percent on decreased strain capacity is evident. Additionally, the response of all four compositions when tested at tan delta peak temperature is more brittle than the response when tested at loss modulus peak temperature.

(b)

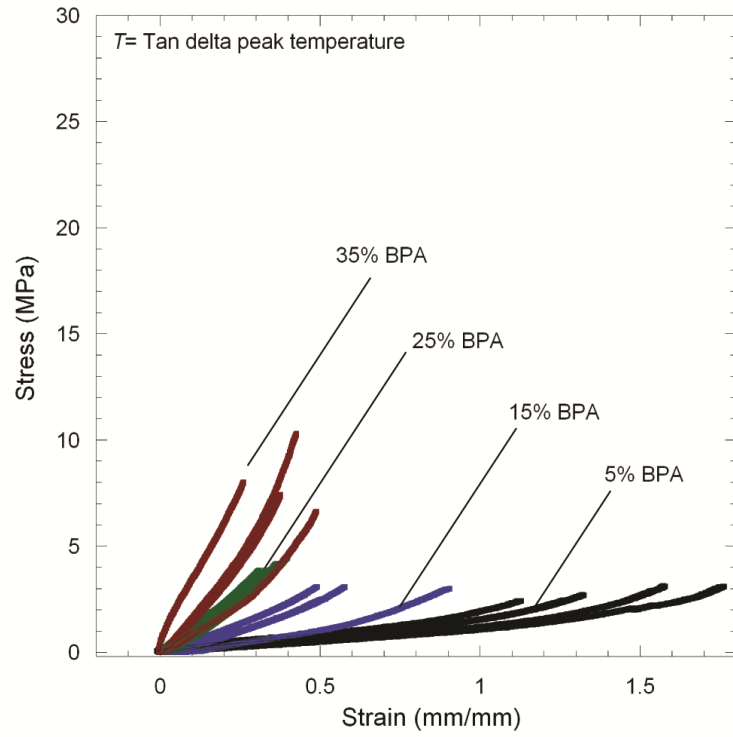


Figure 2.6. Continued.

Table 2.2. Average stress-at-failure, strain-to-failure, and toughness at loss modulus peak and tan delta peak temperatures.

	Composition	Strain-to-failure (mm/mm)		Stress-at-failure (MPa)		Toughness (MJ/m ³)	
<i>T</i> = temperature at loss modulus peak	5% BPA	1.43	± 0.0985	11.9	± 2.14	8.99	± 1.72
	15% BPA	0.773	± 0.0906	14.2	± 1.51	6.21	± 0.992
	25% BPA	0.609	± 0.119	13.2	± 1.07	3.96	± 0.747
	35% BPA	0.475	± 0.0957	23.0	± 4.15	6.38	± 1.79
<i>T</i> = temperature at tan delta peak	5% BPA	1.41	± 0.254	2.75	± 0.338	1.49	± 0.296
	15% BPA	0.590	± 0.182	2.87	± 0.254	0.697	± 0.169
	25% BPA	0.357	± 0.0354	4.09	± 0.251	0.647	± 0.0723
	35% BPA	0.376	± 0.0879	7.73	± 1.56	1.24	± 0.316

Device crimping

A total of five devices were crimped for each of the four BPA compositions at their corresponding loss modulus peak and tan delta peak temperatures. Figures 2.7(a) and 2.8(a) show plots of force versus extension during crimping at loss modulus peak and tan delta peak temperatures, respectively. Figures 2.7(b) and 2.8(b) show images of the top, side, and bottom views of crimped 35 mole% BPA devices at the two respective crimping temperatures. The crimping temperature had a significant effect on both the magnitude of the force required for crimping and on the propensity for device failure during crimping. For devices crimped at loss modulus peak temperature, the maximum average crimping force increased from 0.10 to 0.58 N as BPA composition increased from 5 to 35 mole %. None of

the devices crimped at loss modulus peak temperature failed upon crimping. On the contrary, the devices crimped at tan delta peak temperature were much more susceptible to failure: for the 5, 15, 25 and 35 mole % BPA samples, the number of devices that failed when crimped at this temperature was 1, 2, 3 and 5 respectively. Most failure locations consistently occurred at the base of the devices, and appeared to initiate at the edges of the center holes, as shown in Figure 2.8(b).

Device constrained recovery

Because of the significant device failures that occurred during crimping at tan delta peak temperatures, only devices crimped at loss modulus peak temperatures were subjected to constrained recovery tests. Five devices were tested for each BPA composition. In Figure 2.9, plots of average recovery stress versus temperature are shown for devices with varying BPA composition. As BPA composition increased from 5 to 35 mole %, average recovery stress increased from 0.526 to 12.2 kPa.

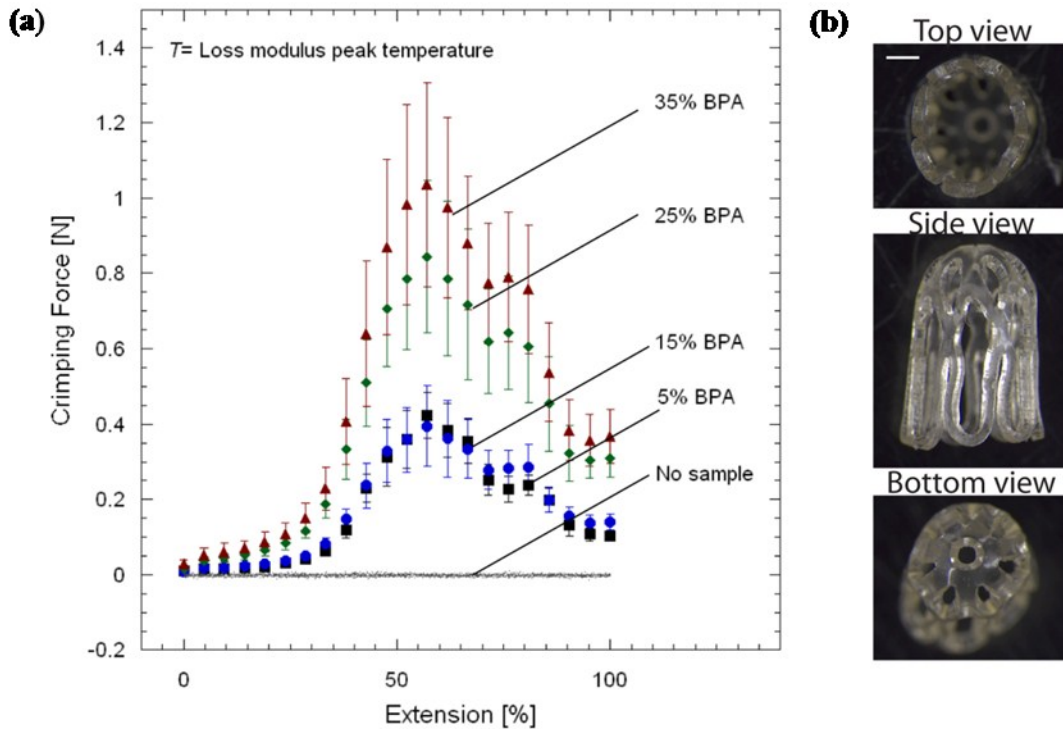


Figure 2.7. Force measurements of devices crimped at loss modulus peak temperature (a). Example of one device with 35 mole % BPA crimped at loss modulus peak temperature (scale bar= 1 mm) (b). Images taken at 2.5 \times magnification.

It is notable that during the constrained recovery tests, two out of the five 25 mole% BPA devices and four out of the five 35 mole% BPA devices developed cracks and subsequently broke. Images of crack development at different temperature points during constrained recovery of 25 and 35 mole % BPA devices are shown in Figure 2.10.

Bench-top thrombus removal

Three 5 and 15 mole % BPA devices were subjected to thrombus removal experiments with flow. In order to better simulate *in vivo* conditions, we chose an experimental flow rate of 57 ml/min because this flow rate is equivalent to 113 ml/min in the MCA after dynamic

similarity via matching of the Reynolds number (Re). This dynamically similar flowrate is within the range of flow rates recorded in the MCA, a common site for thrombotic occlusion in the neurovasculature [71].

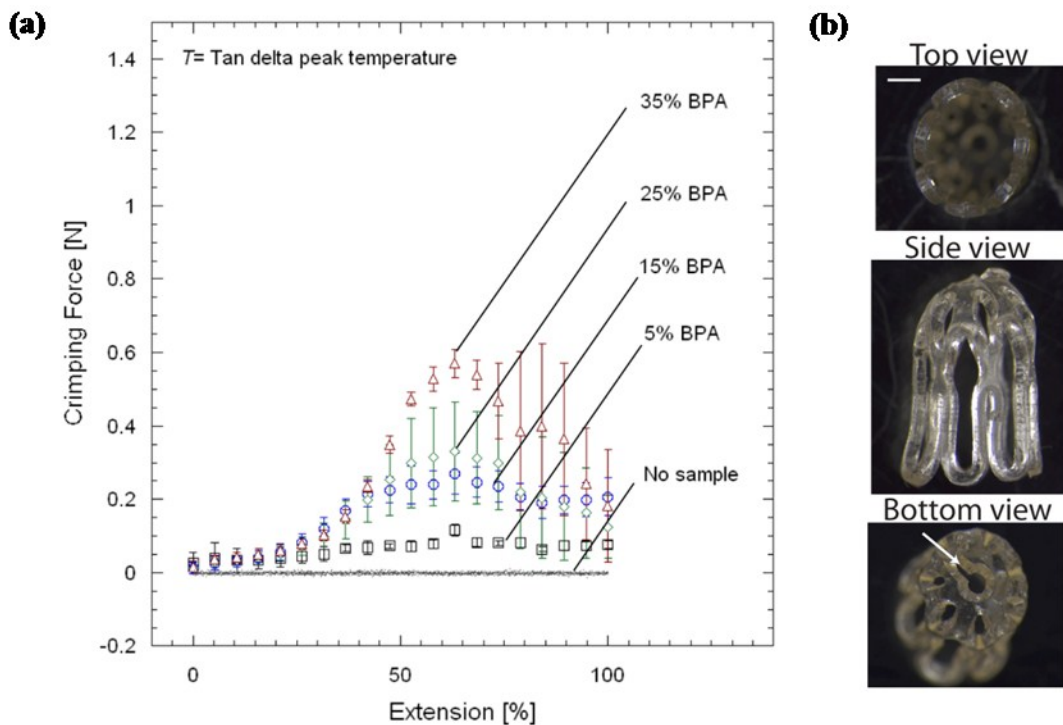


Figure 2.8. Force measurements of devices crimped at tan delta peak temperature (a). One 35 mole % BPA device crimped at tan delta peak temperature (scale bar= 1 mm) (b). Images taken at 2.5 \times magnification. White arrow points at failure site.

Because the 25 and 35 mole % BPA devices developed cracks during recovery under constrained conditions, they were not considered for the thrombus removal experiments. Images of the thrombectomy experiments for a 15 mole % BPA device and a diagram of the

silicone vascular model that was used in the experiments are provided in Figure 2.11. To demonstrate that the crimped devices were able to maintain their crimped geometries under physiological conditions, they were first immersed in 37 °C water and positioned past a bovine thrombus in the silicone vessel model, as pictured in Figure 2.11(a).

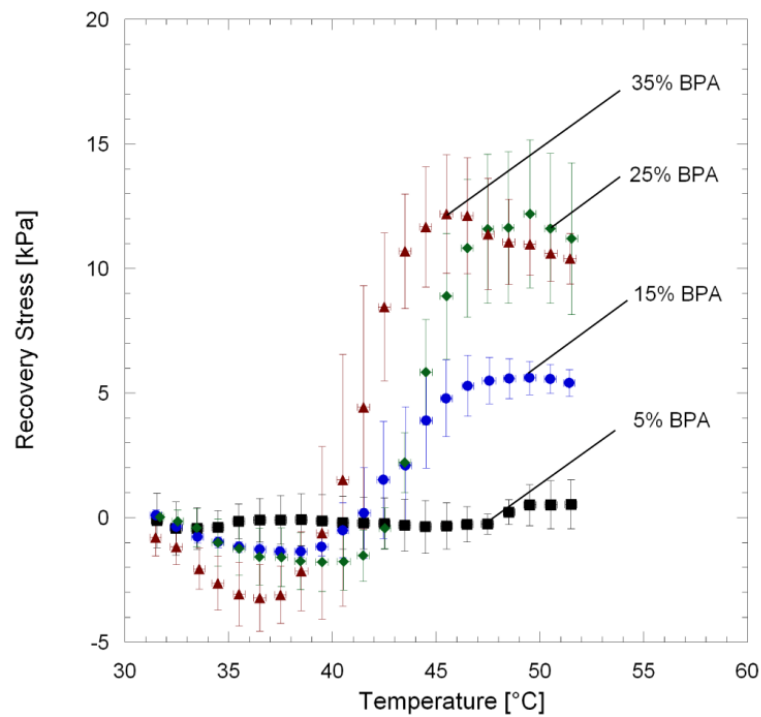


Figure 2.9. Recovery stress of devices during constrained recovery. Increasing the amount of crosslinker results in an increase in the recovery stress measured under constrained conditions.

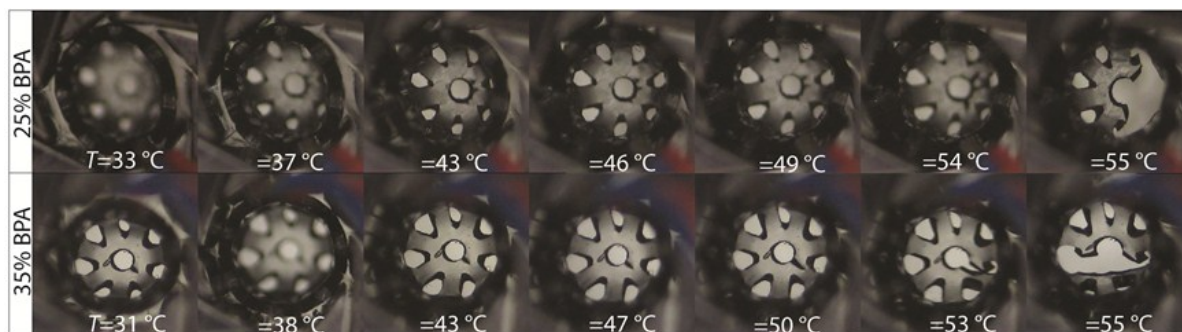


Figure 2.10. Crack development in devices with 25 and 35 mole % BPA during constrained recovery test at different temperature points.

After holding at 37 °C to demonstrate shape fixity for 4-5 min, the water temperature was elevated to $\sim T_g + 15$ °C (max recorded temperature: 77 °C) over the course of 45 s by injecting water near boiling temperature to the flow system. The effect of increasing crosslink density on the device thrombus removal success is clearly demonstrated: 0/3 of the 5 mole % BPA devices resulted in a successful thrombus removal, while 2/3 of the 15 mole % BPA devices successfully removed the thrombus (i.e., the devices were able to move the thrombus from its origin at the bifurcation pictured in Figure 2.11(b) to the catheter at the end of the model vasculature, pictured in Figure 2.11(e)).

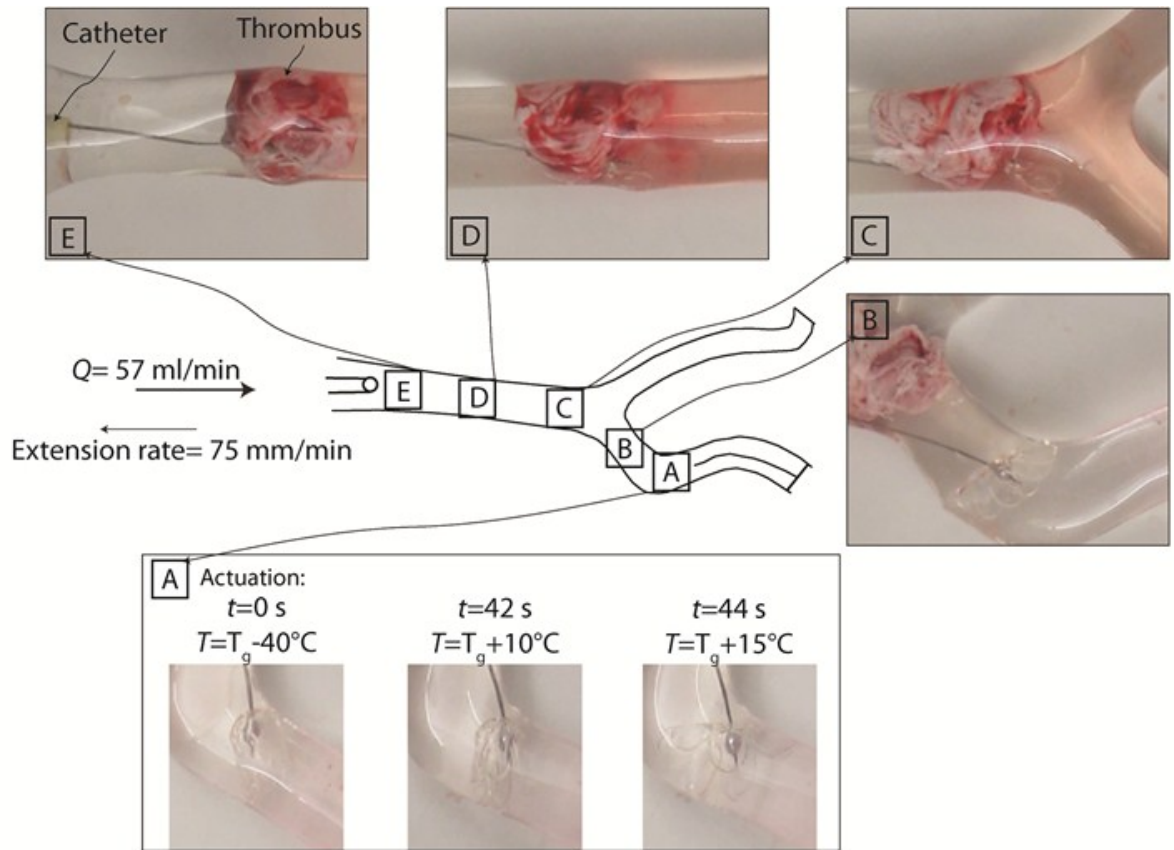


Figure 2.11. Actuation and thrombus removal with 15 mole % BPA device. Q: experimental flow rate. After actuation (panel A) the device exerts enough recovery force to deform the walls of the silicone vessel model as seen in panel B. The device is able to hold the thrombus during removal as shown in panels C-E.

Discussion

The motivation of this study is the need for an SMP-based thrombectomy device that is capable of exhibiting sufficient recovery stress to reduce the likelihood of thrombus dislodgement during thrombectomy, while also being able to undergo sufficient deformation for catheter delivery. While there are commercially available devices for thrombus removal, the potential complications that occur can be reduced by utilizing an SMP-based thrombectomy device [2, 51-53].

Our group has previously investigated SMP-based thrombectomy devices for thrombus removal, and one important finding during preliminary animal studies is that the recovery stress of an SMP-thrombectomy device is key to ensure thrombus entrapment and successful removal [62]. The devices tested in the bench-top thrombotic stroke model in this study consist of 5 and 15 mole % BPA crosslinker. The average recovery stress of the latter is roughly one order of magnitude higher than that of the former. This positive correlation between crosslink density and recovery stress in SMPs has been reported in numerous previous studies [56, 66, 67]. In an ideal rubber, elastic modulus is inversely proportional to the average molecular weight between crosslinks, so a more highly crosslinked rubber will exhibit greater stiffness than a more lightly crosslinked one [65]. Therefore, more energy is required to achieve a specific deformation in a more highly crosslinked rubber than in a more lightly crosslinked rubber. Since the energy required to achieve these deformations is metastably stored when thermally actuated SMPs are strained and then cooled below their thermal transition regions, the force exerted by an SMP during recovery is consequently higher for a more highly crosslinked SMP [56, 65-67, 73]. None of the 5 mole % BPA devices (0/3) exert enough recovery stress to hold the thrombus in our bench-top thrombotic stroke model, while 2/3 of the 15 mole % BPA devices do retain the thrombus as it is being removed.

The goal of varying crosslink density is to increase device recovery stress for improved thrombus hold. However, increases in crosslink density also have a negative effect on device mechanical integrity: the majority of the 25 and 35 mole % BPA devices do not sustain the constrained recovery experiments. The temperature at which the devices are crimped also

plays an important role in device integrity. The strain-to-failure data in Figure 2.6 shows that the stress required to achieve specific deformations decreases with increasing temperature for all compositions. Thus, it is expected that the forces required for crimping at higher temperatures (tan delta peak temperatures) are lower than those required for crimping at lower temperatures (loss modulus peak temperatures). Also, significant failure rates occurred during crimping at tan delta peak temperatures, while no failures occurred during crimping at loss modulus peak temperatures. This trend in failure during crimping was most likely observed because the samples are in higher toughness states at loss modulus peak than at tan delta peak temperatures (see Table 2.2). As expected, failure rates are higher in devices with higher crosslink densities. In all cases, failures originate at the base of the devices. The devices that result in most failures have one characteristic in common: their strain capacities are significantly reduced (see strain-to-failure values at tan delta peak temperatures for 25 and 35 mole % BPA devices in Table 2.2). Therefore, the high localized strains at the base of the devices in conjunction with material limitations and possible machining defects, most likely cause crack initiations that then lead to device failures.

For the devices that are successfully crimped, the recovery stress under constrained conditions increases with increasing crosslink density. Nonetheless, some of the devices with 25 and 35 mole % BPA, which have rubbery moduli greater than 10 MPa (see Table 2.1), fail during constrained recovery. In a similar manner to the findings in this study, Safranski et al. reported that for acrylic SMPs with rubbery moduli greater than 10 MPa, the crosslinking dominates the large strain mechanical properties of the network and a relatively brittle response is observed [69]. This pronounced brittle response in addition to possible

machining defects may be the reason for failures in the devices with higher crosslink densities during constrained recovery.

Full constrained recovery experimentation represents a worst-case condition, but it is of great importance for a device such as the SMP flower-shaped thrombectomy device in this study. The pressure elastic modulus of the common carotid artery, for example, is reported to be on the order of 55 kPa for healthy patients [74]. However, as patients get older and arteries become more diseased, this value has shown to increase to about 165 kPa [75]. Simply testing an actuating thrombectomy device in a silicone vessel model alone and neglecting to perform constrained recovery experiments could result in device failures such as the ones observed during the constrained recovery experiments in this study to remain unnoticed because a silicone vessel model could be more compliant than a diseased artery. Thus, constrained recovery analysis should be performed a priori to avoid fatal complications that would probably only come into play in a more realistic environment, such as a diseased artery in a stroke patient.

Conclusion

In this work we have reported an acrylic SMP system with glass transitions above body temperature in the range of 65 to 75 °C with tailorable recovery stresses that were controlled by varying crosslink density. The increase in recovery stress that came with increasing crosslink density also resulted in higher propensities for device failure. Similarly, crimping temperature significantly influenced device failure: crimping at theoretical maximum

toughness state, loss modulus peak temperature, required a higher force, but minimized device failure, in comparison with crimping at tan delta peak temperature. Devices with rubbery moduli greater than 10 MPa that were successfully crimped, failed upon constrained recovery testing. Consequently, an optimal crosslink density for the SMP system reported in this study—one that both enables sufficient recovery stress for successful thrombus removal but also allows for sufficient device mechanical integrity—appears to be one that results in a rubbery modulus between that of the 15 mole % BPA sample (i.e., 6.0 MPa) and 10.0 MPa.

Our results demonstrate that SMP materials with the highest rubbery moduli are not necessarily the best for applications requiring large deformations. From the four different material compositions evaluated, devices with 15 mole % BPA gave the most favorable outcome. They exhibited average maximum recovery stresses approximately 1 order of magnitude greater than those of the 5 mole % BPA devices and were also capable of undergoing the deformations necessary for device crimping. The development of the tunable acrylic SMP system reported in the study ultimately enabled the fabrication of a thrombectomy device that is shorter than commercially available devices, possesses enough recovery force to remove a thrombus, and does not fail during constrained recovery.

CHAPTER III

SMP-SMA THROMBECTOMY DEVICE

In the previous chapter, a materials engineering solution to a significant clinical problem that has affected and continues to affect thousands of patients worldwide was presented. Flower-shaped thrombectomy devices were fabricated from a system of crosslinked acrylic SMPs to enhance the recovery stress of the devices for better thrombus hold during removal. The results showed that devices with rubbery moduli between 6.0 and 10.0 MPa exhibited sufficient recovery stress for thrombus removal, and also possessed the necessary strain capacity for catheter delivery. However, a major flaw that was encountered was the potential difficulty in centering the device with respect to the vessel lumen during actuation, as illustrated in Figure 3.1. Poor device centering could result in gaps between the device and the vessel lumen post-actuation that increase the potential of thrombus dislodgement, regardless of the ability of the device to recover its primary shape. This problem, which is related to the device geometry, prompts the need to re-evaluate the design of the thrombectomy device.



Figure 3.1. Flower-shaped thrombectomy device off-centered after actuation. Device was painted with a black marker for better visualization.

Introduction

One of the greatest advantages of the new commercially available technology in thrombectomy, called stent retriever technology, is that undeployed stents have a small enough undeployed outer diameter that enables them to be delivered through the thrombus. The general procedure for deployment is to position the self-expandable nitinol stent such that the thrombus is centered within their length. Stents act as a temporary bypass and enable the rapid restoration of blood flow [76]. In addition, they are designed to ensnare the thrombus in their struts for removal. Examples of these devices include the ReviveTM SE (Codman and Shurtleff, USA), the Aperio[®] (Acandis, Germany) and the FDA-approved SolitaireTM FR (ev3, USA) and Trevo[®] (Stryker, USA) [77]. Although stent retrievers have proven to outperform the Merci Retriever[®] (e.g., primary effectiveness endpoint success rate of 60.7% and 87.3% for the SolitaireTM RF and Trevo[®] respectively versus 58% for the

Merci Retriever®), in some instances their use is severely limited [78, 79]. One of the biggest drawbacks is that their length, which is usually 20-30 mm, significantly reduces their post-deployment maneuverability in tortuous vessels such as the MCA. Maneuverability is particularly difficult in atherosclerotic patients, whose calcified lesions and hard thrombi tend to catch on the struts of the stent often resulting in the inability to retrieve the device [76].

Nitinol is limited by maximum strains on the order of 10%, thereby significantly reducing the volume changing capabilities of nitinol-based thrombectomy devices, which is probably one of the primary reasons why their length cannot be reduced further. In the case of the Merci Retriever®, 50 mm of wire are required to achieve 5 loops of the corkscrew shape with diameters between 2.7 and 1.1 mm [80]. The stents are shorter than the Merci Retriever®, but still long enough to cause problems upon thrombus removal [76]. Taking these facts into account, as well as the results that were discussed in Chapter II, a new set of design requirements is needed.

Design requirements

The approach that was taken in the design of the new thrombectomy device is based on the waterfall design control model implemented by the FDA. The first step was the evaluation of the design requirements. The criteria for the design requirements were based on the user needs, which got translated into design inputs. Once a prototype was fabricated, bench-top tests were performed to verify that the design requirements were met. Finally, validation of the design requirements was sought through the use of an animal model.

From the information in the literature, the limitations of the FDA-approved treatments of acute ischemic stroke were identified. Among these limitations are the narrow treatment time window for tPA, arterial perforation and spasm, thrombus fragmentation and distal migration, limited post-deployment device flexibility, and restricted placement caused by the length of the devices that is required to be advanced beyond the thrombus [2, 7, 14, 42,53, 76, 81-83]. Based on these complications, the user needs were defined as a thrombectomy device that can:

1. increase the treatment time window;
2. enhance thrombus hold;
3. prevent distal migration of thrombus fragments;
4. exhibit better post-deployment flexibility; and
5. require a shorter deployment length.

The design of a distal device (i.e., the entire device is deployed distal to the thrombus) with deployment length shorter than commercial devices was employed. Implementing such a design required that the outer diameter of the undeployed device be as small as possible to enable delivery through the thrombus. Therefore, a material able to achieve high volume expansion rates was needed, such that it could be small enough for through-thrombus delivery, be large enough to conform to the vessel lumen for thrombus removal, and offer sufficient rigidity for thrombus hold, while keeping the length of the device as short as possible. In order to supply these various material requirements, a hybrid device design that combined the use of SMP foam and nitinol was selected. The device concept is shown in Figure 3.2 and it consisted of the delivery of crimped SMP foam and a flower-shaped nitinol

portion past the thrombus, followed by the actuation of the SMP foam and subsequent removal of the thrombus. SMP foam was proposed as a major component of the thrombectomy device because it has density values less than 0.03 g/cm^3 , which enables a volume expansion rate of over $20\times$ [55]. Additionally, preliminary animal studies have shown that SMP foams have good biocompatibility [84]. Nitinol was selected as the second component of the thrombectomy device because it is capable of exhibiting shape memory, it has superior yield strains than comparable alloys such as stainless steel 316 L, and its compliance can be modified through the use of heat treatments [59, 85]. Furthermore, it has been widely used in FDA-approved medical devices, including the two most recently FDA-cleared thrombectomy devices [59]. The nitinol portion of the device was intended to compress the free-moving SMP foam against the thrombus to prevent the slippage of the SMP foam out of the device assembly. Its pre-shaped four-strut flower geometry (hence the name shape memory nitinol flower (SNF)) when unloaded provides the struts with a finite radius of curvature and reduced tension that allows the struts to buckle more easily providing a larger diameter for the SNF to compress the SMP foam (see Appendix A for previous design iterations). From preliminary experiments it was observed that the axial compression applied to the SMP foam during thrombus removal resulted in favorable radial expansion. From this data we hypothesized that this diameter expansion would allow the SMP foam to better conform to the uneven lumen of the occluded vessel during thrombectomy, thus preventing device-vessel gaps that could result in the distal migration of smaller thrombi. The design inputs for the SMP foam-nitinol thrombectomy device are listed in Table 3.1.

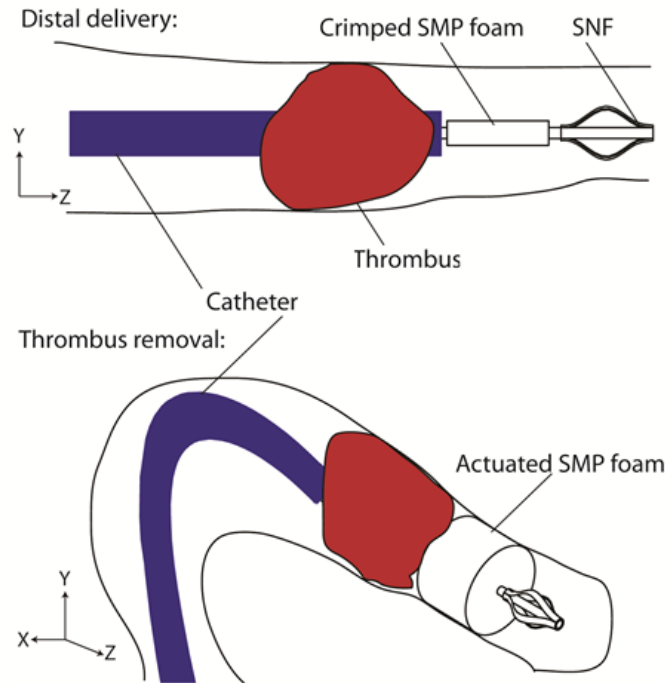


Figure 3.2. Design concept of new hybrid thrombectomy device. Upon distal delivery, the SMP foam actuates to its primary shape and the SNF supports the SMP foam as it gets compressed against the thrombus during removal.

Table 3.1. Summarized design inputs for hybrid thrombectomy device.

Parameter	Target range	Acceptable value
Length of device	6-8 mm	<15 mm
Diameter of crimped foam	0.6-0.8 mm	1 mm
Diameter of undeployed nitinol flower	<0.8 mm	1 mm
Diameter of actuated foam	\geq diameter of target vessel	= diameter of target vessel
Device-catheter friction force (6 F catheter) [86]	≤ 0.3 N	0.5 N
Device working time	Unlimited for deployment, < 2 min for retrieval	10 min for deployment, ≤ 5 min for retrieval

Design selection

The selection of the final design of the hybrid thrombectomy device entailed preliminary experiments for the selection of the SMP foam type, particularly regarding the shape of the SMP foam sample (i.e., cylindrical vs oval) and the average cell size. The chemistry of the SMP foams can be found in [87].

From preliminary axial compression tests in 37 °C water, it was observed that the shape of the SMP foam affects the amount of radial expansion. As shown in Figure 3.3, cylindrical SMP foam samples exhibit greater diameter expansion rates as a function of axial compression, compared to oval samples. Thus, cylindrical samples were selected as the shape of the SMP foam component of the thrombectomy device.

To determine the appropriate range of SMP foam cell size for this application, SMP foams with three different cell sizes were fabricated by varying the viscosity of the pre-polymer mix. The resulting SMP foams are pictured in Figure 3.4, and the average cell size, density and T_g measured by differential scanning calorimetry (DSC) are listed in Table 3.2. The SMP foams were labeled as F44, F68 and F110 to represent their average cell sizes, which were 0.44, 0.68 and 1.1 mm respectively.

Cylindrical samples of each SMP foam type were cut using a biopsy punch (Sklar Instruments) with 6 mm diameter. The length of all SMP foam samples was cut to 5 mm with a straight edge razor. The shape recovery rate of the three types of SMP foams and the diameter expansion as a function of axial compression were tested in 37 °C water. For each

test, three samples of each SMP foam type were evaluated. The shape recovery rate experiment consisted of submerging one sample of crimped SMP foam at a time in 37 °C water and acquiring images with a photographic camera (Canon, Powershot SX 230 HS) every 10 seconds. Three diameter measurements were made at every time point using ProGress Pro capture Software, which was calibrated for every image. The axial compression experiments were performed in a similar manner, except that the foam was compressed to known percentages using a custom-machined acrylic apparatus. This apparatus consisted of a rectangular acrylic container with a movable insert. The insert was moved by the rotation of two screws towards one of the walls of the acrylic container. The acrylic container and insert had a center hole through which a 0.25 mm diameter wire was fed. The wire held the sample of SMP foam in place as the insert was moved to compress the sample axially. Images at compression percentages of 0, 15, 30, 45, 60 and 75% were acquired utilizing the Canon camera, and three diameter measurements were taken at each compression level. The shape recovery and diameter expansion as a function of axial compression in 37 °C water for all three foam types are shown in Figures 3.5 and 3.6 respectively.

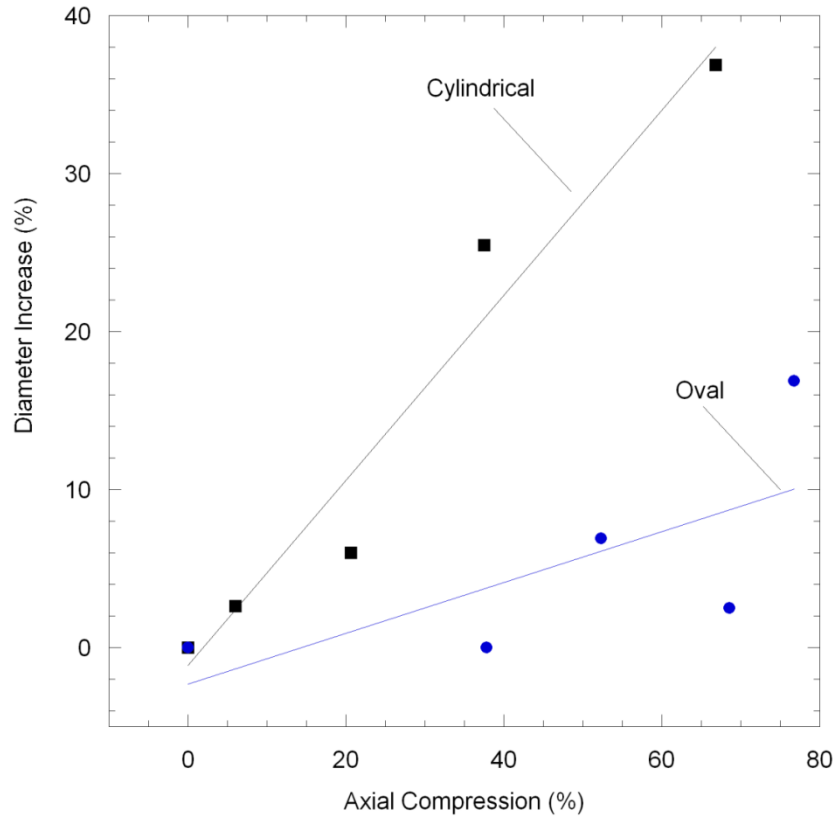


Figure 3.3. Preliminary results of radial expansion of the SMP foam as a function of axial compression. A first-order least squares fit is applied to the data. Cylindrical samples achieve a greater diameter increase as a result of axial compression compared to the oval samples.

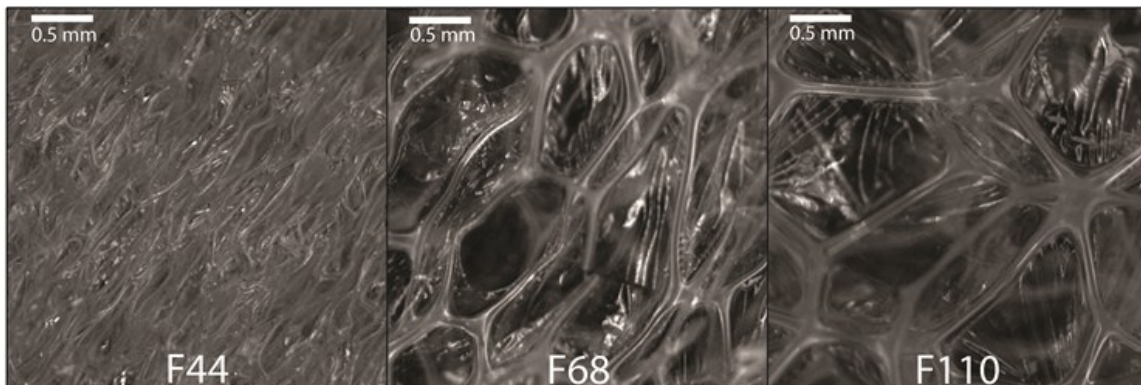


Figure 3.4. SMP foams considered in the selection of the final design of the hybrid thrombectomy device. The average cell sizes are 0.44, 0.68 and 1.14 mm for foams F44, F68 and F110 respectively.

Table 3.2. Properties of SMP foams.

SMP foam label	F44	F68	F110
Average cell size (mm)	0.44 ± 0.14	0.68 ± 0.21	1.14 ± 0.40
Density (g/cm ³)	0.026	0.027	0.028
T _g (°C)	60	59	56

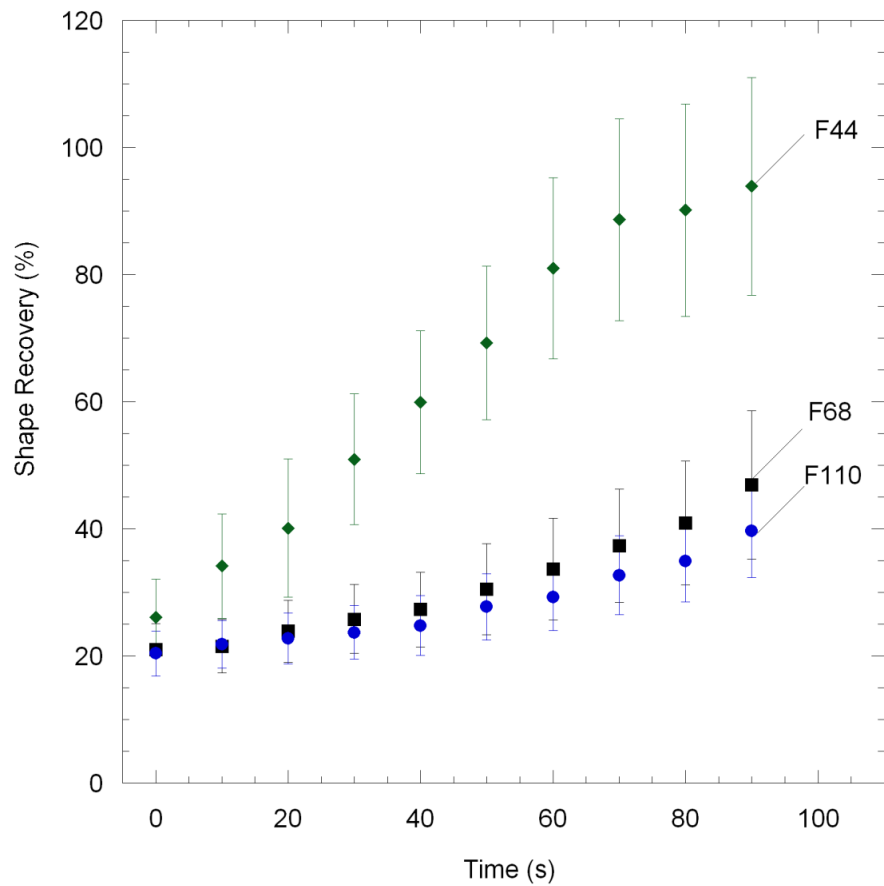


Figure 3.5. Shape recovery in 37°C water of foams F44, F68 and F110 (n=3). A better shape recovery is observed for SMP foams with smaller cell size compared to SMP foams with larger cell size (e.g., F44 versus F110).

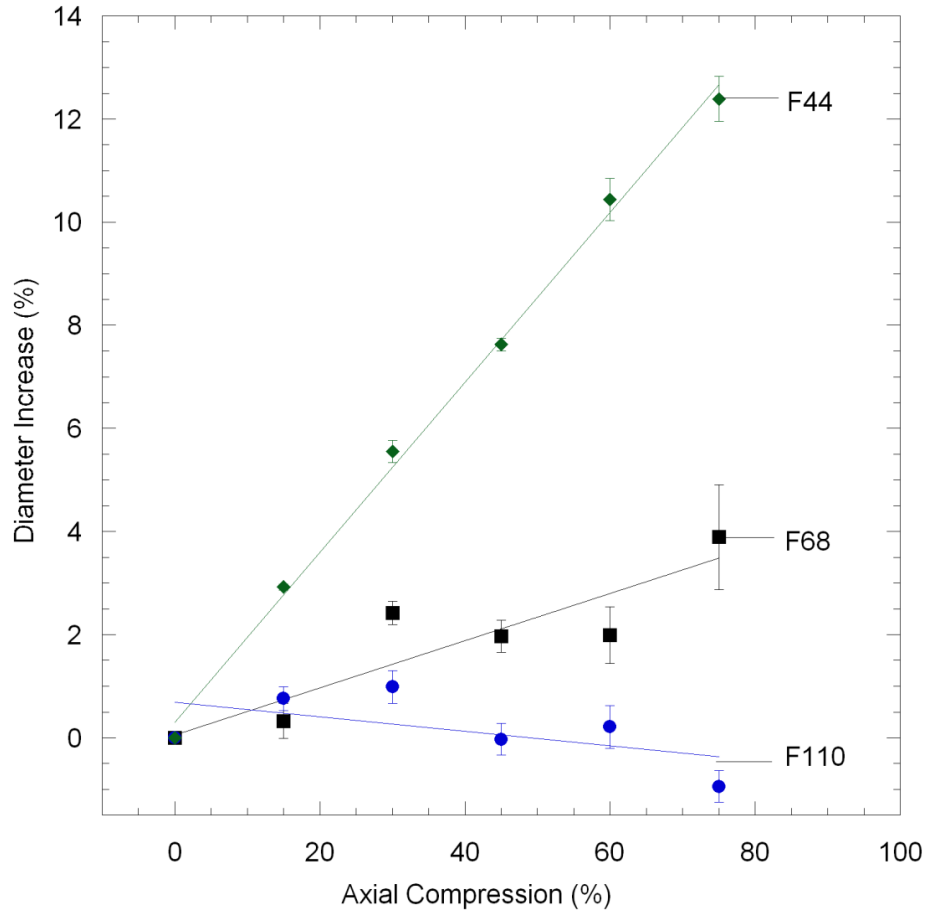


Figure 3.6. Diameter expansion in 37°C water of foams F44, F68 and F110 (n=3). Foam F44 exhibits a greater diameter increase as a function of axial compression compared to foams F68 and F110.

From these preliminary experiments it was concluded that smaller average cell sizes (less than 0.44 mm) showed better shape recovery (i.e., 90% compared to $\leq 60\%$ within the first 90 seconds of water at body temperature exposure) during passive actuation, and greater amount of diameter expansion as a function of axial compression (i.e., 12% versus $\leq 2\%$) compared to SMP foams with average cell size greater than 0.68 mm.

Materials and methods

Proof of concept

SNF machining: The SNF was fabricated from nitinol tube with 0.4 mm outer diameter and 0.3 mm inner diameter purchased from NDC. Four 5 mm long straight struts were laser cut along the surface of the tube every 90° using an excimer laser with a rotary axis (RapidX, Resonetics) with the following settings: 248 nm wave length; demagnification of 29; mask size of 2 mm; power of 4 mJ; frequency of 100 Hz, and 100 pulses. These settings were selected because machining was achieved on average in only two passes with an amount of power and frequency rate that did not overburden the laser. After the struts were laser cut, the piece was sliced from the rest of the nitinol tube utilizing the same laser settings, and its final length was 7 mm. Then, the cut area was carefully sanded with 600 grit sand paper and cleaned with acetone. To set the flower shape, the laser-cut nitinol tube was mounted on a custom-made aluminum fixture that allowed for a gradual and controlled compression of the SNF axially, resulting in the buckling of the struts. The nitinol tube mounted on the fixture were then placed inside a furnace at 550 °C for 7 minutes and subsequently quenched in water at room temperature.

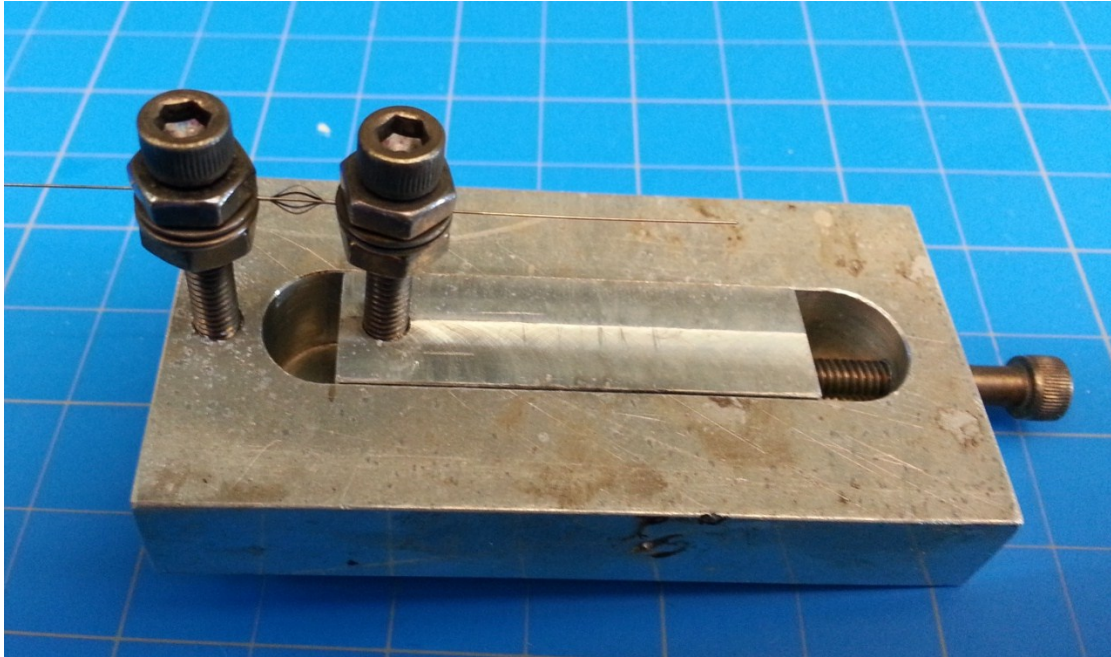


Figure 3.7. Aluminum fixture for SNF shape setting. The set screw on the right is utilized to move the center piece for the gradual and controlled compression of the SNF between two washers. Once the desired deformation is achieved, the fixture is placed in a furnace at 550 °C for 7 minutes.

Bench-top thrombotic model: The SNF was adhered to the distal tip of a 1000 mm long nitinol wire with 0.25 mm diameter purchased from NDC, using medical grade UV curable epoxy (Epotek). Proximal to the SNF was crimped a cylindrical sample of foam F44. Three samples of foam F44 were cut with 6, 8 and 10 mm diameters and their length was kept at 5 mm. The prototypes were tested in the same thrombotic stroke model as described in Chapter II utilizing bovine thrombi prepared as previously described (see Figure 2.4).

Device fabrication

Tungsten-doped SMP foam characterization: SMP foams doped with tungsten at a concentration of 4% by weight were utilized in the devices that were fabricated for the animal study. Tungsten acts as an inert filler to make SMP foam visible under fluoroscopy, which is the standard imaging modality for clinical and pre-clinical endovascular procedures [84]. The average cell size, density and T_g of the doped SMP foam was 0.18 ± 0.077 mm, 0.70 ± 0.0058 g/cm³ and 60 °C, respectively. Cylindrical samples of this SMP foam were cut using the 6 mm diameter Sklar biopsy punch. The length of all SMP foam samples was cut to ~5 mm with a straight edge razor. The shape recovery rate and the diameter expansion as a function of axial compression of the SMP foam were tested in 37 °C water (n=3). The shape recovery rate experiment consisted of submerging one sample of crimped SMP foam at a time in 37 °C water and acquiring images with the Canon Powershot camera every 10 seconds. Three diameter measurements were made at every time point using the ProGres Pro capture software, which was calibrated for every image. The axial compression experiments were performed using the Instron dual column tensile tester with a 50 N load cell (with resolution of 0.00025 N). For these experiments, the crosshead was manually controlled utilizing the Instron's fine position thumb wheel, to SMP foam compression levels of 0, 15, 30, 45, 60, and 75%, and the load was recorded by hand. Images were acquired using the Canon Powershot camera, and three diameter measurements were made at each compression level using the ProGres Pro software. To ensure that the SMP foams were in rubbery state during each experiment, they were kept saturated with water at ~70 °C.

Guidewire fabrication and device assembly: The same nitinol tube used for the SNFs (length=1220 m) was utilized in the guidewire construction. Braided nitinol wire (Assahi Intecc, actone flat) (length= 330 mm) with 0.31 mm outer diameter and 0.16 mm inner diameter was inserted in the distal end of the nitinol tube, and a 1064 nm YAG laser welder (i990, LaserStar) was used to weld both components. The final device was assembled by welding the pre-shaped SNF at the distal tip of the actone flat utilizing the LaserStar laser welder, followed by the crimping of a sample (diameter ~6 mm, length ~5 mm) of tungsten-doped SMP foam proximal to the SNF as shown in Figure 3.8(A).

Device delivery system: The SMP foams that were utilized for this thrombectomy device are hydrophilic and get plasticized when exposed to moisture [88]. Plasticization is caused by hydrogen bonding between the SMP foam's carbonyl groups and the water molecules. As a result, the gaps between the polymer chains increase and therefore have higher mobility reducing the T_g of the SMP foam [55]. Therefore, the catheter delivery of the thrombectomy device is challenging because there is a risk of premature SMP foam actuation prior to deployment. To solve this problem, a delivery system that constrained the SMP foam during catheter delivery and achieved deployment by means of a pusher and a hex cap screw, was designed and implemented as shown in Figure 3.8(B).

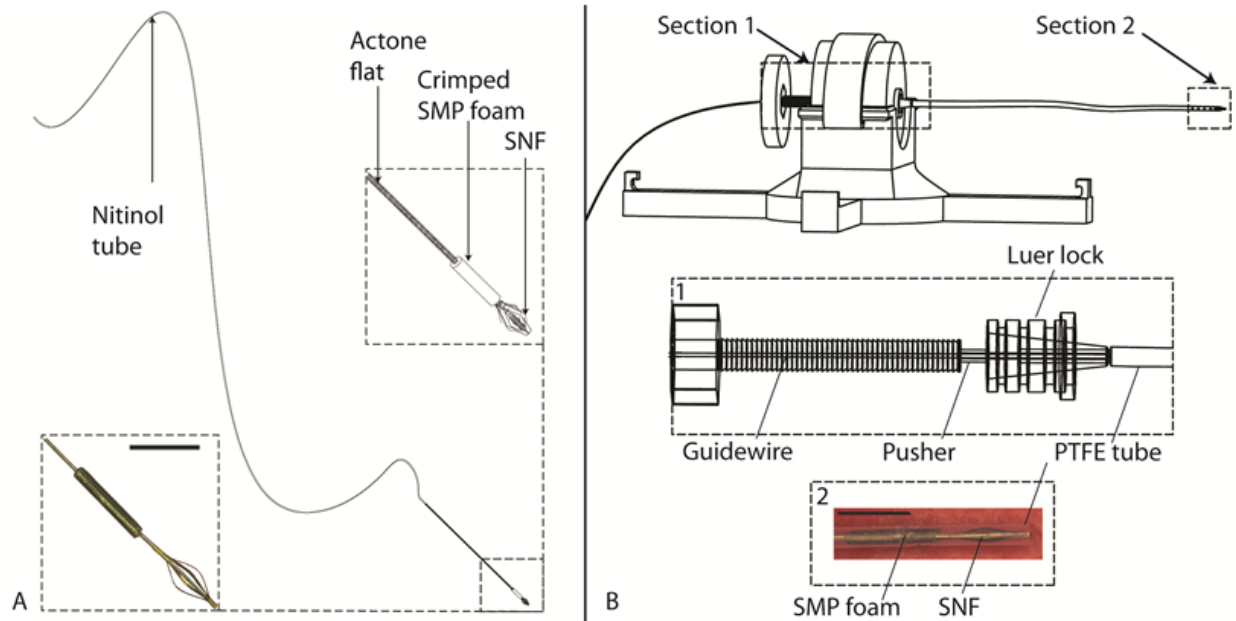


Figure 3.8. Guidewire assembly (A) showing a picture of an actual device acquired at 1.25× magnification (scale bar= 5 mm), and delivery system construction showing a crimped device inside the PTFE tube (1.25× magnification, scale bar= 5 mm) (B). The delivery system functions by means of a pusher that is activated by the rotation of a screw.

The entire device assembly was inserted in an 18 AWG, lightweight wall, medical grade PTFE tube purchased from Zeus with the SMP foam positioned at the distal tip of the PTFE tube. Eight holes were punctured on the PTFE tube around the location of the SMP foam using a 23 gauge needle to aid in the flushing of water to remove air from the tube prior to being delivered through the catheter. The PTFE tube was attached to an 18 gauge needle, whose length was cut to 8 mm, and whose distal tip was dulled using a dremmel.

An acrylic holder was fabricated utilizing the Roland CNC and it served to support a cylindrical acrylic insert that contained a luer lock on one end, and a 14 mm long threaded hole on the other end. These two features were connected by a 1.3 mm hole. The modified

18 gauge needle served as the attachment between the PTFE tube and the acrylic insert by means of the luer lock, allowing the guidewire to be advanced through both parts. A nitinol tube (outer diameter 0.58 mm, inner diameter 0.51 mm), with an outer diameter small enough to fit through the PTFE tube and 18 gauge needle, and with an inner diameter large enough to fit the guidewire in its lumen, was utilized as the pusher. It was inserted through the proximal end of the guidewire up to the location of the crimped SMP foam. The length of the pusher was cut such that when a hex cap screw, which had a 0.46 mm diameter hole through the center (small enough to fit the guidewire but not the pusher), was screwed to the end of the threaded 14 mm hole, the distal end of the pusher was flush with the distal end of the PTFE tube, thereby pushing the SMP foam out. A female luer lock was adhered with a cyanoacrylate-based glue (360, Loctite) to the 18 gauge needle holding the PTFE tube. Its purpose was to allow the proximal end of the catheter to be locked to the entire delivery system, so that during thrombus removal, all components could be retrieved as a single unit. Thus, it was necessary that the length of the PTFE tube was sized according to the length of the catheter. A 3-way stop cock was glued to the cap of the hex screw, and a Touhy borst adaptor was used to make the proximal end of the delivery system water tight to enable the flushing of air from the PTFE tube.

Bench-top testing

Weld tensile strength: It has been shown that welding nitinol results in joints with decreased strength compared to stainless steel welded joints, mainly due to the oxide layer in the surface of nitinol components [89]. Furthermore, the selection of the welding parameters has an effect on the mechanical performance of the joints [90]. In order to determine the

LaserStar welding parameters utilized in both weld types, the three different settings listed in Table 3.3 were evaluated in samples separately prepared for tensile testing (n=3). The center welds were intended for the nitinol tube-actone flat joint, and the end weld for the SNF-actone flat weld. The goal was to find the setting that resulted in the highest possible fracture load. To achieve this goal, welded samples were extended to failure at an extension rate of 75 mm/min (the same extension rate utilized in the bench-top thrombectomy) using the Instron Tensile tester with the 50 N load cell. Data were recorded at 1 Hz through BlueHill 3 software.

Table 3.3. Laser welding parameters for the assembly of nitinol components.

Type of weld	Voltage (V)	Pulse duration (ms)	Frequency (Hz)	Beam diameter (mm)	Pulse shape
Center edge	157	0.9	2	0.55-0.8	Square
Center tube	155	0.9	2	0.55	Square
End	155	0.9	2	0.55	Square

Device-catheter friction: The friction forces resulting from pushing and pulling the assembled device through both a 5 and 6 F catheters (Cordis, 0.056” and 0.070” inner diameter respectively) were measured. The catheter was mounted onto the Instron tensile tester as pictured in Figure 3.9 and the assembled device was displaced through it at a rate of 100 mm/min in extension and compression modes. Water was injected to the catheter prior

to testing, and the friction forces between the two components were recorded at 1 Hz with the 50 N load cell (resolution 0.00025 N, lower limit 0.05 N) using BlueHill 3 software.

Load to push actuating SMP foam: The force required to push a crimped sample of tungsten-doped, actuating SMP foam out of the PTFE tube was also measured. Samples with the same dimensions as those used in the device assembly were crimped over a ~3 cm long piece of actone flat, and then were inserted into the PTFE tube. They were then submerged in a water bath at approximately 70 °C while the pusher, which was held by the manual grip of the Instron tensile tester, was displaced in compression at 15 mm/min until the foam was pushed out (n=3). The load was recorded with a 50 N load cell (resolution 0.00025 N, lower limit 0.05 N) at 1 Hz using BlueHill 3 software.

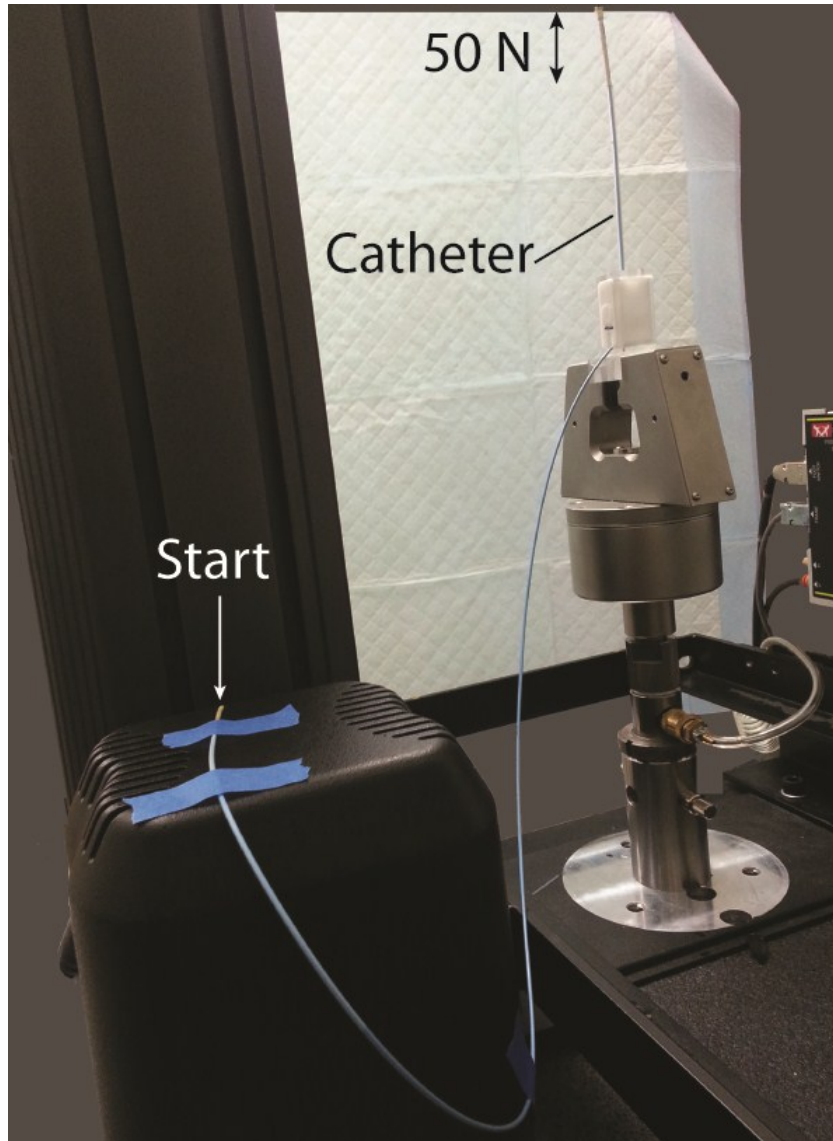


Figure 3.9. Experimental setup for device-catheter friction force measurements. The device inside the delivery system is inserted in the catheter such that both distal ends are flush with one another. The device is displaced by the movement of the crosshead in extension and compression for 30 mm when using a 5 F catheter, and 300 mm when using a 6 F catheter.

PTFE tube-needle attachment strength: To determine if the strength of the attachment between the PTFE tube and the 18 gauge needle was enough to sustain the load required to push the actuating SMP foam out of the PTFE tube, the load required to pull apart said

attachment was tested. An extension rate roughly five times higher (i.e., 75 mm/min) than the extension rate expected for pushing the actuating SMP foam out of the PTFE tube was used to simulate a worst case condition. Three samples were tested using the Instron tensile tester with the 50 N load cell. Data were acquired at 1 Hz via BlueHill 3 software.

Thrombus compressive stress: The same thrombus preparation protocol and thrombotic stroke model were used as described in Chapter II to test the feasibility of the hybrid thrombectomy device. The compressive mechanical properties of the resulting thrombi were measured using the 50 N load cell at a compression rate of 1 mm/min until reaching a maximum load of 15 N for three samples cut utilizing 10 mm diameter biopsy punches.

Animal testing

The pilot animal procedure was approved by the Texas A&M University Institutional Animal Care and Use Committee (IACUC) and was conducted according to its policies. An incision was made in the neck of a 25 kg Yorkshire pig, and the left carotid artery was accessed. A 10 F sheath was inserted utilizing a dilator, which was advanced through the distal aorta attempting to reach one of the femoral arteries. A piece of bovine thrombus, aged for 1.5 weeks, was cut using a 10 mm biopsy punch and was injected through the 10 F sheath utilizing saline solution at room temperature. The thrombus got lodged in the distal femoral artery, after which it elongated to roughly 50 mm. The thrombus was allowed to mature in this location for 15 minutes and contrast was injected subsequently to confirm the occlusion. Consequently, a 0.035” guidewire was advanced through the occlusion and a 5 F catheter was advanced over the guidewire such that its tip was placed distal to the thrombus. The

device was delivered through the 5 F catheter, and after roughly 1 minute of incubation at body temperature, the tungsten-doped SMP foam was deployed. The catheter and device were placed such that the thrombus was entrapped between the two, and their position was locked utilizing the Touhy borst adaptor on the hex cap screw. The entire device assembly was pulled towards the tip of the 10 F sheath, allowing for the restoration of blood flow. This procedure was repeated using 4 more devices.

Results

With this new design concept, thrombectomy devices with a deployment length of only 12 mm, and a crimped diameter of 1 mm were fabricated. Our initial goal was to fabricate a device that could be delivered through a 6 F catheter; however, this device and delivery system were small enough to fit through a 5 F catheter.

Proof of concept

All of the experiments (3/3) that were performed with the 1, 1.5 and 2× sized SMP foams were successful, i.e., the thrombus did not get dislodged through the bifurcation vessels. Still images of the thrombus extraction at different locations in the vessel model are shown in Figure 3.10 for the 1 and 2× cases. On the same figure is a graph of the load recorded during each thrombus removal trial. There was not a significant difference in the force recorded for the devices with 1 and 1.5× sized SMP foams; the maximum recorded load was 0.7 N. In contrast, the maximum recorded load for the devices made with 2× sized SMP foams was 1.85 N.

From the still images in Figure 3.10 it can be observed that the SMP foam tends to adhere to the thrombus, which aids in its retention. In the case of the 1× sized SMP foam, panel B depicts that the diameter of the SMP foam is too small to come in full contact with the thrombus. Thus, more than half of the thrombus body had an open path to flow into the second segment artery of the vessel model. However, the thrombus stayed attached to the SMP foam during the entire procedure. In order to further investigate this observation, one sample of SMP foam was placed on a thrombus that had been allowed to incubate at room temperature overnight. Bovine blood at 37 °C was added to the vial, and after four minutes the SMP foam and thrombus were taken out of the vial for inspection. Figure 3.11 pictures the SMP foam-thrombus interface while being held from the SMP foam only by a pair of tweezers. The adhesion between the SMP foam and the thrombus is evident.

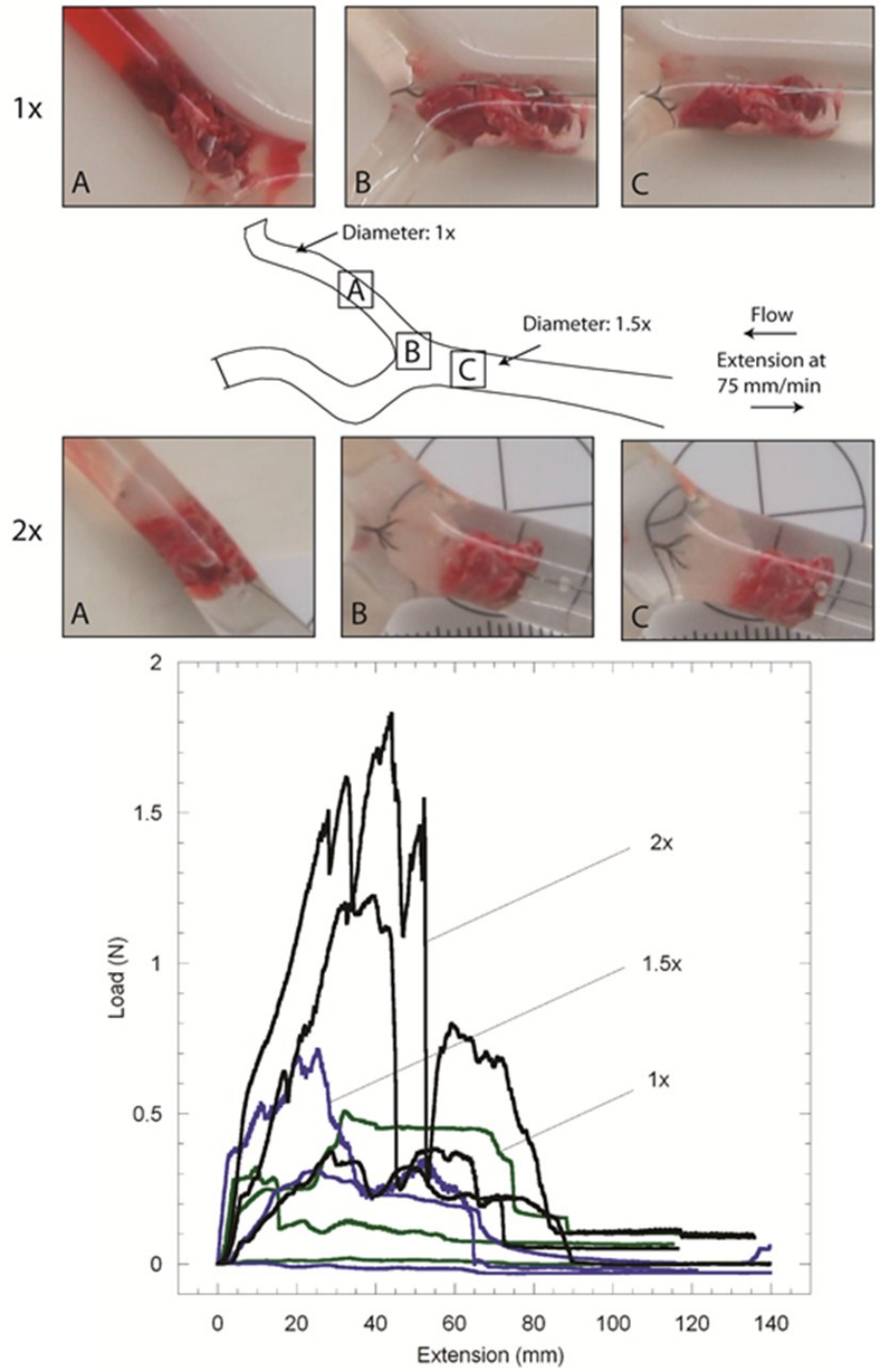


Figure 3.10. Bench-top thrombus removal results showing still images of thrombus removal procedure at different locations of the vessel model for devices with 1 and 2× sized SMP foams. Recorded load during the experiment for all devices tested (the diameter of occluded artery, second segment and parent artery are 5, 7 and 8 mm respectively).

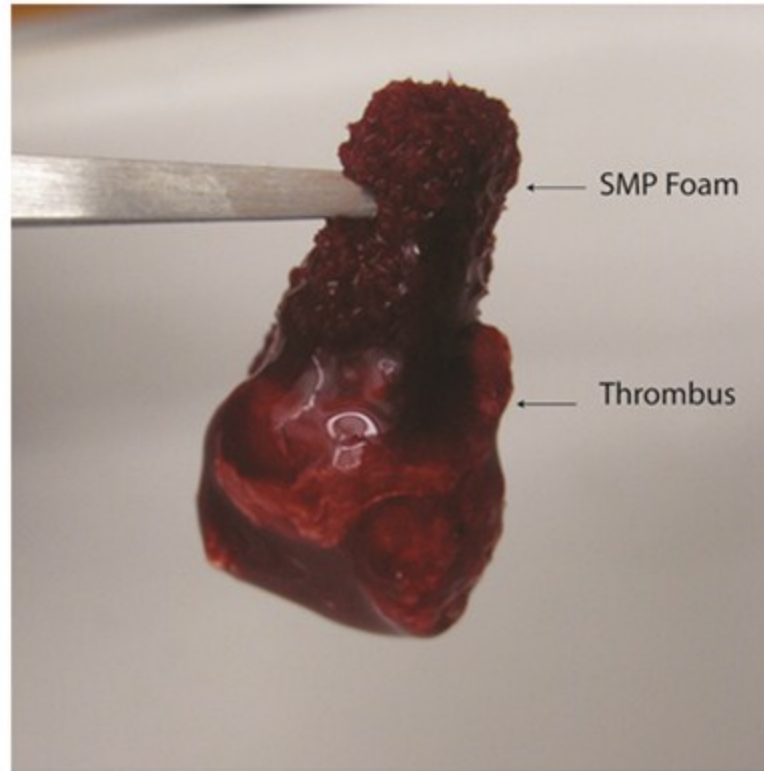


Figure 3.11. SMP foam adhesion to bovine thrombus after being incubated in a vial filled with bovine blood for 4 minutes. By holding only the SMP foam with tweezers it is evident that the thrombus had adhered to the SMP foam during the incubation.

The shape recovery and diameter expansion as a function of axial compression of the tungsten-doped SMP foam is shown in Figures 3.12 and 3.13 respectively. After being exposed to water at 37 °C for 90 seconds, the tungsten-doped SMP foam recovers 95% of its original shape. This SMP foam, while in rubbery state, only requires 0.13 N to achieve ~75% axial compression, resulting in roughly 45% radial deformation.

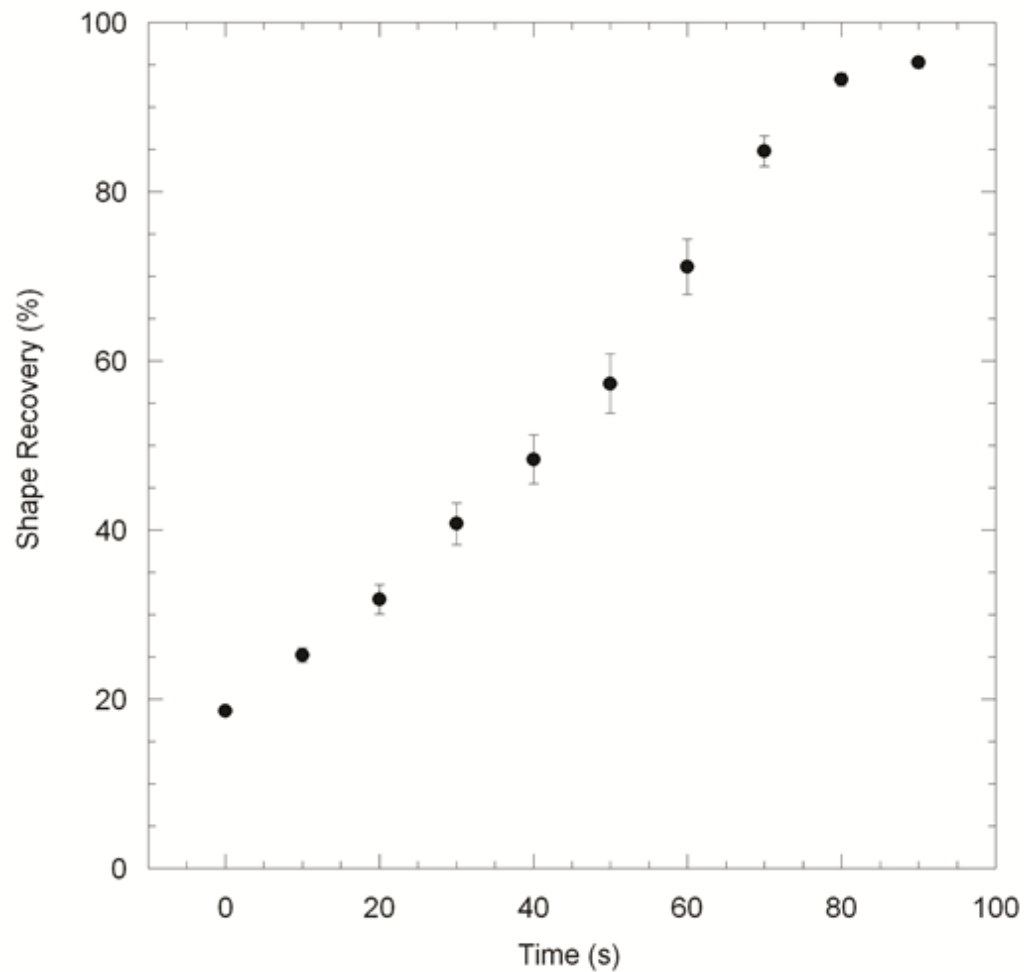


Figure 3.12. Shape recovery of tungsten-doped (4% by weight concentration) SMP foams in 37°C water. A maximum shape recovery of roughly 95% is observed.

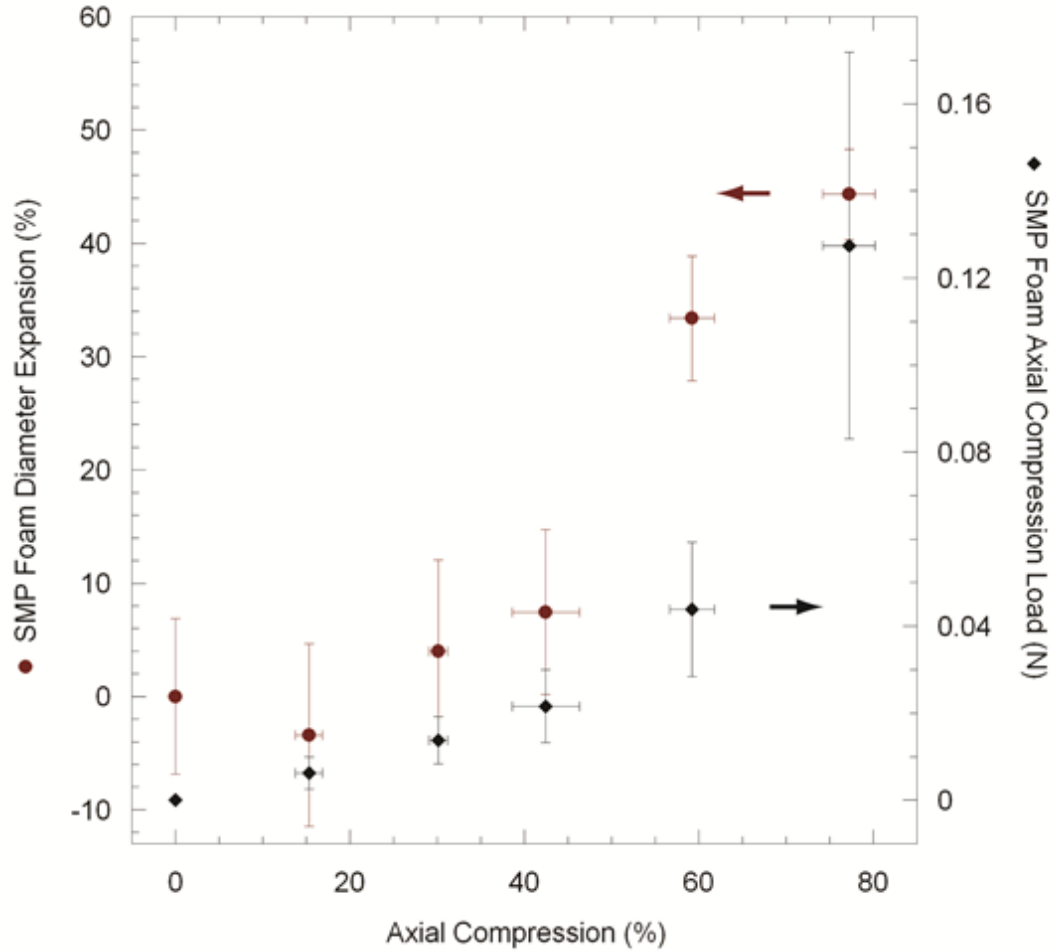


Figure 3.13. Diameter expansion as a result of axial compression and resulting compression load for tungsten-doped (concentration of 4% by weight) SMP foams while in rubbery state. An average axial compression load of roughly 0.12 N is required for the tungsten-doped SMP foam to achieve a diameter expansion of approximately 45%.

Bench-top testing

Weld tensile strength: Scanning electron microscopy (SEM) images of all three weld types are shown in Figure 3.14(A-C). The center edge weld, shown in Figure 3.14(A) fractured at an average load of 1.8 ± 0.97 N; in contrast, the center tube weld fractured at an average load of 25 ± 6.0 N. The SEM data shown in Figure 3.14(B) depicts how the center tube weld

made the nitinol tube conform to the actone in its lumen, almost acting like a shrink wrap without the need of exposing the actone to the laser beam. The end weld resulted in a smooth melt between the two components as shown in Figure 3.14(C). Its failure load was 14 ± 2.3 N. Because of the improved tensile strength of the last two welds compared to the first type, the center tube weld was implemented in the guidewire portion of the device, and the end weld for attaching the SNF to the guidewire.

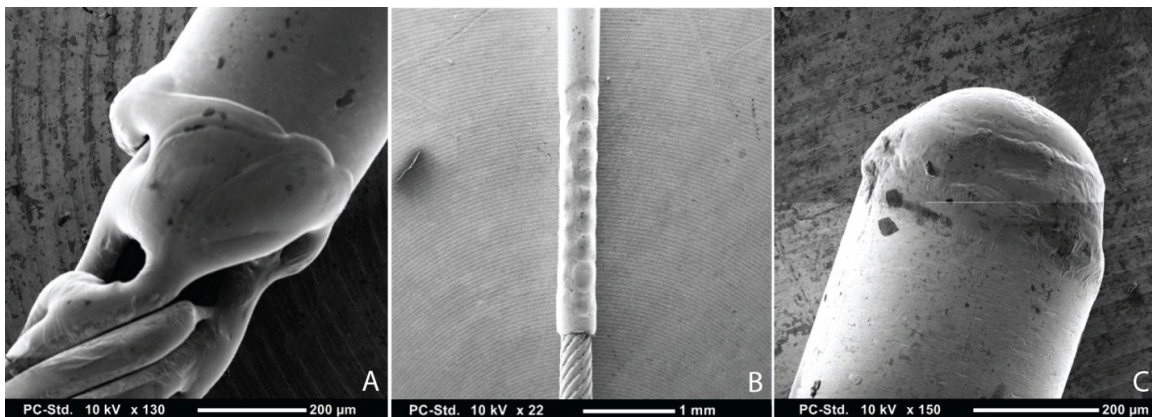


Figure 3.14. Laser welding of nitinol tube and actone flat braided wire at the edge of the tube (center edge weld) (A), on the tube only without contacting the actone flat (center tube weld) (B) and at the end of the flush nitinol tube-actone flat interface (end weld) (C).

Device-catheter friction: The friction forces between the assembled device inside the PTFE tube of the delivery system and a 5 F catheter over a 30 mm distance are plotted in Figure 3.15. The maximum average loads recorded during the pull and push cycles were 1.28 N and 1.48 N respectively. The pushing action required an overall higher amount of force compared to the pulling action.

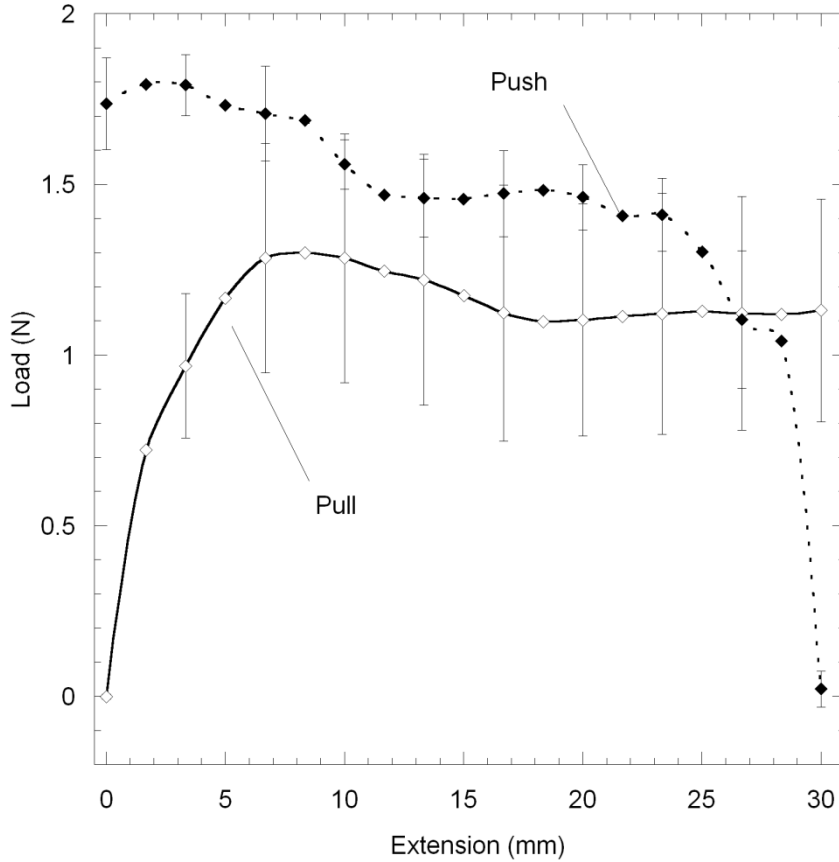


Figure 3.15. Load required to pull and push the assembled device through a 5 F catheter. The loads recorded during the push cycles are overall higher than the loads recorded during the pull cycles.

The friction forces resulting from pulling and pushing the assembled device inside the PTFE tube over a 300 mm distance through a 6 F catheter are depicted in Figure 3.16. The maximum average load recorded during the pull cycle was 0.21 N and that during the push cycle was 0.37 N. The overall pushing force was higher than the pulling load.

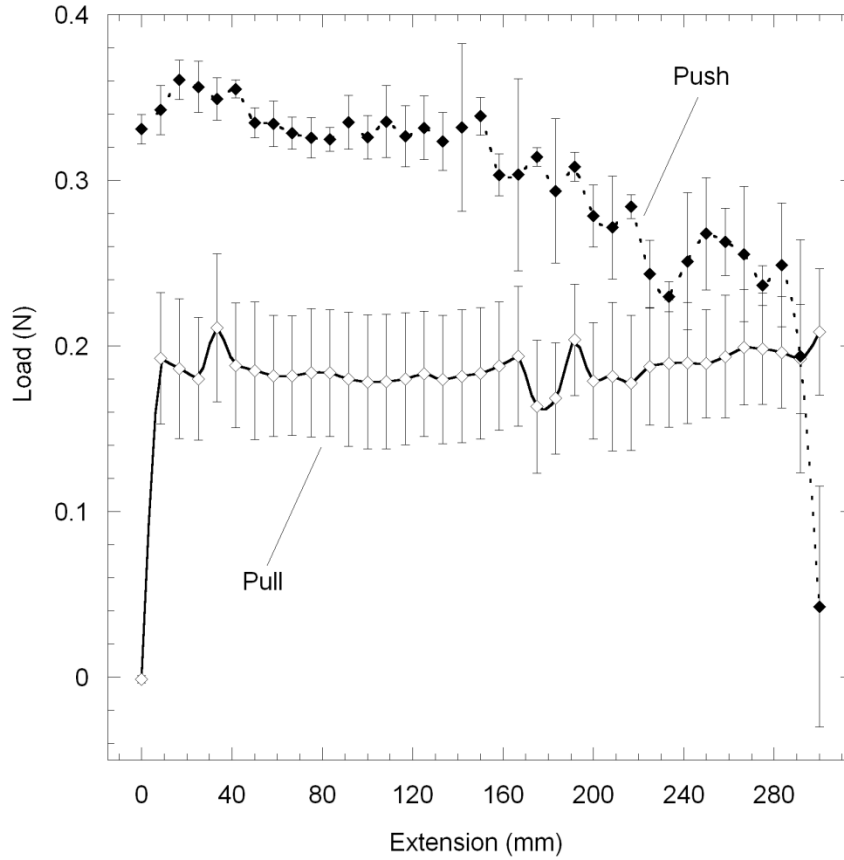


Figure 3.16. Load required to pull and push the assembled device through a 6 F catheter. As shown in the previous figure, the loads recorded during the push cycles are overall higher than the loads recorded during the pull cycles.

Load to push actuating SMP foam and to pull apart PTFE tube-needle attachment:

Figure 3.17 shows an example of the experimental procedure to measure the load required to push a sample of tungsten-doped SMP foam while it is actuating in hot water (6 mm diameter, 5 mm length) out of the PTFE tube. Figure 3.18 shows the average force required to push three SMP foams out the PTFE tube during actuation. The load ramped from 0 to a maximum of 3.2 N within the first 2 mm of compression. It then gradually decreased back to approximately 0 N after the whole SMP foam sample was completely pushed out of the

PTFE tube. This peak force was almost four times smaller than the force required to pull apart the PTFE tube-needle attachment, which was 11.9 ± 2.52 N.

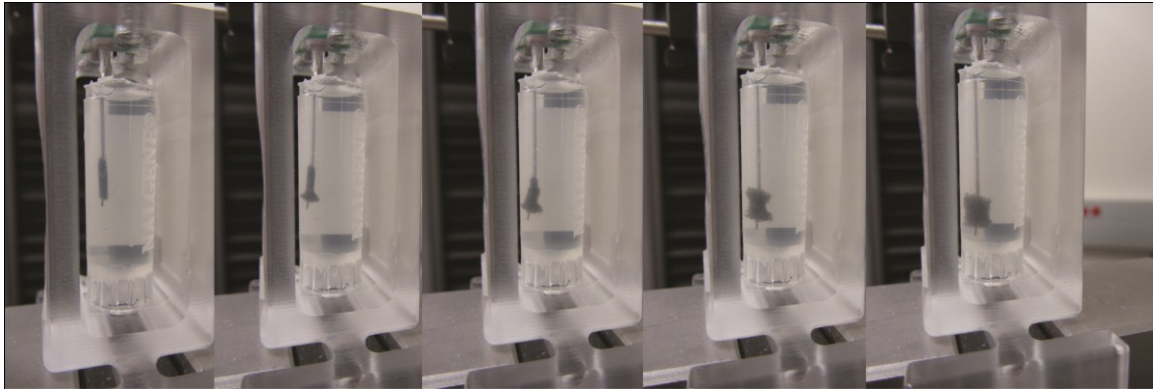


Figure 3.17. Example of one tungsten-doped actuating SMP foam sample push experiment in water at $\sim 70^\circ\text{C}$. Experiment was conducted by attaching the nitinol pusher to the crosshead of the Instron tensile tester, and displacing it at a rate of 15 mm/min in compression mode.

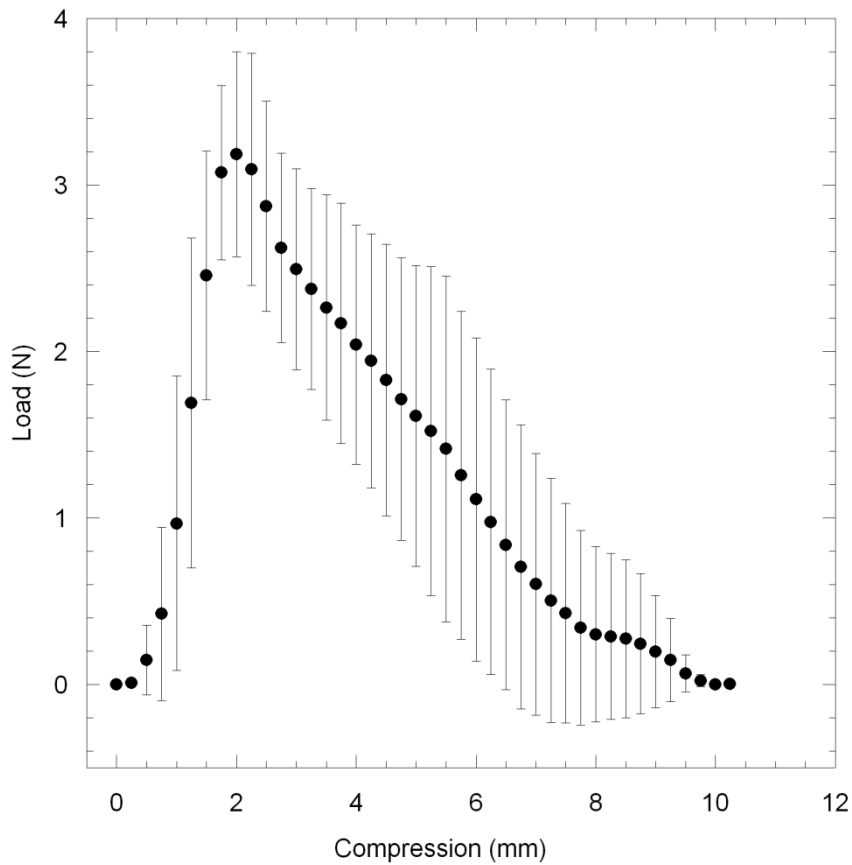


Figure 3.18. Average force required to push three actuating tungsten-doped SMP foam samples (6 mm diameter, 5 mm length) through the 18 AWG lightweight wall, medical grade PTFE tube. The strength of the PTFE tube-syringe attachment is 11.9 ± 2.52 N.

Thrombus compressive stress: Bovine thrombi containing 1 g of barium sulphate and 25 IU of bovine thrombin per 10 ml of bovine blood, required 83.3 ± 0.762 % strain to achieve a compressive stress of 0.19 MPa. These values are within the range of published stress-strain data for human red thrombi [91].

Animal results

During the animal study, only the first device was able to successfully remove the blood clot from its occluded location, as seen in Figure 6. After confirming occlusion (Figure 3.19(A-B)), the device was successfully deployed utilizing the hex cap screw pusher method, and approximately after 60 seconds, the tungsten-doped SMP foam was actuated (arrow in Figure 3.19(C)). As pictured in Figure 3.19(D-F), the clot extractor was able to move a ~50 mm long blood clot from the occluded location, to the tip of the 10 F sheath. Given that this sheath was too large for the vessels of this pig, we decided to keep in in place to avoid vessel dissection. Thus, the same procedure was repeated in the same vessel with a second device utilizing the same nitinol pusher and delivery mechanism. After the hex cap screw was fully rotated, the SMP foam was still inside the PTFE tube. This device was removed, and a new one was delivered through the catheter. This instance, a new nitinol pusher was used, and the SMP foam was successfully deployed out of the PTFE tube. As the device was pulled in an attempt to remove the blood clot, the device slid through the clot, failing to move it. Two more devices were delivered to remove the same clot; however, the devices slid through the clot as in the previous time.

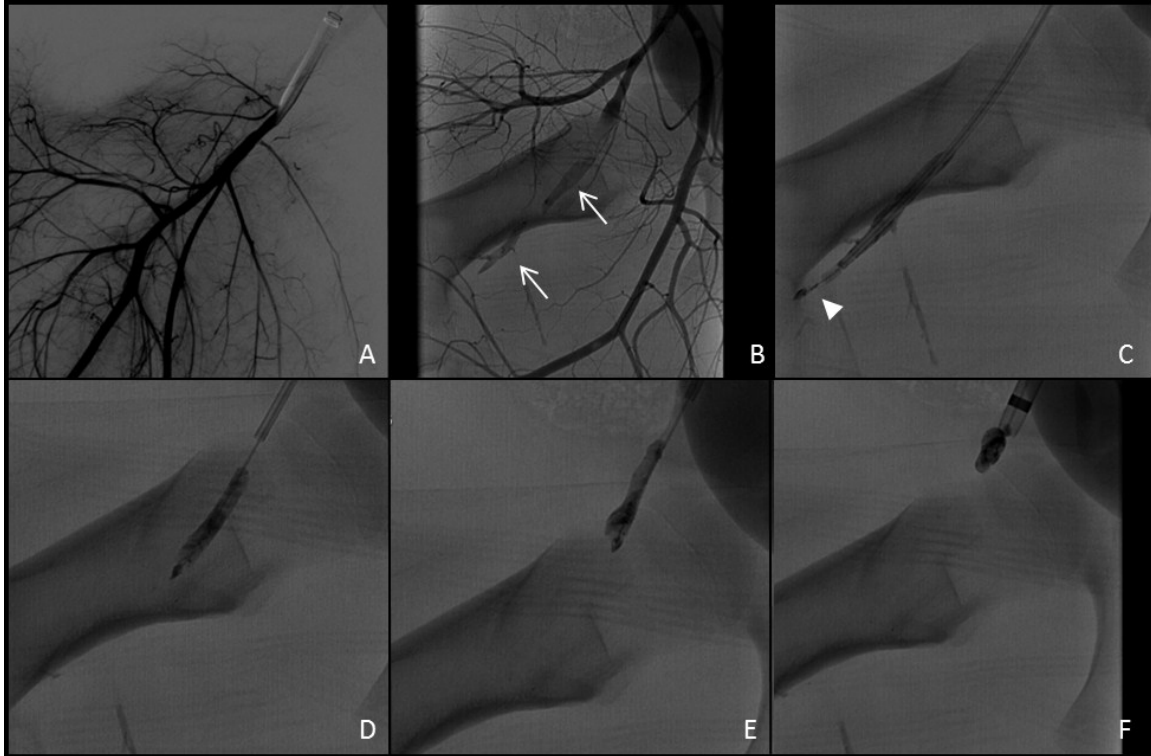


Figure 3.19. Control angiogram prior to injecting the clot (A) and after the clot was injected followed by contrast (B) (white arrows point at blood clots). Deployed device distal to the clot (C) (arrow points at SNF and actuated SMP foam), and device-clot interface during removal (D-F).

Discussion

A hybrid thrombectomy device made with SMP foam and nitinol has been proposed as an alternative design to the new wave of commercially available thrombectomy devices, stent retrievers. By combining the benefits of both types of shape memory materials, a thrombectomy device that is shorter and has a lower modulus in vessel contacting surfaces was fabricated. This reduction in length helps mitigate common complications that are associated with the use of thrombectomy stents that often result in treatment failure. The resulting hybrid thrombectomy device was able to move a ~50 mm long clot from its occlusion site, to the delivery sheath, revascularizing the femoral artery of a pig.

In a study by Castaño et al. (2010), the Solitaire stent failed to achieve restoration of blood flow in all the cases in which the blood clot was longer than the stent [92]. Conversely in our animal study, our proposed thrombectomy device was able to hold a thrombus that was almost 5 times its length, and almost twice as long as any of the stent retrievers. While this positive result was only observed in the first device tested, the fact that the clot was not successfully removed in the following cases is not necessarily attributable to device failure. One possible explanation for the missed clot removals could be that the occluded vessel got dilated. From the angiogram images it was observed that the diameter of the occluded vessel got on average 35% larger in the subsequent clot extraction attempts, requiring the use of a device with a larger SMP foam sample that was not available. This reason, exacerbated by the fact that the multiple catheter passes through the clot might have created a channel that made it easier for the actuated SMP foam to slip through it, was a major role player in the outcome of the devices that were tested last.

The bulk of this work was devoted to verifying that the design outputs met the design inputs. Because this device has gone through multiple design iterations as shown in Appendix A, the number of design requirements has had to broaden to accommodate the changes. Thus, the final design requirements were based on user needs, information about predicate devices, and information in the literature; and are applicable to the design presented in this chapter. With this information, performance specifications and verification tests were outlined as listed in Table 3.4. The most important parameters for the SMP foam were crimped diameter, shape recovery and radial deformation as a function of axial compression. The design requirements were within specification only for the SMP foam with the smallest average cell size (F44), and expectations were exceeded by the implementation of the tungsten-doped SMP foam, primarily because it had an even smaller average cell size. The parameters of the nitinol backbone were also within specification, and in some cases, the results exceeded the expectations. For example, the outer diameter of the non-actuated nitinol backbone was 0.4 mm, which is 0.06 mm smaller than the proximal core wire diameter of its predicate device, Trevo® according to the Trevo Retriever 510(k) summary [79]. Additionally, the tensile data revealed that the center welds are a novel method of attaching nitinol braided wire (actone) to nitinol tube, as its fracture load was 14 times higher compared to the fracture load of the typical edge welding method. For the delivery system, the tensile strength of the PTFE tube-needle attachment was also within specification, as it resisted a load that was 3.7× the load required to push actuating tungsten-doped SMP foam out of the PTFE tube. Finally, the deployment length of the device was 3 mm below the maximum accepted value defined in the design inputs, showing a significant advantage over all predicate devices. The force required to pull the devices through a 6 F catheter was also below the maximum accepted

value defined in the design inputs, and is comparable to the friction measured between a 0.47 mm inner diameter microcatheter and 0.41 mm guidewire in a tortuous path [86].

SMP foam adhesion to the thrombus was observed during the bench-top thrombectomy trials, and we believe this phenomenon is caused by the high surface area of the SMP foams that is in contact with the thrombus, compared to the surface area of contact between the thrombus and a nitinol-based device. The ability to size the portion of the thrombectomy device that is in contact with the thrombus during removal according to the cross-sectional area of the occluded vessel is an advantage of this device compared to commercially available predicate thrombectomy devices because it helps in thrombus retention during removal. Thrombus retention is often poor in commercially available devices, which is why thrombus dislodgement is found as a major drawback in mechanical thrombectomy in the literature [2, 7].

A major concern of the implementation of distal devices for the treatment of stroke is that, as the catheter is advanced through the thrombus, there is a high probability of small fragments getting cut off the thrombus and migrating distally. We have observed this issue in our bench-top experiments; while in some cases the fragment adhered to the SMP foam, in others it got flushed distally with the flow of water. Even though this problem is present in every distal device, using large catheters with high profiles (i.e., edges that do not transition smoothly) increases the probability of thrombus fragmentation as well as the size of the fragments.

Table 3.4. Performance specifications and verification tests for the SMA-SMP thrombectomy device.

Device component	Design requirement	Units	Target value	Accepted range	Criteria	Method of verification	Result
SMP foam	Crimped diameter	(mm)	0.6	0.6-1	Catheter delivery	Verify that crimped SMP foam fits inside PTFE tube	Passed for 6 mm diameter tungsten-doped SMP foams
	Shape recovery	(%)	95	80	Full occluded vessel lumen conformation when actuated	Allow SMP foam to passively actuate in 37 °C water and acquire images every 10 s. Perform three diameter measurements at each time point utilizing ProGres Capture Pro software with proper calibration. Repeat with three samples.	Passed for tungsten-doped SMP foam
	Radial deformation as a function of axial compression	(%)	30	10	Ability to conform to vessel lumen for sections that are tapered out	Compress the actuated SMP foam in 37 °C water and acquire images at every compression point. Perform three diameter measurements at each time point utilizing ProGres Capture Pro software with proper calibration. Repeat with three samples.	Passed for tungsten-doped SMP foam

Table 3.4 Continued.

Device component	Design requirement	Units	Target value	Accepted range	Criteria	Method of verification	Result
Nitinol backbone	Outer diameter of non-actuated SNF and guidewire	(mm)	0.8	0.8-1	Catheter delivery	Measure with calibrated caliper	Passed
	Diameter of actuated SNF	(mm)	2.5	2.5-2.7	Risk of vessel injury upon contact	Acquire images and measure diameter with ProGres Capture Pro software with proper calibration	Passed
	Fracture load of center weld	(N)	>10	8	Maximize fracture load with respect to bench-top thrombus extraction load of 1.85 N	Perform tensile test at same extension rate used for thrombus extraction experiment	Passed for center tube weld
	Fracture load of end weld	(N)	>10	8	Maximize fracture load with respect to bench-top thrombus extraction load of 1.85 N	Perform tensile test at same extension rate used for thrombus extraction experiment	Passed

Table 3.4 Continued.

Device component	Design requirement	Units	Target value	Accepted range	Criteria	Method of verification	Result
Delivery system	Tensile strength of PTFE tube-syringe attachment	(N)	12.8	6.4	Maximize tensile strength of attachment with respect to load to push actuating SMP foam of 3.2 N	Perform tensile test at extension rate 5 times higher than rate used to push SMP foam out of the PTFE tube	Passed
Assembled device	Deployment length of device	(mm)	8	<15	Comparison against commercially available devices, which require at least 15 mm of deployment length	Acquire image and measure with ProGres Capture Pro software with proper calibration	Passed
	Pull and push force required for advancement through 6 F catheter in a tortuous path	(N)	0.3	0.3-0.5	Catheter maneuverability	Measure with tensile tester in extension and compression modes at 100 mm/min	Passed

Therefore, future iterations of the thrombectomy device should incorporate the use of a sheath and a dilator to provide a smooth transition from the diameter of the catheter to the tapered tip of the dilator to access the thrombus prior to device deployment.

Conclusion

A thrombectomy device made with SMP foam and nitinol has been proposed as an alternative mechanical thrombectomy treatment for the 95% of patients who are unable to receive tPA for the treatment of acute ischemic stroke. Design features such as a shorter working length, higher surface area of contact with the thrombus normal to the direction of blood flow, and low rubbery modulus in vessel-contacting surfaces, address complications associated with most current devices, such as difficult maneuverability, poor clot hold and vessel damage. The ability to recanalize a vessel that was occluded with a 50 mm long blood clot in a porcine animal model indicates the potential of this novel thrombectomy device to outperform its predecessors.

CHAPTER IV

SMP FOAM FILLING DEVICE: POROUS MEDIA PROPERTIES

CHARACTERIZATION

The fabrication of ultra-low density SMP foams with high volume expansion capabilities enabled the redesign of the thrombectomy device to the hybrid SMP-SMA device that was presented in the previous chapter. In addition to being utilized as components of the thrombectomy device, these SMP foams are being investigated as an alternative aneurysm treatment technique to the insertion of embolic coils, e.g., GDCs. The goal of both techniques is the reduction of blood flow into the aneurysm and the subsequent formation of a stable thrombus, which results in the isolation of the aneurysm from the vasculature, thereby preventing its future rupture [4, 5, 18, 27]. This chapter presents a porous media approach to quantify the resistance to flow imposed by the SMP foams and coils imitating the geometry of clinical embolic coils.

Introduction

Despite the thousands of patients who have been treated with the coiling method with positive results, there are still considerable limitations to this treatment technique. The most important are incomplete filling of the aneurysm resulting in low coil packing densities, coil compaction over time, and coil migration to the parent artery [47-49]. For example in aneurysms with diameter greater than 6 mm, the maximum packing density is on average 21% [50].

To overcome these challenges, SMP foams have been proposed as an alternative treatment [55, 84, 88, 93, 94]. The main advantage of this method is that SMP foams show up to 70 times volume expansion, which enables them to be delivered through a microcatheter, while possessing the ability to completely fill the aneurysm upon actuation [55, 94]. The flow behavior within the treated aneurysm can be further customized by utilizing SMP foams that have been mechanically reticulated, i.e., pierced with a needle. This process helps enhance the flow through the SMP foams by puncturing residual membranes.

The success of the endovascular treatment of aneurysms begins with the formation of a stable thrombus. It has been known for over 40 years that thrombosis within a treated aneurysm is not only due to biochemical reactions, but also due to altered fluid dynamics [4, 27]. Among the hemodynamic factors that induce thrombosis, blood stasis is one of the most important [18, 27]. Many studies have implemented a porous media approach to model the flow within an aneurysm filled with embolic coils with the goal of evaluating thrombosis [95-98]. The same approach has been taken for simulations utilizing virtually reticulated SMP foam [99].

The porous media model that we employed in this study is the Forchheimer-Hazen-Dupuit-Darcy (FHDD) equation:

$$-\frac{\partial P}{\partial x} = \frac{\mu}{K} v_o + \rho C v_o^2, \quad (4.1)$$

where $\frac{\partial P}{\partial x}$ is the pressure gradient across the sample in the direction of flow (Pa/m), μ is the dynamic viscosity of the fluid (Pa·s), K is the intrinsic permeability (m^2), v_o is the Darcy velocity (flow rate divided by cross-sectional area of the sample) (m/s), ρ is the density of the

fluid (kg/m^3), and C is the form factor (m^{-1}). Permeability and form factor are constitutive geometrical parameters of the porous matrix and depend on the contributions of viscous drag and inertial losses, respectively [100-102]. Thus, the permeability is inversely proportional to the surface area of contact between the solid and the fluid, and the form factor is proportional to the projected cross-sectional area of the obstructing solid perpendicular to the direction of the fluid flow. In the present study, we compared the permeability and form factor of mechanically-reticulated SMP foams to those of mock embolic coils (MECs), which are inexpensive, non-clinical coils that approximate the diameter, distribution, and packing density of clinical embolic coils. Strictly from a fluid dynamics perspective, the purpose of this work is to evaluate the potential of SMP foams as embolic devices or components of embolic devices.

Materials and methods

Flow system and measuring apparatus

An *in vitro* closed flow loop was constructed to produce a measurable pressure gradient across either the SMP foam or the MEC sample at a given flow rate (see Figure 4.1). It was comprised of a gear pump (Chemsteel R106, Oberdorfer), a servo motor (750 W M-series, Applied Motion Products), a motor controller (BLuAC5-Q, Applied Motion Products), a testing chamber, a fluid reservoir of room temperature water elevated by 30 cm above the testing chamber, and two high accuracy pressure transducers (PX429-2.5G5V, Omegadyne Inc with accuracy rated at $\pm 0.08\%$ of the baseline maximum). The output voltage of the pressure transducers was recorded at 1 Hz through a data acquisition system (USB6251,

National Instruments) to a computer disk for 120 seconds. The flow rate was measured by hand using a stop watch (Traceable, VWR) and a graduated cylinder (250 ml capacity).

Two distinct chambers were required for the characterization of both media. The chamber for the SMP foam samples was fabricated from polycarbonate (inlet and outlet) and PMMA (body) using the Roland CNC. As pictured in Fig. 4.2(A), the body of the chamber was designed to enclose a sample holder (inner diameter and outer diameter 15.1 mm and 18.9 mm, respectively), to which SMP foam samples were adhered prior to being tested. The dimensions of the SMP foam samples were chosen such that they were large enough to minimize any effects of heterogeneities in their structure. Using a 3D printer (Fortus 360, Stratasys), the sample holders were fabricated with three 4×4 mm pressure port openings, 15 mm apart of one another.

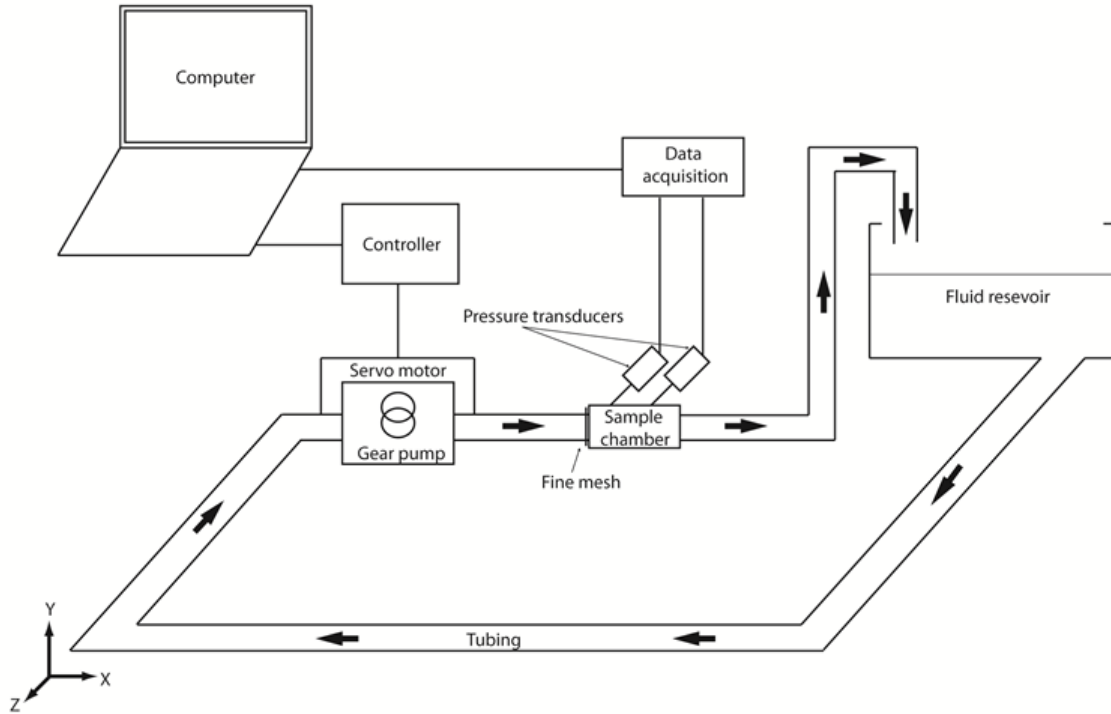


Figure 4.1. Flow system constructed to measure the pressure gradient across SMP foam and MEC samples for a given flow rate range.

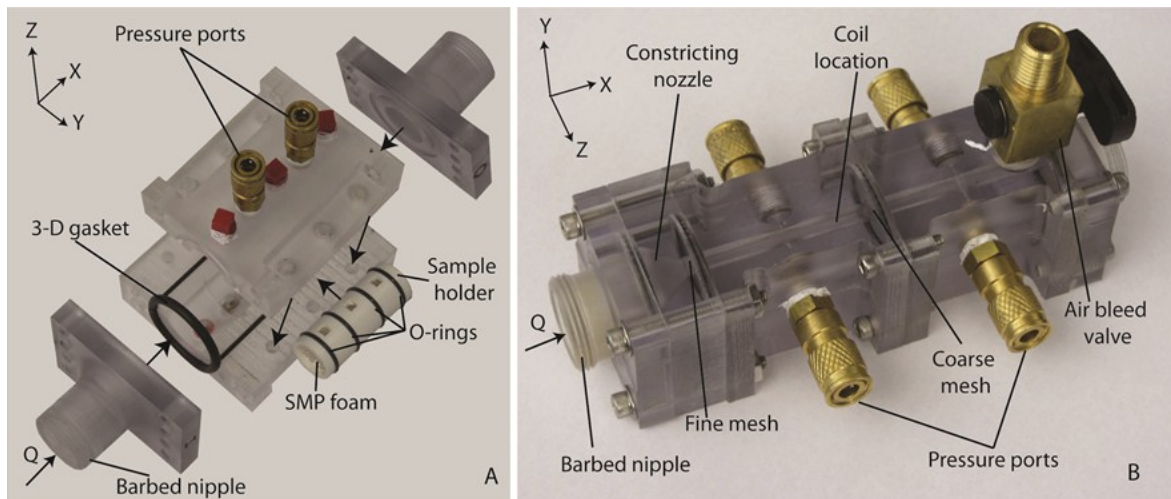


Figure 4.2. Exploded view of SMP foam chamber with arrows showing how pieces are assembled (A) and assembled MEC chamber (B).

Only the upstream and downstream pressure ports were utilized in the measurements. O-ring grooves were machined in both the chamber body and the sample holder to ensure repeatable chamber alignment and to seal the pressure ports. A fine mesh (stainless steel 316, 0.1 mm wire diameter, 0.4 mm² squares) was installed at the inlet of the chamber to homogenize the flow.

The chamber for measurement of MECs was fabricated from polycarbonate using the Roland CNC (see Figure 4.2(B)). A constricting nozzle was machined at the inlet to provide a smooth transition from the 20 mm diameter tubing to the 6 mm diameter of the chamber lumen, which is within the range of diameters of ISAs [50]. A Fine mesh (stainless steel 316, 0.1 mm wire diameter, 0.4 mm² squares) was installed downstream of the nozzle to homogenize the flow. Two pressure ports 50 mm apart were utilized to connect the pressure transducers. A coarse mesh (stainless steel 316, 0.25 mm wire diameter, 2.3 mm² squares) was installed between the coil location and the second pressure transducer to hold the MECs in place during the test. The pressure gradient across this mesh was subtracted from the pressure gradient data for each MEC sample.

Sample preparation

Two SMP foams with different cell sizes were evaluated in this study. They were labeled as foam S, for small average cell size, and L, for large average cell size (see Figure 4.3). They were made following the same chemistry and cleaning protocol as the foams described in the previous chapter. Foam S had a T_g , measured by DSC, of 59.1 °C, an average cell size of 0.7 mm and a porosity of 98%. Foam L had a T_g by DSC of 55.6 °C, an average cell size of 1.1

mm and a porosity of 98% (refer to [55] for porosity calculation). The samples were cut from a large piece of dried SMP foam using a drill press with a $\frac{3}{4}$ " hole saw attachment. Then, the appropriate length was achieved by cutting it with a straight edge razor. The resulting SMP foam samples had a diameter of ~ 16 mm and a length of 49 mm. For mechanical reticulation, the SMP foam samples were perforated utilizing a stainless steel acupuncture needle (Kingli) with a diameter of 0.3 mm. In order to achieve mechanical reticulation in a repeatable manner, we 3D printed a hollow cylinder with a cap and utilized it as a template guide. The hollow cylinder had 1600 radial holes and 124 axial holes with a hole diameter of 0.9 mm and was designed so that the SMP foam samples fit securely within it during reticulation. Four scenarios of mechanical reticulation were produced, and they are reported as a function of hole density (ζ), i.e., the number of holes pierced per unit area of the surface of the SMP foam sample. The resulting hole densities were 0.9, 1.7, 3.5 and 6.9 $E+05$ holes/m². In all four cases, the pierced holes were evenly distributed along the surface of the SMP foam sample. Figure 4.3 illustrates a true-scale representation of the four hole densities overlaid on each foam type, and Figure 4.4 shows the piercing patterns that were followed. Following mechanical reticulation, the SMP foam samples were fixed to the sample holders by being crimped to a diameter of roughly 8 mm and then allowed to expand inside the sample holder, which had been evenly coated with a thin layer of water resistant epoxy (Marine Epoxy, Loctite). The epoxy was allowed to cure for at least 2 hours prior to beginning each test. Since long term exposure to water can potentially affect the mechanical properties of the SMP foams, data were acquired at 0, 2, and 4 hours of water exposure times [55, 89].

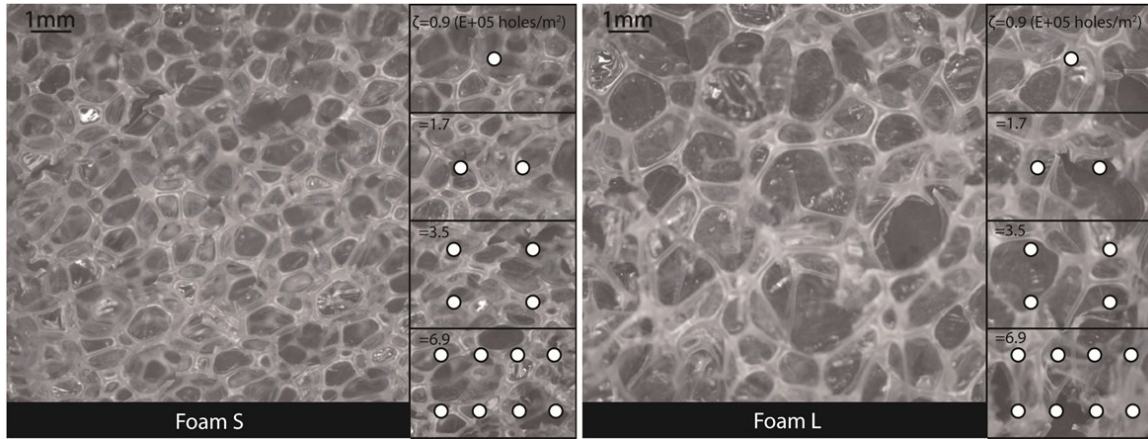


Figure 4.3. SMP foams prior to mechanical reticulation (2.5× magnification) and true-scaled overlaid illustrations of the four scenarios of mechanical reticulation and their corresponding hole densities. Hole density is calculated by dividing the number of holes pierced over the surface area of the 3D-printed template.

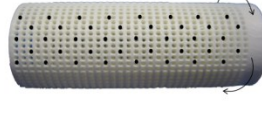

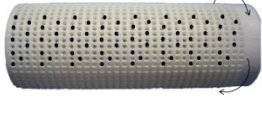





Number of radial holes	Number of axial holes	Radial ζ (holes/m ² E+05)	Axial ζ (holes/m ² E+05)
200 	15 	0.85	0.86
400 	30 	1.7	1.7
800 	62 	3.5	3.4
1600 	124 	6.9	6.9

Figure 4.4. Pattern of holes pierced in each of the four scenarios of mechanical reticulation. Resulting radial and axial hole densities were approximately the same.

MEC samples were prepared by randomly coiling different known lengths (i.e., 0.28, 0.47, 0.59 and 0.71 m) of copper wire with a diameter of 0.39 mm, which is near the center of the range of commercially available embolic coil diameters [5]. Each MEC sample was then packed inside the measuring chamber one at a time as shown in Figure 4.5. Packing density (η) was calculated as the ratio of the volume of the coil to the cylindrical bounding volume of the coil mass. The achieved packing densities were 11, 16, 23 and 28%.

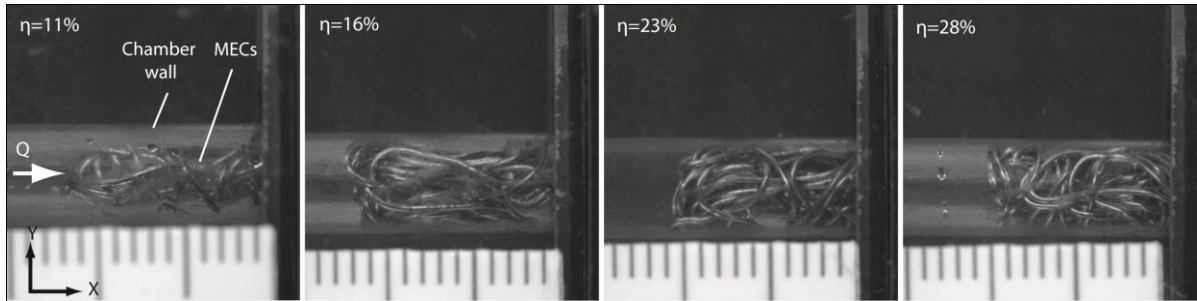


Figure 4.5. Packed MECs in measuring chamber. Packing density is calculated by the ratio of the coil volume to the cylindrical bounding volume of the coil mass.

Sample characterization

For each sample, we implemented a second-order least squares fit to the data of pressure gradient plotted against Darcy velocity. Then we calculated the values of permeability, K , and form factor, C , using Eq. 4.1 (see Appendix B for Matlab code). A total of nine values of v_0 and their corresponding pressure gradients were utilized for the calculations. Measurements were made to check for hysteresis, which could have been caused by sample deformation during testing [102]. To quantify other potential sources of measurement

variability arising from the instrumentation, an uncertainty analysis was performed based upon the root-sum-squares method (see Appendix B for uncertainty analysis calculation) [103, 104].

The Re of these measurements was defined as the ratio of inertial forces and viscous forces (from Eq. 4.1) [100, 105]

$$Re = \frac{\rho v_0 KC}{\mu}. \quad (4.2)$$

Non-dimensionalization of Eq. 4.1 by $C\rho v_0^2$ yielded

$$\frac{-\frac{\partial P}{\partial x}}{C\rho v_0^2} = \frac{1}{Re} + 1 = f, \quad (4.3)$$

where the term to the left of the equal sign is the friction factor, f [105, 106]. Logarithmic plots of friction factor against Re provide information about the flow regime in which SMP foams and MECs were tested [107].

Results

Plots of pressure gradient against Darcy velocity are shown in Figures 4.6(a,b) and 4.7 for SMP foams and MECs respectively. There was no evidence of compression-induced hysteresis for either media. Additionally, moisture uptake from water exposure of the SMP foams had little, if any, impact on the measured quantities. Therefore, data from all water exposure times were used in the least squares fits for the SMP foams. For all the regressions, the coefficients of determination for both media were greater than $R^2=0.99$.

(a)

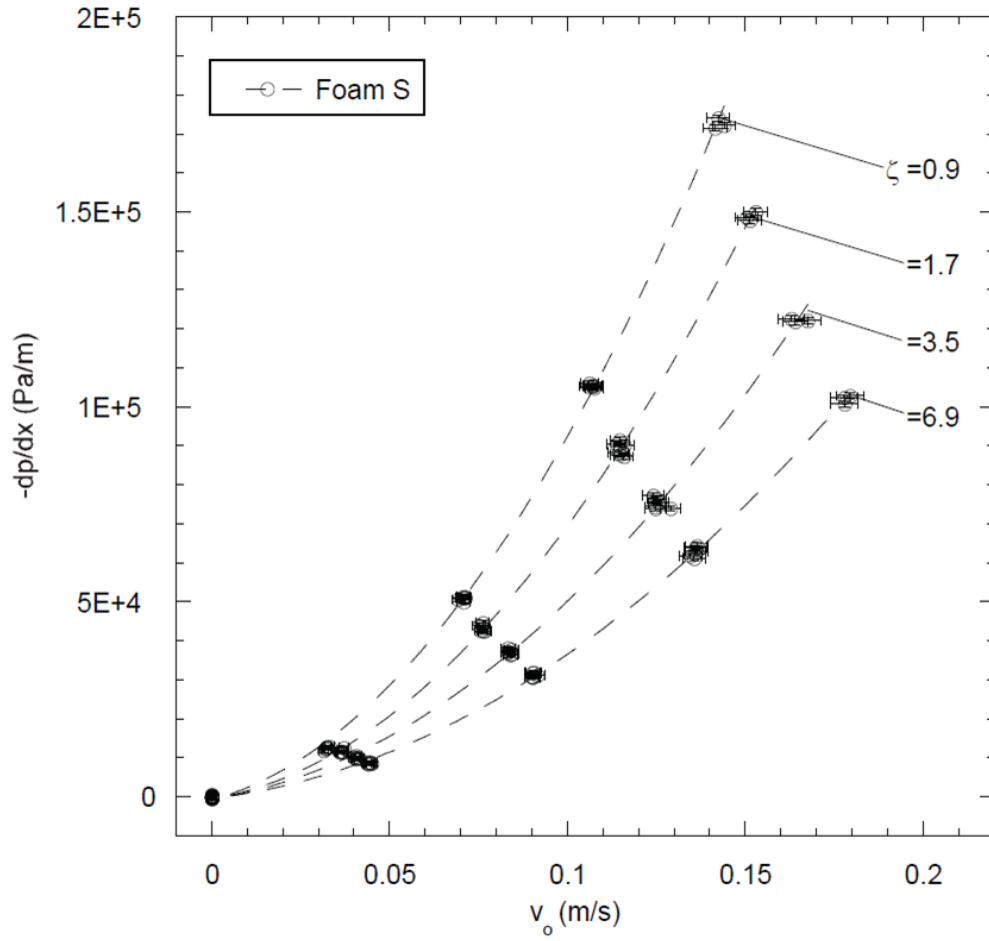


Figure 4.6. Pressure gradient versus Darcy velocity (v_0) of SMP foam S (a) and L (b) (hole density (ζ) with units $\text{E}+05$ holes/ m^2). As the hole density increases, the pressure gradient across the samples decreases for both SMP foam types.

(b)

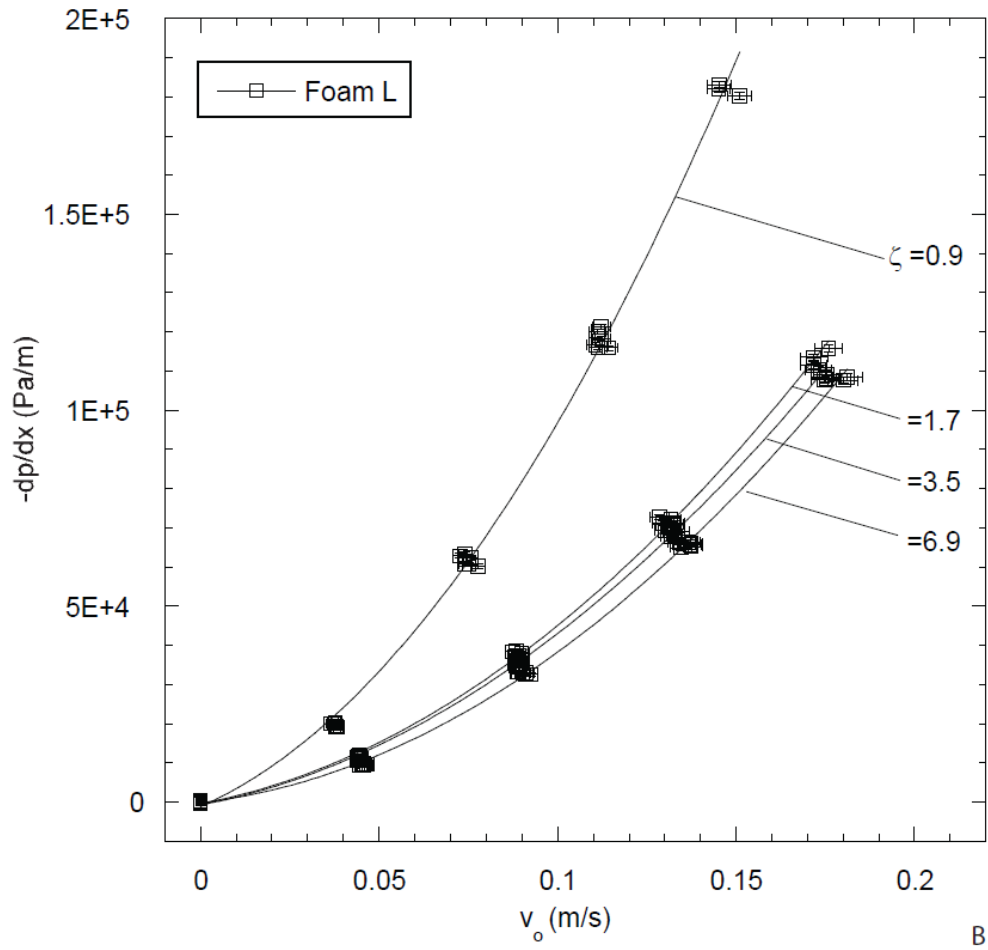


Figure 4.6. Continued.

For the SMP foams, the pressure gradient at v_{0_max} of foam S was 173E+03 Pa/m and that of foam L was 182E+03 Pa/m for the samples with the least amount of mechanical reticulation (i.e., $\zeta=0.9E+05$ holes/m²). As hole density was increased to 6.9E+05 holes/m², the pressure gradient at v_{0_max} decreased to 102E+03 and 108E+03 Pa/m for foams S and L respectively. For the MECs with $\eta=28\%$, the pressure gradient at v_{0_max} was 169E+03 Pa/m and it decreased to 58.0E+03 Pa/m for $\eta=11\%$.

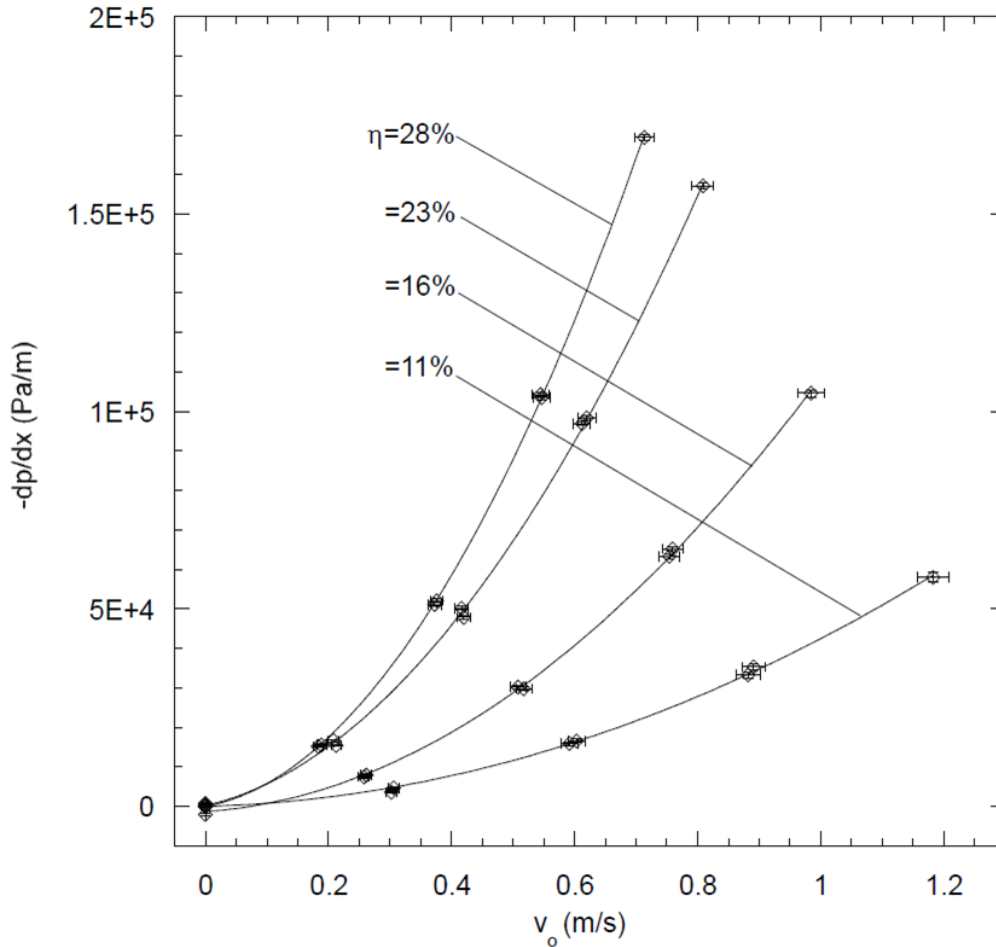


Figure 4.7. Pressure gradient versus Darcy velocity (v_0) of MECs (packing density (η)). The higher the packing density of the MECs, the higher the pressure gradient across them.

Plots of permeability and form factor are shown in Figures 4.8 and 4.9 respectively. The differences in permeability and form factor for the SMP foams as a result of varying the average cell size were not as pronounced as those resulting from varying the amount of mechanical reticulation. As would be expected, higher amounts of mechanical reticulation resulted in overall higher permeability and lower form factor values. For foam S, permeability values ranged between $5.70\text{E-}09$ and $12.4\text{E-}09 \text{ m}^2$, and form factor values were between $2.72\text{E+}03$ and $7.26\text{E+}03 \text{ m}^{-1}$. For foam L, permeability and form factor values ranged

from $3.25\text{E-}09$ to $11.5\text{E-}09$ m^2 and $2.80\text{E+}03$ to $6.19\text{E+}03$ m^{-1} respectively. For the MECs, there was a change of one order of magnitude in permeability and form factor for samples with $\eta=11\%$ versus samples with $\eta=28\%$; permeability and form factor ranged from $40.5\text{E-}09$ to $561\text{E-}09$ m^2 and $0.0409\text{E+}03$ to $0.296\text{E+}03$ m^{-1} respectively.

Figure 4.8 depicts additional permeability data for embolic coils (diameter of $0.25\text{E-}3$ m) that were considered in the simulations of Kakalis et al. (2008) [95]. In their study, the Kozeny theory was implemented to calculate the permeability of embolic coils using the porosity and specific surface, which is the total interstitial surface area per unit bulk volume of the porous medium [95, 107]. These calculated permeability values follow a similar trend to that of the MECs, but are on average four times smaller. When the measured permeability and form factors are used to non-dimensionalize the pressure gradient and Darcy velocity, the resulting friction factors and Reynolds numbers for both SMP foams and MECs collapse onto the relationship specified by Eq. 4.3 for Reynolds numbers ranging from approximately 1 to 35 (Fig. 4.10).

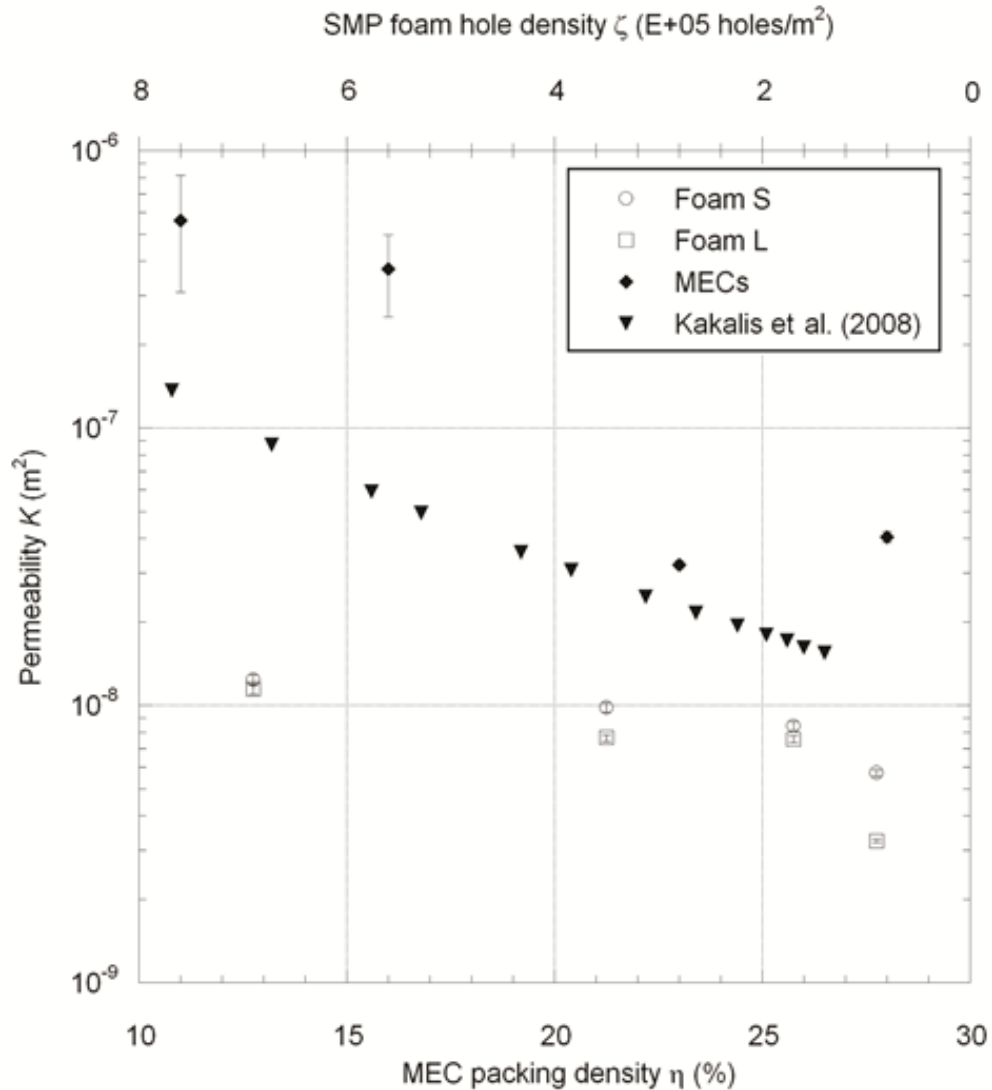


Figure 4.8. Permeability of SMP foams and MECs. The permeability of the MECs is higher than the permeability of both SMP foam types in all cases. Decreasing the packing density results in a decrease in permeability. Similarly, decreasing the number of holes pierced (i.e., decreasing the hole density) also results in a decrease in permeability. The permeability data for embolic coils that was calculated using the Kozeny theory by Kakalis et al. follows the same trend as our measured data.

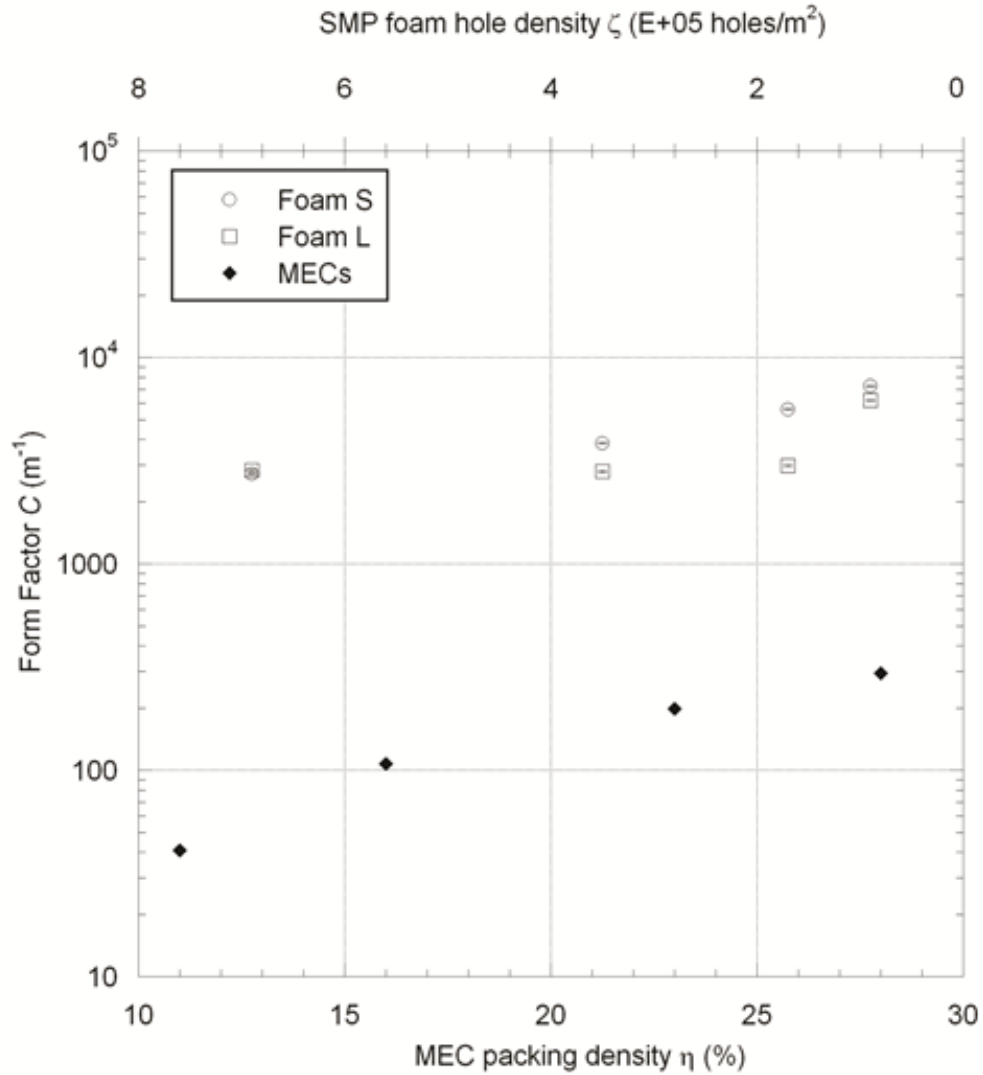


Figure 4.9. Form factor of SMP foams and MECs. The form factor of both SMP foam types is higher than that of the MECs in all cases, and it increases as the hole density of the SMP foams decreases and as the packing density of the MECs increases.

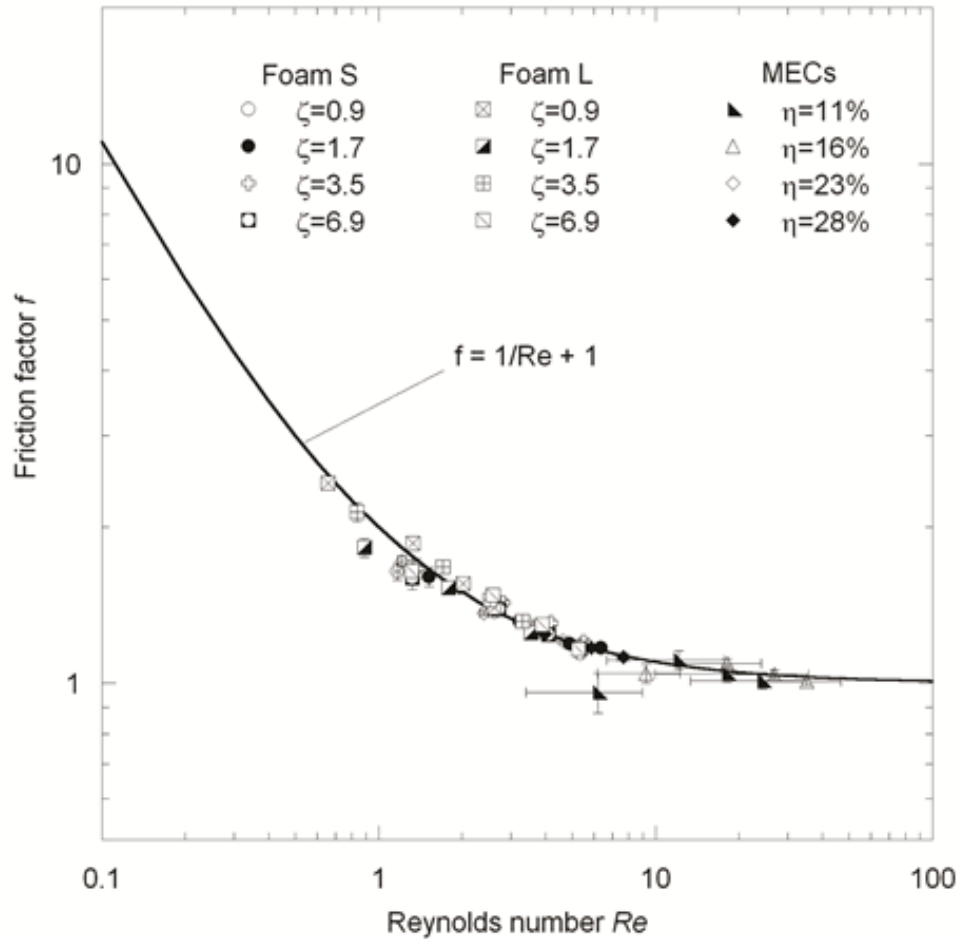


Figure 4.10. Friction factor versus Re for SMP foam samples and MECs. The friction factors and Reynolds numbers for both SMP foams and MECs collapse onto the relationship specified by Eq. 4.3 for Reynolds numbers ranging from approximately 1 to 35. The friction factors of all SMP foam samples are higher than those of the MECs.

Discussion

The goal of the state-of-the-art treatment of aneurysms is to prevent the flow of blood into the aneurysm by filling it with embolic coils. Because of biochemical reactions and altered hemodynamics, thrombosis is initiated within the coiled aneurysm, and over time, scar forms [5, 18, 27]. The biochemical and hemodynamic factors that influence thrombosis go hand in hand. For example, high flow shear stresses activate platelets that subsequently secrete

procoagulants and aggregate. Similarly, areas of turbulence and flow stagnation characterized by low shear and long retention times also activate and aggregate platelets [108]. Flow stagnation is one of the most important hemodynamic factors that promote thrombus formation within an aneurysm [18]. The current study demonstrates that SMP foams impose a greater resistance to flow compared to MECs and would therefore be more effective at producing these desired post-treatment hemodynamics. We do not observe hysteresis in the pressure gradient versus flow speed data, an effect which would be indicative of sample deformation during the test. Therefore, the higher friction factors for the SMP foams arise from a larger contact surface area and projected area that produce greater viscous and inertial losses, respectively, relative to those of MECs.

The porous media theory described in this study has been previously used to measure the geometrical parameters of polyurethane foams and fibrous porous media [109-113]. Additionally, blood flow through aneurysms treated with either embolic coils [95-98] or SMP foams [99] has been simulated utilizing porous media models. Major differences between these various studies are the selection of the porous media model, the definition of the Re , the flow regime of the experiments, and the fluid type. Some authors limit their flow range to the Darcy regime and define Re based on the cell size [110, 114], while others use different porous media models, such as the Kozeny theory [95, 98]. The greatest challenge of this type of model is that it requires the characterization of additional constitutive parameters, such as the specific surface and, in some cases, the flow tortuosity [112]. Another drawback specific to the Kozeny theory is that it does not take into account the diverging or converging nature of the flow within the porous medium. This is one possible

reason for the differences between the embolic coil permeability values of Kakalis et al. and those measured for MECs [95, 107].

One of the main limitations in this study is the selection of the Newtonian working fluid, which does not exhibit the shear thinning behavior of blood at small shear rates. Even though it is well documented in the literature that permeability and form factor are intrinsic geometrical parameters of the porous medium, experiments should be performed in order to validate this statement for the use of blood [100, 102, 107]. Nonetheless, Sorteberg et al. observed marked similarities in pressure and fluid dynamics within a bench-top aneurysm model packed with coils using blood versus saline solution as the working fluid [115]. In addition, Ortega et al. found nearly identical permeability and form factor values for both Newtonian and non-Newtonian viscosity models when simulating the flow of blood through virtually-reticulated SMP foam at Re ranging between 0.2 and 2.7 [99]. Thus, within this range of Re , the permeability and form factor values from the present study may be applicable for non-Newtonian blood flow within foam- or coiled-filled aneurysms.

Conclusion

We have reported *in vitro* experimental measurements on the porous media properties of mechanically-reticulated SMP foams and MECs. For the reticulation and coil packing densities evaluated in this study, SMP foams impose a larger flow resistance than MECs. From a perspective in which only the fluid dynamics are considered, these results suggest

that SMP foams will be more effective than embolic coils at inducing flow stagnation within a treated aneurysm.

CHAPTER V

CONCLUSIONS AND FUTURE WORK

Over the last century, parallel advancements primarily in the fields of medical imaging and materials science, have spurred the progress of neuroendovascular medical devices. Its capabilities have been further broadened by the emergence of smart materials, such as nitinol and SMPs, which provide the shape changes necessary for catheter delivery. This dissertation focused on the design, fabrication and testing of neuroendovascular devices made with shape memory materials for the treatment of stroke.

Fifteen million people suffer stroke each year worldwide, out of which five million are permanently disabled, rendering this disease the leading cause of adult long term disability. Commercial neuroendovascular devices for the treatment and prevention of stroke are available; however, their use is associated with severe complications that often lead to treatment failure and in some cases, patient death. The motivation for the work presented in this dissertation was to provide alternative solutions through the use of novel shape memory materials.

Commercially available thrombectomy devices are mainly limited by their deployment length as well as their potential for thrombus dislodgement during treatment. Chapter I presented the first attempt at creating a device with a shorter deployment length and a greater surface area of contact for improved thrombus hold. A flower-shape design that crimps to a cylinder was adopted, and prototypes were fabricated from crosslinked acrylic thermoset. Different crosslink densities, 5, 15, 25 and 35 mole % crosslinker, were evaluated with the

goal of maximizing the recovery stress of the devices to ensure thrombus hold. We performed constrained recovery experiments on the machined devices to quantify the increase in recovery stress as a function of crosslinker amount, and there was a change of one order of magnitude between the 5 and 15 mole % crosslinker devices. Although the devices with the two highest crosslink densities resulted in even higher recovery stresses, they devices broke during the constrained recovery experiment as a result of material limitations. While increasing crosslink density results in increases in recovery stress, it also reduces the strain capacity of the material. Limited strain and machining defects were probably the reason why the highest crosslinked devices failed. The devices with the two lowest crosslink densities were tested in a bench-top thrombotic model with flow, and the effectiveness of increasing the crosslink density from 5 to 15 mole % crosslinker was demonstrated by a success rate increase from 0 to 67%, respectively.

During the bench-top thrombus removal experiments it was observed that this device had the potential of being off-centered with respect to the vessel lumen after shape recovery, resulting in device-vessel gaps, through which the thrombus could escape. The need for a design re-evaluation became glaring, giving rise to a novel concept of the thrombectomy device involving SMP foam and nitinol, which was discussed in Chapter II. This version of the thrombectomy device is referred to as SMP-SMA, or hybrid thrombectomy device, because it exploits the benefits of both types of materials: the high volume expansion rate of SMP foams, and the high modulus of nitinol. After arriving at a design that was most feasible from a device performance and fabrication perspectives (see Appendix A for previously attempted iterations), design requirements were delineated based on the user

needs and predicate device data. Appropriate tests were then carried out to verify that the design met the set specifications. The fabricated device was only 12 mm in length, compared to 20-30 mm for commercially available stent retrievers. Additionally, the results of all verification tests were within the accepted range and the device showed a 100% success rate in 9 bench-top thrombus removal experiments with flow. Final proof-of-concept validation was possible through an acute porcine model, in which the device was able to re-establish blood flow in an artery occluded with a thrombus nearly 3 times its length.

The chemistry of the SMP foam that was utilized in the hybrid thrombectomy device was initially designed for embolic applications. The current state-of-the-art treatment of ISAs is the insertion of embolic coils with the primary goal of forming a thrombus that then leads to the isolation of the aneurysm from the vasculature thus reducing the likelihood of rupturing. However, with this treatment method it is difficult to achieve complete aneurysm filling, and over time, coils tend to compact resulting in the need of treatment repeats and in some cases, aneurysm rupture, after which there is only a 50% chance for survival. One of the main driving factors of the formation of a thrombus in a coiled aneurysm is hemodynamics, in particular longer residence time or flow stagnation. Therefore, in Chapter IV we took a porous media approach to study how the geometry of the SMP foams affected thrombosis within a treated aneurysm compared to non-clinical, inexpensive copper coils mimicking the geometry of embolic coils. The parameters that were investigated were permeability and form factor, which are correlation coefficients related to the viscous and inertial losses, respectively. Our results showed that the permeability of the SMP foams was one order of magnitude lower than that of the MECs, and their form factors were up to two orders of

magnitude higher. From this data it was concluded that the geometry of the SMP foams provides a better environment for fluid stagnation compared to the geometry of the MECs, suggesting that SMP foams would enhance thrombosis within a treated aneurysm compared to embolic coils.

This study was limited by the use of water as the working fluid. Even though permeability and form factor are theoretically independent of fluid properties, further experiments must be performed in order to validate these results with the use of blood. Given that it is difficult to implement a bench-top flow system with blood as the working fluid without having confounding effects of thrombosis within the pressure ports, a possible way to validate these results would be to subject the SMP foam samples and MECs to gravity-fed blood flow. By keeping the level of blood in the reservoir at a constant height, repeatability of the experimental conditions can be ensured between each sample. After a certain amount of time, samples can then be further investigated by means of SEM and weight measurements to compare the amount of thrombosis in both types of porous media.

REFERENCES

1. A. D. Lopez, C. D. Mathers, M. Ezzati, D. T. Jamison, C. J. L. Murray, *Lancet* **2006**, 367, 1747-1757.
2. L. G. Stead, R. M. Gilmore, M. F. Bellolio, A. A. Rabinstein, W. W. Decker, *Arch. Neurol.* **2008**, 65, 1024-1030.
3. C. D. Gandhi, L. D. Christiano, C. J. Prestigiacomo, *Neurosurg. Focus* **2009**, 26, 1-8.
4. C.J. Prestigiacomo, *Neurosurgery* **2006**, 59, S3-39.
5. E. Deshaies, C. Eddleman, A. Boulos, *Handbook of Neuroendovascular Surgery*, Thieme, New York **2012**.
6. D. Lloyd-Jones, R. Adams, M. Carnethon, G. De Simone, T. B. Ferguson, K. Flegal, E. Ford, K. Furie, A. Go, K. Greenlund, *Circulation* **2009**, 119, 480-486.
7. W. S. Smith, G. Sung, S. Starkman, J. L. Saver, C. S. Kidwell, Y. P. Gobin, H. L. Lutsep, G. M. Nesbit, T. Grobelny, M. M. Rymer, *Stroke* **2005**, 36, 1432-1438.
8. P.J. Lindsberg, A.J. Grau, *Stroke* **2003**, 34, 2518-2532.
9. G.W. Petty, R.D. Brown, J.P. Whisnant, J.D. Sicks, W.M. O'Fallon, D. O Wiebers, *Stroke* **1999**, 30, 2513-2516.
10. J. Moncayo, G. Devuyst, G. Van-Melle, J. Bogousslavsky, *Arch. Neurol.* **2000**, 57, 1139-1144.
11. J.F. Varona, J.M. Guerra, F. Bermejo, J.A. Molina, A. Gomez de la Cámara, *Eur. Neurol.* **2007**, 57, 212-218.
12. M. Brainin, Y. Teuschl, L. Kalra, *Lancet* **2007**, 6, 553-561.
13. J.L. Saver, *Stroke* **2006**, 37, 263-266.
14. D. L. Brown, W. G. Barsan, L. D. Lisabeth, M. E. Gallery, L. B. Morgenstern, *Ann. Emerg. Med.* **2005**, 46, 56-60.
15. V. Torres, Y. Pirson, D. Wiebers, *N. Engl. J. Med.* **2006**, 355, 2703-2704.
16. C. Vega, J.V. Kwoon, S.D. Lavine, *Am. Fam. Physician*, **2002**, 66, 601-610.
17. F.J. Carod-Artal, J.A. Egido, *Cerebrovasc. Dis.* **2009**, 27, 204-214.

18. J.D. Humphrey, *Cardiovascular Solid Mechanics: Cells, Tissues, and Organs*, Springer, New York **2002**.
19. J.D. Humphrey, S.L. Delange, *An Introduction to Biomechanics: Solids and Fluids, Analysis and Design*, Springer, New York **2004**.
20. R.S. Mitchell, V. Kumar, A.K. Abbas, N. Fausto, *Robbins basic pathology*, Saunders, Elsevier, Philadelphia **2007**.
21. J.R. Østergaard, *Acta Neurol. Scand.* **1989**, 80, 81-98.
22. T. Kurth, S.C. Moore, J.M. Gaziano, C.S. Kase, M.J. Stampfer, K. Berger, J.E. Buring, *Arch. Intern. Med.* **2006**, 166, 1403-1409.
23. W.I. Schievink, *New Engl. J. Med.* **1997**, 336, 28-40.
24. J.M. Neff, *J. Am. Med. Assoc.* **1911**, 57, 700-708.
25. G. Debrun, P. Lancour, J.P. Caron, M. Hurth, J. Comoy, Y. Keravel, *Neuroradiology* **1975**, 9, 267-271.
26. W.E. Dandy, *Ann. Surg.* **1938**, 107, 654-659.
27. B. Richling, *Neurosurgery* **2006**, 59, S3-30.
28. A.J. Luessenhop, W.T. Spence, *J. Am. Med. Assoc.* **1960**, 172, 1153-1155.
29. J.L. Doppman, G. Di Chiro, A. Ommaya, *Lancet* **1968**, 291, 477.
30. J.P. Gallagher, *J. Am. Med. Assoc.* **1963**, 183, 231-236.
31. H. Rosomoff, *Trans. Am. Neurol. Assoc.* **1966**, 91, 330-331.
32. J. F. Alksne, A.G. Fingerhut, R.W. Rand, *J. Neurol. Neurosur. Ps.* **1967**, 30, 159-162.
33. S.B. Yodh, N.T. Pierce, R.J. Weggel, B. Montgomery, *Med. Biol. Engng.* **1968**, 6, 143-147.
34. S.C. Werner, A.H. Blakemore, B.G. King, *J. Am. Med. Assoc.* **1941**, 116, 578-582.
35. S. Mullan, C. Reyes, J. Dawley, *Prog. Neurol. Surg.* **1969**, 3, 193-211.
36. N. Chater, N. Peters, *West. J. Med.* **1976**, 124, 1-5.
37. R. Spetzler, P. Schmiedek, O. Gratzl, *Stroke* **1977**, 8, 16-19.

38. A. de Sousa Pereira, *Ann. Surg.* **1955**, 141, 218-233.
39. E. Moniz, *Lancet* **1933**, 222, 1144-1147.
40. C. Kerber, *Neurosurgery* **2006**, 59, S3-22.
41. D. Collen, H. Lijnen, *Arterioscler. Throm. Vas.* **2009**, 29, 1151-1155.
42. Y.P. Gobin, S. Starkman, G.R. Duckwiler, T. Grobelny, C.S. Kidwell, R. Jahan, J. Pile-Spellman, A. Segal, F. Vinuela, J.L. Saver, *Stroke* **2004**, 35, 2848-2854.
43. S. Hilal, *Am. J. Neuroradiol.* **1988**, 9, 1030.
44. K. J. Becker, T.G. Brott, *Stroke* **2005**, 36, 400-403.
45. E. Wajnberg, J. Marcondes de Souza, E. Marchiori, E.L. Gasparetto, *Surg. Neurol.* **2009**, 72, 612-619.
46. Y. Murayama, F. Vinuela, G.R. Duckwiler, Y.P. Gobin, G. Guglielmi, *J. Neurosurg.* **1999**, 90, 207-214.
47. R.A. Willinsky, *Can. Med. Assoc. J.* **1999**, 161, 1136.
48. A.F. Zubillaga, G. Guglielmi, F. Vi, G. Duckwiler, *Am. J. Neuroradiol.* **1994**, 15, 815-820.
49. F. Viñuela, G. Duckwiler, M. Mawad, *J. Neurosurg.* **1997**, 86, 475-482.
50. M. Sluzewski, W.J. van Rooij, M.J. Slob, J.O. Bescos, C.H. Slump, D. Wijnalda, *Radiology* **2004**, 231, 653-658.
51. K. Imai, T. Mori, H. Izumoto, M. Watanabe, *Am. J. Neuroradiol.* **2005**, 26, 1395-1398.
52. T.E. Mayer, G.F. Hamann, H.J. Brueckmann, *Stroke* **2002**, 33, 2232-2235.
53. G. Wikholm, *Am. J. Neuroradiol.* **2003**, 24, 892-894.
54. A. Lendlein, S. Kelch, *Angew. Chem. Int. Edit.* **2002**, 41, 2034-2057.
55. P. Singhal, J.N. Rodriguez, W. Small, S. Eagleston, J. Van de Water, D.J. Maitland, T.S. Wilson, *J. Polym. Sci. Pol. Phys.* **2012**, 50, 724-737.
56. K. Hearon, K. Gall, T. Ware, D.J. Maitland, J.P. Beringer, T.S. Wilson, *J. Appl. Polym. Sci.* **2011**, 121, 144-153.

57. K. Otsuka K, C.M. Wayman, *Shape Memory Materials*, Cambridge University Press, Cambridge, United Kingdom **1999**.
58. D.C. Lagoudas, *Shape Memory Alloys: Modeling and Engineering Applications*, Springer, New York **2008**.
59. L. Petrini, F. Migliavacca, *J. Metallur.* **2011**, 2011, 1-15.
60. P. Hiemenz, T. Lodge, *Polymer Chemistry*, 2nd ed., Taylor & Francis, Boca Raton, Florida **2007**.
61. W. Voit, T. Ware, R. R. Dasari, P. Smith, L. Danz, D. Simon, S. Barlow, S. R. Marder, K. Gall, *Adv. Funct. Mater.* **2010**, 20, 162-171.
62. J. Hartman, W. Small, T. S. Wilson, J. Brock, P. R. Buckley, W. J. Benett, J. M. Loge, D. J. Maitland, *Am. J. Neuroradiol.* **2007**, 28, 872-874.
63. P. R. Buckley, G. H. McKinley, T. S. Wilson, W. Small, W. J. Benett, J. P. Bearinger, M. W. McElfresh, D. J. Maitland, *IEEE Trans. Biomed. Eng.* **2006**, 53, 2075-2083.
64. A. M. Ortega, S. E. Kasprzak, C. M. Yakacki, J. Diani, A. R. Greenberg, K. Gall, *J. Appl. Polym. Sci.* **2008**, 110, 1559-1572.
65. L. E. Nielsen, *J. Macromol. Sci-Pol R.* **1969**, 3, 69-103.
66. K. Hearon, L. D. Nash, B. L. Volk, T. Ware, J. P. Lewicki, W. E. Voit, T. S. Wilson, D. J. Maitland, *Macromol.Chem.* **2012**, 214, 1258-1272.
67. K. Hearon, S. E. Smith, C. A. Maher, T. S. Wilson, D. J. Maitland, *Radiat. Phys. Chem.* **2012**, 83, 111-121.
68. T. G. Mezger, *The Rheology Handbook*, 2nd Ed., Vincentz Network GmbH & Co KG, Hannover, Germany **2006**.
69. D. L. Safranski, K. Gall, *Polymer* **2008**, 49, 4446-4455.
70. J. Gralla, G. Schroth, L. Remonda, A. Fleischmann, J. Fandino, J. Slotboom, C. Brekenfeld, *Am. J. Neuroradiol.* **2006**, 27, 1357-1361.
71. K. Stock, S. Wetzel, P. Lyrer, E. Radü, *Eur. Radiol.* **2000**, 10, 1795-1800.
72. D. A. Schiraldi, S. Iyer, *Vol: 1051: Advances in Silicones and Silicone-Modified Materials* (Eds: S.J. Clarson, S.D. Smith, M.E. Van Dyke), Am. Chem. Soc. Washington DC **2010**, 211-226.

73. C. M. Yakacki, R. Shandas, D. Safranski, A. M. Ortega, K. Sassaman, K. Gall, *Adv. Funct. Mater.* **2008**, *18*, 2428-24635.
74. G. Gamble, J. Zorn, G. Sanders, S. MacMahon, N. Sharpe, *Stroke* **1994**, *25*, 11-16.
75. W. A. Riley, R. W. Barnes, G. W. Evans, G. L. Burke, *Stroke* **1992**, *23*, 952-956.
76. T.K. Kim, J.K. Rhim, C.J. Lee, S.H. Oh, B.S. Chung, *J. Cerebrovasc. Endovasc. Neurosurg.* **2012**, *14*, 203-209.
77. M. Saleh, J.N Spence, S. Nayak, G. Pearce, C. Tennuci, C. Roffe, *Am. J. Cardiovasc. Dis.* **2012**, *2*, 301-308.
78. Solitaire FR Revascularization Device (Micro Therapeutics), *FDA 510(k) Summary No. K113455*, **2012**.
79. Trevo Retriever (Concentric Medical), *FDA 510(k) Summary No. K120961*, **2012**.
80. Merci Retriever (Concentric Medical), *FDA 510(k) Premarket Notification No. K033736*, **2004**.
81. W.L. Baker, J.A. Colby, V. Tongbram, R. Talati, I.E. Silverman, C.M. White, J. Kluger, C.I. Coleman, *Ann. Intern. Med.* **2011**, *154*, 243-252.
82. C. Tennuci, G. Pearce, J. Wong, S. Nayak, T. Jones, F. Lally, C. Roffe, *Stroke Res. Treat.* **2011**, *2011*, 1-6.
83. J.P. Broderick, *Stroke* **2009**, *40*, S103-S106.
84. J.N. Rodriguez, Y.J. Yu, M.W. Miller, T.S. Wilson, J. Hartman, F.J. Clubb, B. Gentry, D.J. Maitland, *Ann. Biomed. Eng.* **2012**, *40*, 883-897.
85. A.R. Pelton, J. Dicello, S. Miyazaki, *Minimal Invasiv. Ther.* **2000**, *9*, 107-118.
86. N. Ogata, K. Goto, K. Uda, *Interv. Neuroradiol.* **1997**, *3*, 65-80.
87. T. Wilson, J. Bearinger, J. Herberg, J. Marion, W. Wright, C. Evans, D. Maitland, *J. Appl. Polym. Sci.* **2007**, *106*, 540-551.
88. Y.J. Yu, K. Hearon, T.S. Wilson, D.J. Maitland, *Smart. Mater. Struct.* **2011**, *20*, 1-6.
89. B. Tam, M.I. Khan, Y. Zhou, *Metall. Mater. Trans. A* **2011**, *42A*, 2166-2175.
90. M.I. Khan, Y. Zhou, *Proceedings from the Materials & Processes for Medical Devices Conference*. Minneapolis, Minnesota. J. Gilbert **2009**, 210-213.

91. J.Y. Chueh, A.K. Wakhloo, G.H. Hendricks, C.F. Silva, J.P. Weaver, M.J. Gounis, *Am. J. Neuroradiol.* **2011**, 32, 1237-1244.
92. C. Castaño, L. Dorado, C. Guerrero, M. Millan, M. gomis, N. Perez de la Ossa, M. Castellanos, M.R. Garcia, S. Domenech, A. Davalos, *Stroke* **2010**, 41, 1836-1840.
93. W. Small IV, P. Singhal, T.S. Wilson, D.J. Maitland, *J. Mater. Chem.* **2010**, 20, 3356-3366.
94. W. Hwang, B.L. Volk, F. Akberali, P. Singhal, J.C. Criscione, D.J. Maitland, *Biomech. Model. Mechan.* **2012**, 11, 715-729.
95. N.M.P. Kakalis, A.P. Mitsos, J.V. Byrne, Y. Ventikos, *IEEE T. Med. Imaging* **2008**, 27, 814-824.
96. K.M. Khanafer, R. Berguer, *Using Porous Media Theory to Determine the Coil Volume Needed to Arrest Flow in Brain Aneurysms*. Porous Media: Applications in Biological Systems and Biotechnology, ed. K. Vafai, Taylor & Francis, Boca Raton, Florida **2010**, 237-250.
97. Y. Wei, S. Cotin, L. Fang, J. Allard, C. Pan, S. Ma, *Lect. Notes Comput. Sc.* **2009**, 12, 198-205.
98. A.P. Mitsos, N.M.P. Kakalis, Y.P. Ventikos, J.V. Byrne, *Neuroradiology* **2008**, 50, 341-347.
99. J.M. Ortega, J. Hartman, J.N. Rodriguez, D.J. Maitland, *Ann. Biomed. Eng.* **2013**, 41, 725-743.
100. J. Lage, *The Fundamental Theory of Flow Through Permeable Media from Darcy to Turbulence*. Transport Phenomena in Porous Media, ed. D.B. Ingham, I. Pop, Elsevier Science, Oxford **1998**, 1-30.
101. A. Dybbs, R. Edwards, *A New Look at Porous Media Fluid Mechanics-Darcy to Turbulent*. Fundamentals of Transport Phenomena in Porous Media, ed. J. Bear, M.Y. Corapciogly, Springer Netherlands, Dordrecht **1984**, 201-256.
102. A.E. Scheidegger, *The Physics of Flow Through Porous Media (3rd ed.)*, University of Toronto Press, Toronto **1974**.
103. P.R. Bevington, D.K. Robinson, *Data Reduction and Error Analysis for the Physical Sciences (2d ed.)*, McGraw-Hill, New York **1992**.
104. R.S. Figliola, D.E. Beasley, *Theory and Design for Mechanical Measurements (4th ed.)*, Wiley, New York **2006**.

105. J. Geertsma, *Spe. J.* **1974**, 14, 445-450.
106. N. Ahmed, D.K. *J. Hyrd. Eng. Div.-ASCE* **1969**, 95, 1847-1857.
107. J. Bear, *Dynamics of Fluids in Porous Media*, New York, Dover, **1988**.
108. S. Einav, D. Bluestein, *Ann. NY Acad. Sci.* **2004**, 1015, 351-366.
109. M.V. Sefton, H.M. Lusher, *J. Appl. Polym. Sci.* **1980**, 25, 2167-2178.
110. J.F. Despois, A. Mortensen, *Acta Mater.* **2005**, 53, 1381-1388.
111. G.S. Beavers, E.M. Sparrow, *J. Appl. Mech.* **1969**, 36, 711-715.
112. N. Sabiri, A. Montillet, J. Comiti, *Chem. Eng. Commun.* **1997**, 156, 59-74.
113. L. Tadrist, M. Miscevic, O. Rahli, F. Topin, *Exp. Therm. Fluid Sci.* **2004**, 28, 193-199.
114. M. Dawson, J. Germaine, L. Gibson, *Int. J. Solids Struct.* **2007**, 44, 5133-5145.
115. A. Sorteberg, W. Sorteberg, B.D.L. Aagaard, A. Rappe, C.M. Strother, *Am. J. Neuroradiol.* **2004**, 25, 1049-1057.

APPENDIX A

NITINOL COMPONENT DESIGN ITERATIONS: FROM MECHANICAL NITINOL FLOWER (MNF) TO SNF

The first prototyping attempt of the SMP-SMA hybrid thrombectomy device concept consisted of feeding four nitinol wires (0.1 mm diameter) through a stainless steel microband and soldering them at the distal tip of a center wire (0.25 mm diameter) as pictured in Figure A1. This version of the nitinol component was termed mechanical nitinol flower (MNF) because the actuation to the flower shape was achieved by pulling the center wire, relying on the nitinol's pseudoelastic behavior to recover its original shape upon unloading. While this method was an attractive solution to the lack of equipment with nitinol machining capabilities such as an excimer laser, it had three major flaws: size, actuation load and aesthetics. The smallest catheter size through which this device could be delivered was 6 F, thus miniaturization was not possible. Also, the load required for the mechanical actuation of the nitinol flower was higher than the load required to compress the foam axially (see Figure A2). Given the scale of the components, the fabrication of this prototype in a manner that was pleasing to the eye was difficult to achieve.

In an attempt of reducing the load required for the actuation of the MNF, the wires were subjected to heat treatments. It has been shown that when nitinol is exposed to heat for prolonged periods of time, a precipitation reaction occurs that increases its austenitic finish transformation temperature. This shift also causes a decrease in the upper loading plateau, defined as the tensile stress at 3% strain according to the standard test method for "Tension testing of nickel-titanium superelastic materials" (ASTM F2516-07E2). The upper loading

plateau is also the stress required to induce crystal transformation from austenite to martensite. Therefore, the reduction in the upper loading plateau after heat treatment yields wire that is more compliant at room temperature [85].



Figure A1. First prototype of the SMP-SMA thrombectomy device made assembled with the nitinol wire-based MNF and crimped SMP foam.

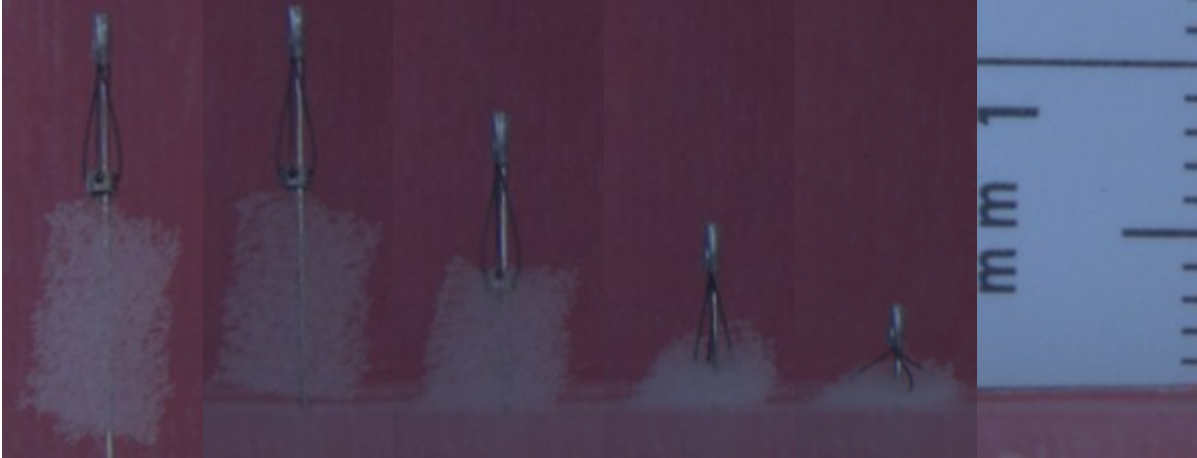


Figure A2. Axial compression of MNF and SMP foam in 37 °C water.

Figure A3 shows the stress-strain curves of two nitinol wires (0.1 mm diameter) that were tested following ASTM F2516-07E2, one untreated and the other one after it had been treated at 550 °C for 180 minutes. This heat treatment resulted in a reduction in the upper loading plateau from 575.5 to 169.9 MPa along with a significant decrease in shape memory. Upon unloading at 6% strain, the control was able to recover 6% strain, while the heat treated wire only recovered 1% strain. This loss in shape memory was also observed in devices made with heat treated wire at 550 °C for 60 and 120 minutes as pictured in Figure A4 before and after axial compression. Only the wires in the control device fully recovered their shape.

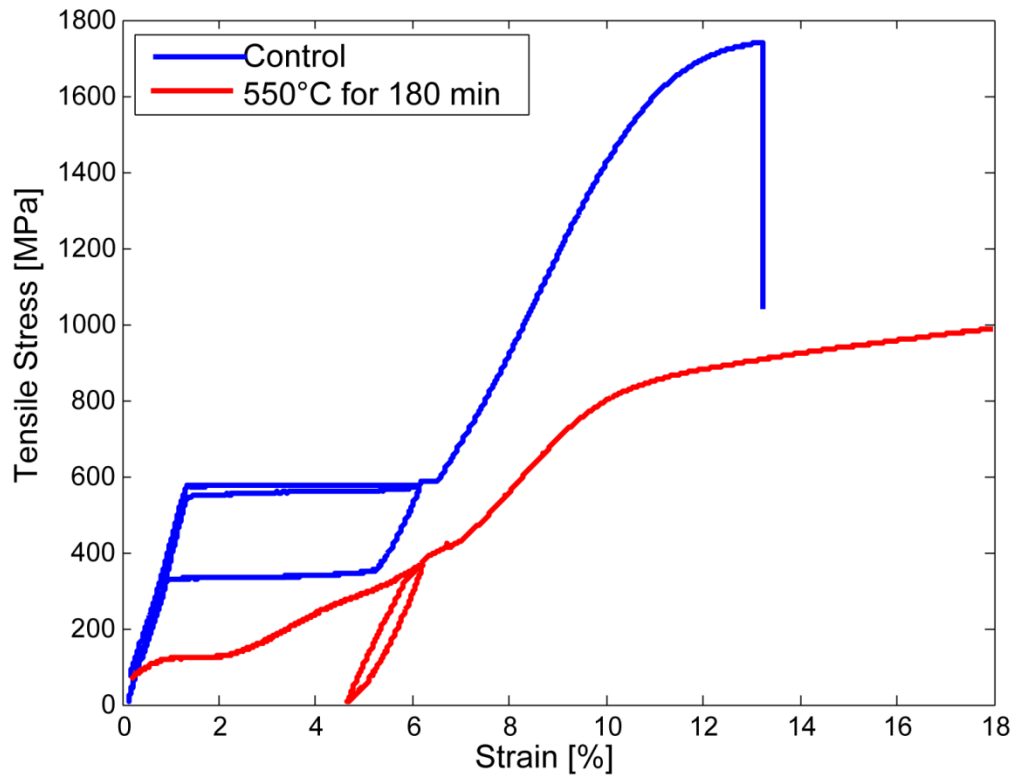
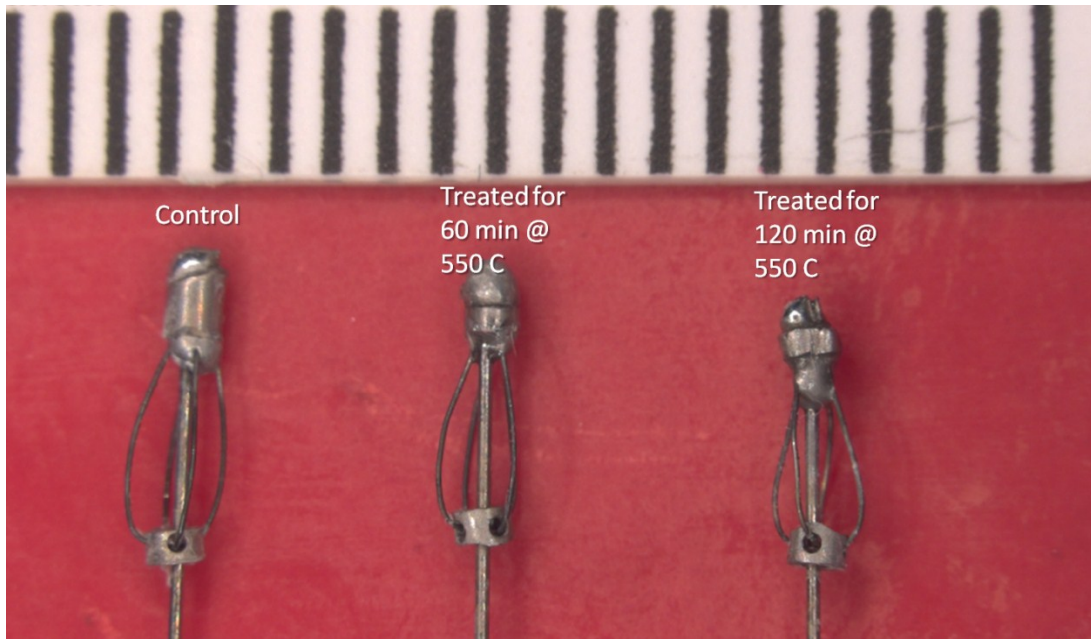


Figure A3. Tensile properties of untreated nitinol wire (0.1 mm diameter) as well as treated wire at 550 °C for 180 min.

(a)



(b)



Figure A4. MNFs assembled with control wire and heat treated wire at 550 °C for 60 and 120 min before (a) and after (b) axial compression.

It is evident that no further improvements could be made on the first prototyping method of the MNF. Therefore, we resorted to a method that utilized equipment with nitinol machining capabilities. The resulting prototype is shown in Figure A5. Four 3 mm long slits were machined with an excimer laser every 90° on nitinol tube (0.41 mm outer diameter, 0.33 mm inner diameter). This version was still termed MNF because the actuation method was intended to be mechanical as well. However, with this iteration, miniaturization was possible, but the load required for actuation of the machined MNF was still higher than the load required to axially compress the AMP foam. Figure A6 shows that a peak load of 1.9 N is required to achieve maximum reversible deformation of the excimer machined MNF. This load is roughly one order of magnitude higher than the load required to axially compress SMP foam to 80% (see Figure A7).

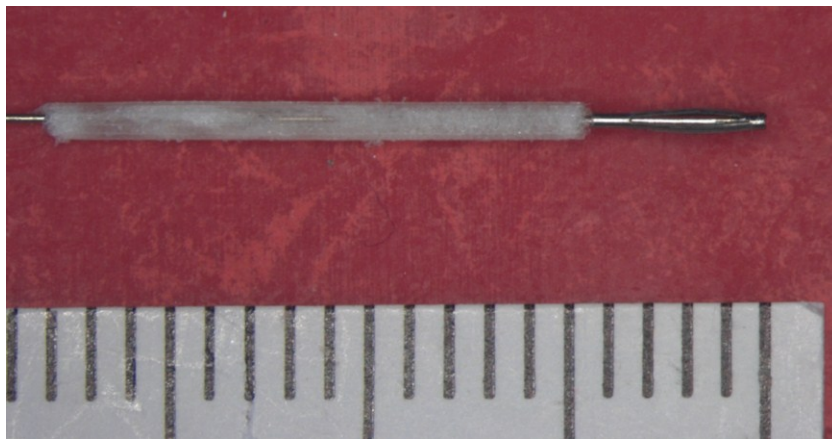


Figure A5. Un-actuated laser-cut MNF with crimped SMP foam.

Thus, there was a risk of SMP foam slippage during thrombectomy because the SMP foam would be fully compressed while the MNF would still be in its unactuated geometry. Therefore, with this design iteration, the MNF did not serve its purpose: to retain the foam during compression. It is for this reason that the third and final iteration was the pre-setting of the nitinol flower shape thermally.

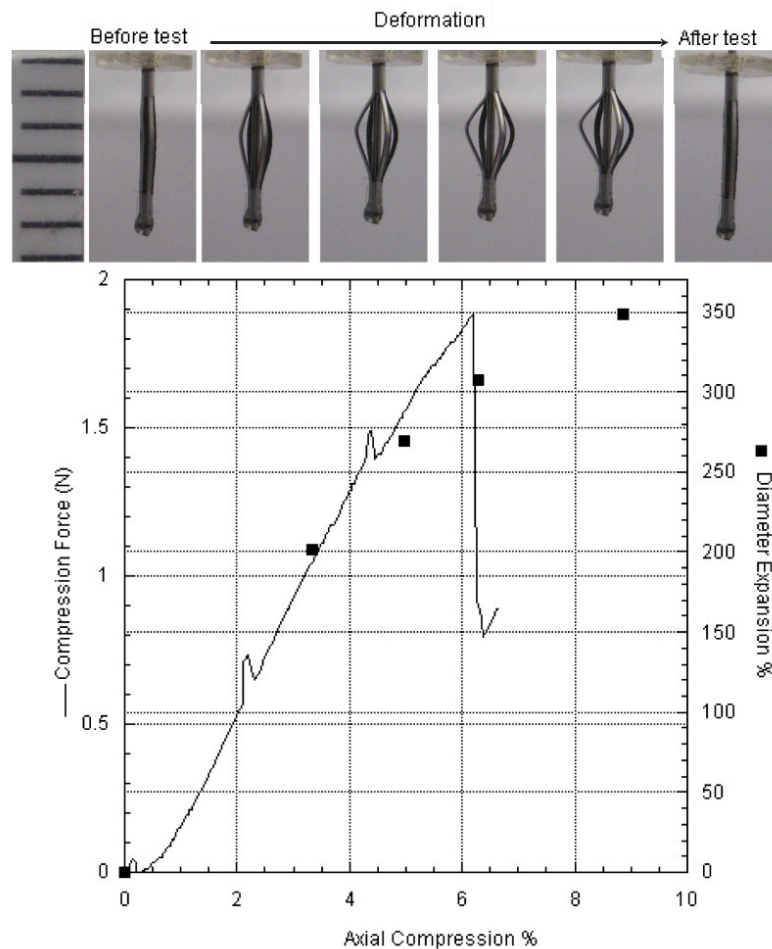


Figure A6. Force required for axial compression of the laser-cut MNF and resulting diameter diameter expansion.

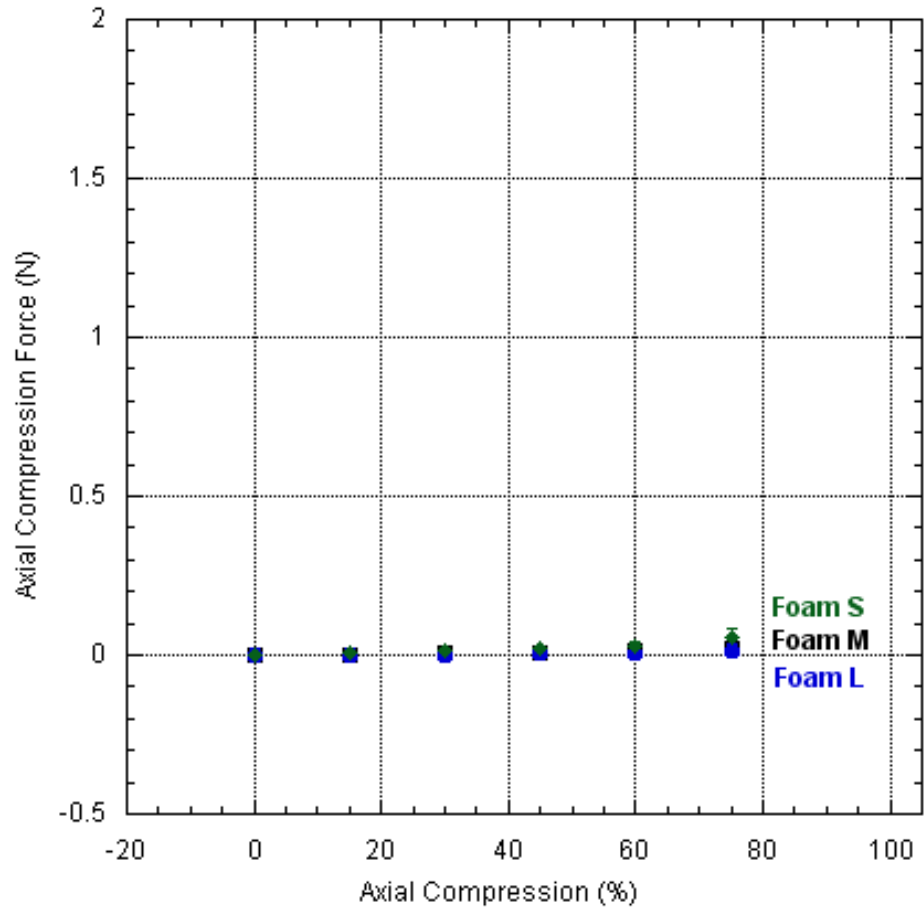


Figure A7. Force required for axial compression of SMP foams S, M and L.

APPENDIX B

POROUS MEDIA CHARACTERIZATION SYSTEM MANUAL

Introduction

This manual contains details about the components; both purchased as well as machined in-house, and operation instructions for the Porous Media Characterization System in the Biomedical Device Laboratory. This system is intended to measure the pressure gradient across a porous sample as a function of fluid flow. By fitting the data of pressure gradient versus fluid velocity to a second order function by means of a least squares fit, the parameters of the Forchheimer-Hazen-Dupuit-Darcy (FHDD) (Eq. 1) can be calculated.

$$-\frac{\partial P}{\partial x} = \frac{\mu}{K} v_0 + \rho C v_0^2. \quad (\text{B1})$$

These parameters are permeability (K) and form factor (C), and provide information about the energy losses resulting from viscous and inertial effects respectively. The same system can be utilized to fit the data to a different porous media model; however, appropriate changes to the selection of the flow rate range and Matlab code must be made.

Components

The actual experimental setup is pictured in Figure B1. The flow loop is comprised of a gear pump (Chemsteel R106, Oberdorfer), a servo motor (750 W M-series, Applied Motion Products) (see Figure B2), a motor controller (BLuAC5-Q, Applied Motion Products) (see

Figure B3), a testing chamber, a fluid reservoir elevated by 30 cm above the testing chamber, a data acquisition (DAQ), and two high accuracy pressure transducers (PX429-2.5G5V, Omegadyne Inc with accuracy rated at $\pm 0.08\%$ of the baseline maximum) powered by a voltage source at 24 V (see Figure B4). The transducers have a flush system connected to them as pictured in Figure B5.

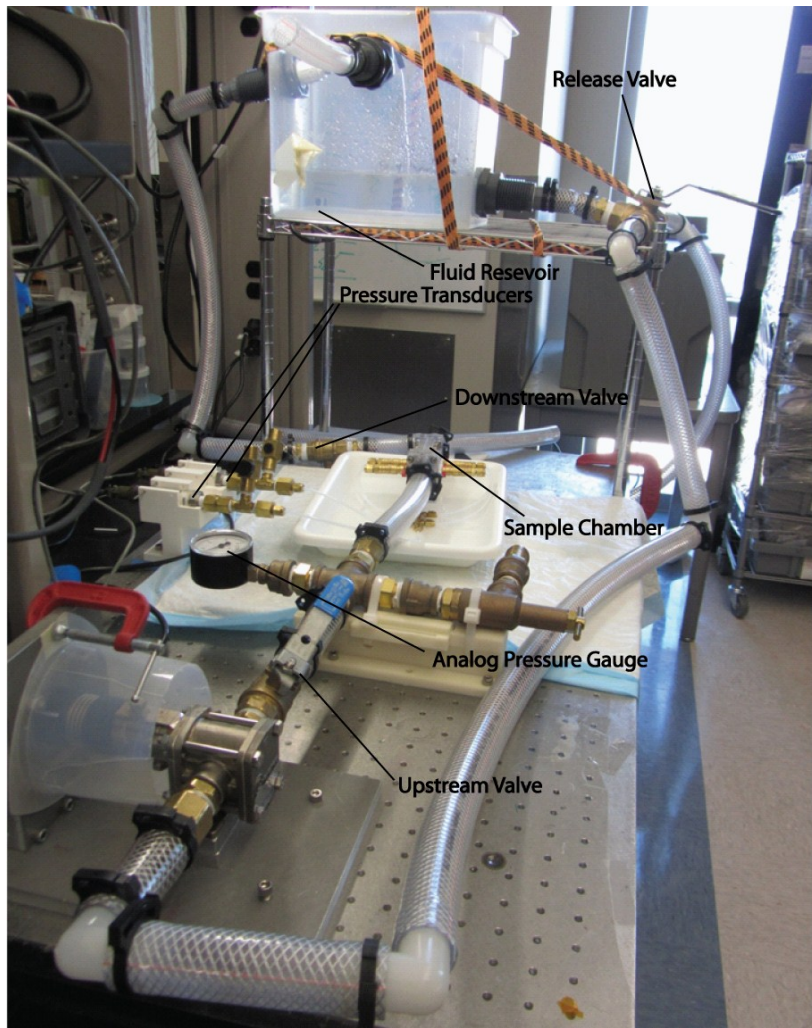


Figure B1. Actual experimental setup.

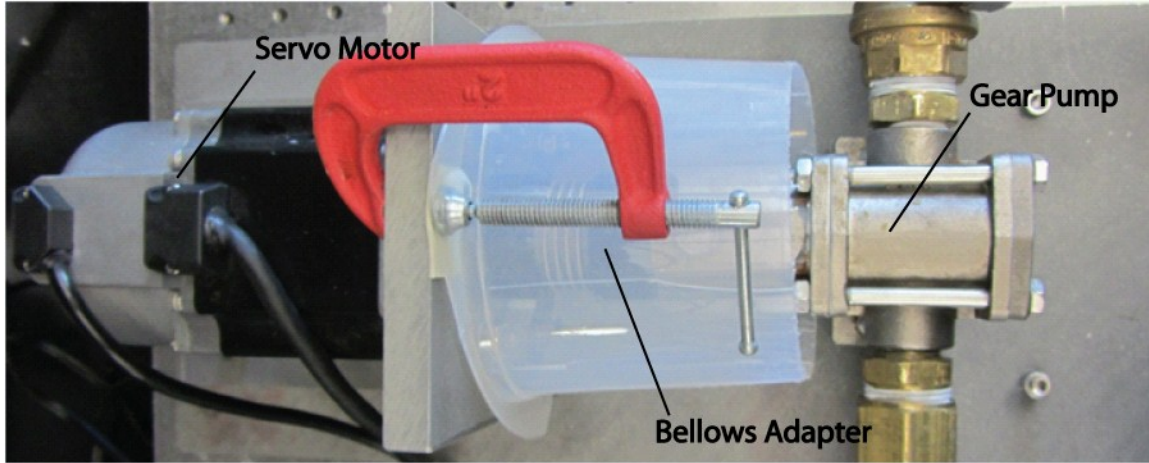


Figure B2. Servo motor and gear pump assembly.

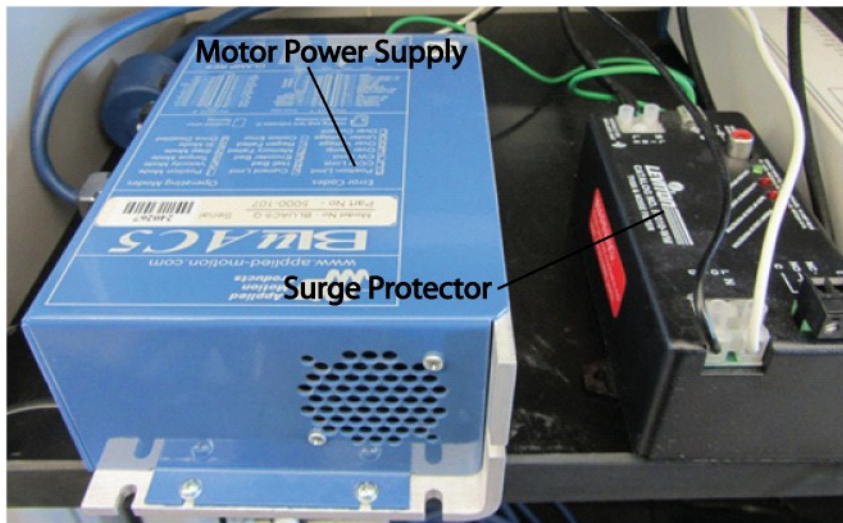


Figure B3. Motor controller and surge protector.

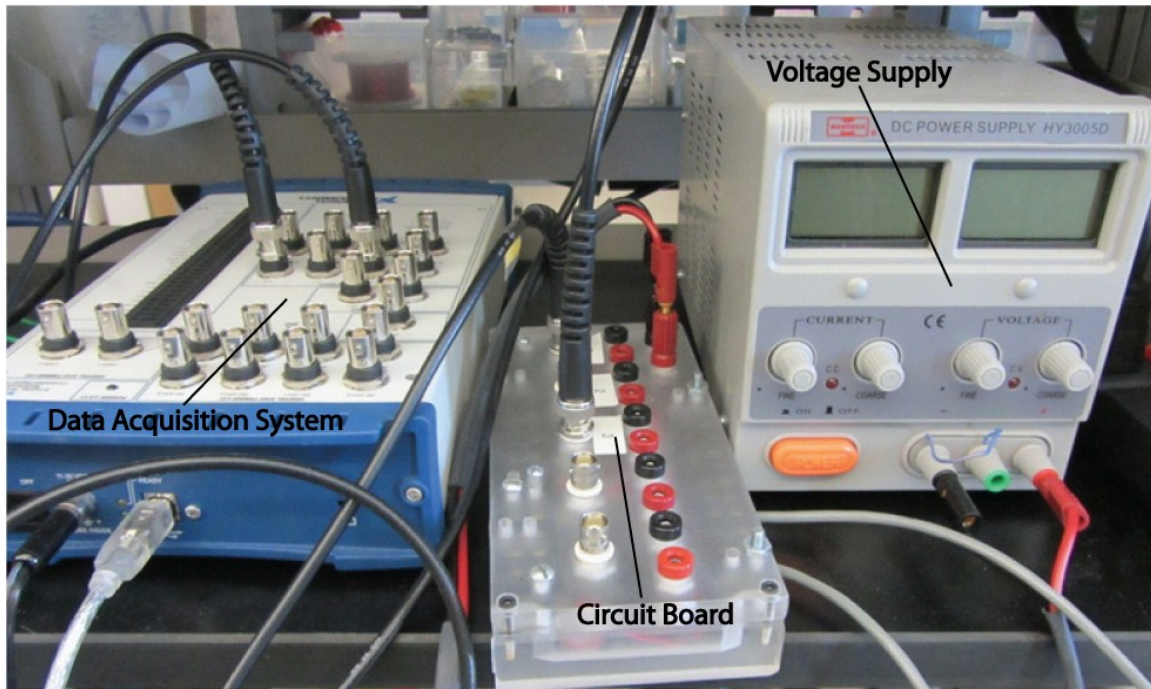


Figure B4. Transducer voltage supply and data acquisition electronics.

The two chambers described in Chapter 4 are available for this system. A component of the foam chamber is the 3D gasket, which is made with two Vitron o-rings (dash # 216), two pieces 6.2 mm long of o-ring cord, a 2 mm biopsy punch and clear urethane glue. Two holes are punched on both gaskets at 3 and 9 o'clock, and the o-ring cord is first immersed in the urethane glue and then inserted inside one of the holes until the end of the o-ring cord is flush with the punched o-ring. The opposite end of the o-ring cord is then adhered in the same manner to the second o-ring. The same procedure is done for the second o-ring cord. The final product should look like the gaskets pictured in Figure B6. Allow the urethane glue to cure for two hours. Replace the gasket if leaks are observed.

An engineering drawing of the sample holder is shown in Figure B7. Four o-rings (dash # 016) are required for each sample measurement. The part number and vendor of this item, as well as other consumables and parts that area likely to be replaced, are listed in Table B1.

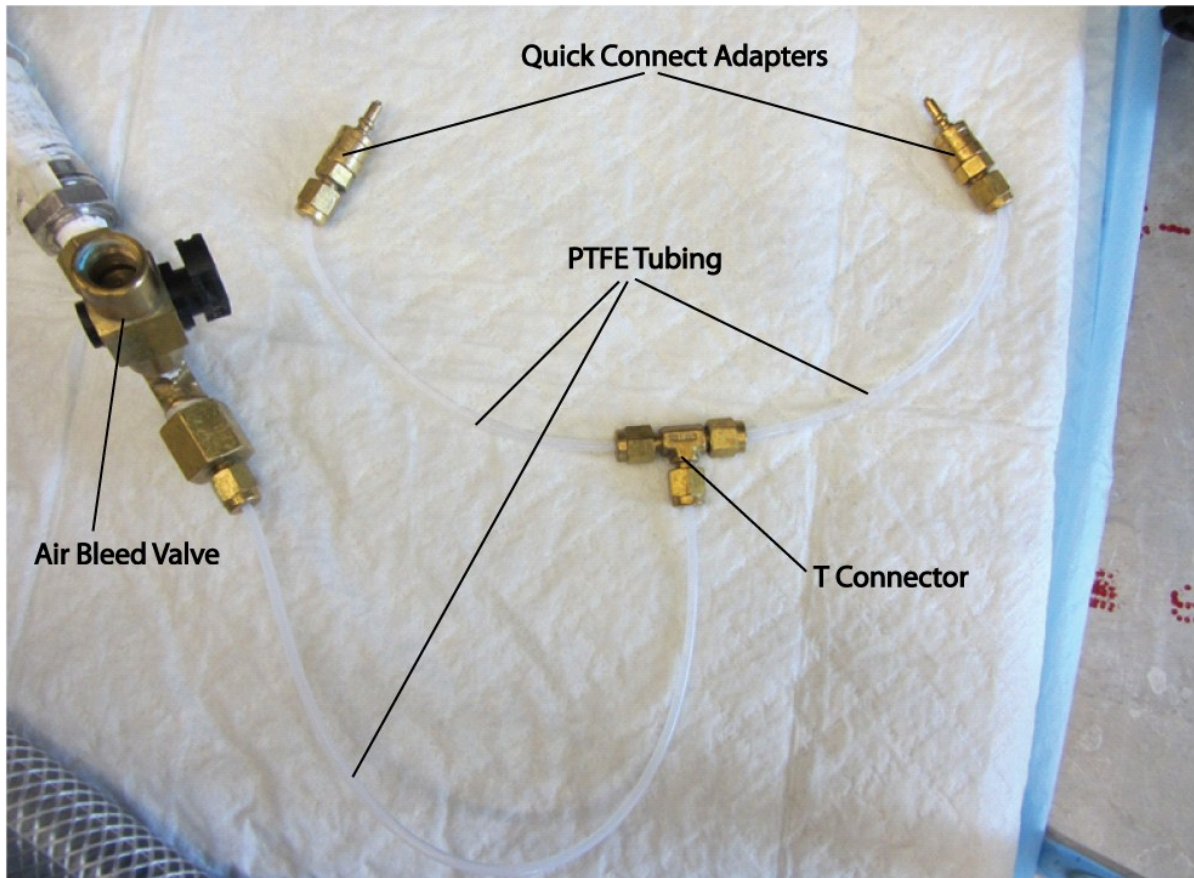


Figure B5. Transducer air flush system.



Figure B6. Custom 3D gaskets.

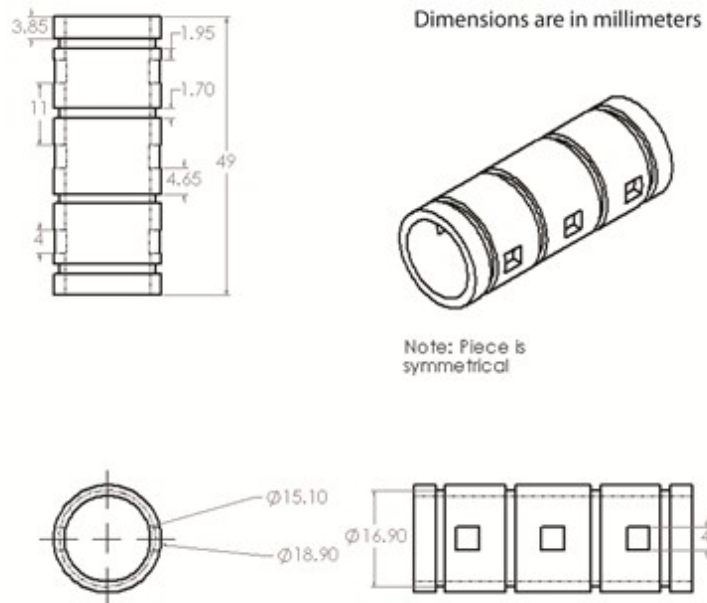


Figure B7. Drawing of sample holder.

Table B1. List of parts, part numbers and vendors.

Component of:	Part description	Part number	Vendor
Chambers and transducer flush system	Brass miniature quick connect fitting	B-QM2-D-200	Swagelok
Coil chamber	Coarse mesh	9238T56	McMaster
Coil chamber	Fine mesh	9230T454	McMaster
Coil chamber	Air bleed valve	4886K52	McMaster
Transducer flush system	1/16" ID PTFE tube	0000089761	Zeus
3D gasket	216 o-ring	9464K37	McMaster
3D gasket	2 mm diameter o-ring cord	9679K12	McMaster
Sample holder	016 o-ring	2418T122	McMaster

Operation instructions

The approach to set up the computer interface, load the sample into the measuring chamber, select the range of flow rates for the experiment, acquire data, and the basics about data interpretation are listed in the following subsections. Special care must be taken when measuring an unknown sample for the first time, because it might be too impervious for the transducers that are currently on the setup. If this were the case, new transducers able to appropriately resolve the pressure generated by the sample would be required. **Important: always check that all the hose clamps are tight prior to enabling flow.**

1. Setting up the computer interface
 - a. Turn on all equipment, including pump power source, DAQ system, and power supply (set voltage to 24 V)

- b. Begin by setting up the folder where the data is to be stored. Name the folder the run number from start to finish (for example, for runs 1-5, the folder name would be 'runs1-5')
- c. Copy into this folder the run matrix and Matlab program file
- d. Rename the run matrix to include the data taker's initials and the date in the following format: 'runmatrix_initials_DayMonthYear' (for John Smith on January 1st 2000, the file name would be 'runmatrix_JS_1January2000')
- e. Rename the Matlab program to include the name of the current runs being performed
- f. Open the run matrix, Matlab program, Labview program, Q Programmer, and a new windows explorer window
- g. In the run matrix, fill in all possible starting information including the date, the run numbers, working fluid, foam sample name, foam sample length, and foam sample diameter
- h. In the Matlab program, change the run matrix file name in row 38 to the same name as the edited run matrix. Set variables a and b on rows 22 and 23 to equal your first run number (for runs 1434-1435, a and b would be set to 1434 for the first run. Then, b will be changed to 1432, 1433, 1434, and 1435 for runs 1432, 1433, 1434, and 1435 respectively). Comment out (ctrl+t) rows 41-44 as seen in Figure B8.


```

21 %set range of file names:
22 - a=1434;
23 - b=1434;
24
25 %This is the diameter of the black plastic insert piece that goes inside
26 %the chamber. Be sure to change this value if the diameter is altered t o
27 %get a tighter foam fit. The units are m.
28 %Alternatively, if using the GDC chamber, this is the inner diameter of the
29 %chamber, which is 0.006 m.
30 - insert_diameter=0.0151;
31
32 %dx is the length from the first to the last pressure tap. This value
33 %should be used depending on the chamber used. The new permeability
34 %chamber is dx=0.03 m and the gdc chamber is dx=0.05 m.
35 - dx=0.015; %m
36
37 %Enter filename of the run matrix
38 - str2='run_matrix_JS_27Mar2013.xlsx';
39
40 %% Using hand measured flow rates instead of the transducer:
41 - data2=xlsread(str2,'sheet2');
42 - handmeas=data2(1:9,2); %*edit to the correct rows/columns of the hand
43 - range_vec=[1:9];
44 - rps_vals=data2(1:9,3);
45 %*****
46

```

Figure B8. Matlab code and rows (#41-44) that are to be commented out for all runs except the last one.

- i. In the Labview program, right click on the DAQ program box and select properties. Set the file save location to the folder created for this set of experiments
- j. Open the newly opened windows explorer window to the folder created for this set of experiments
- k. Arrange the relevant windows like those in Figure B9:

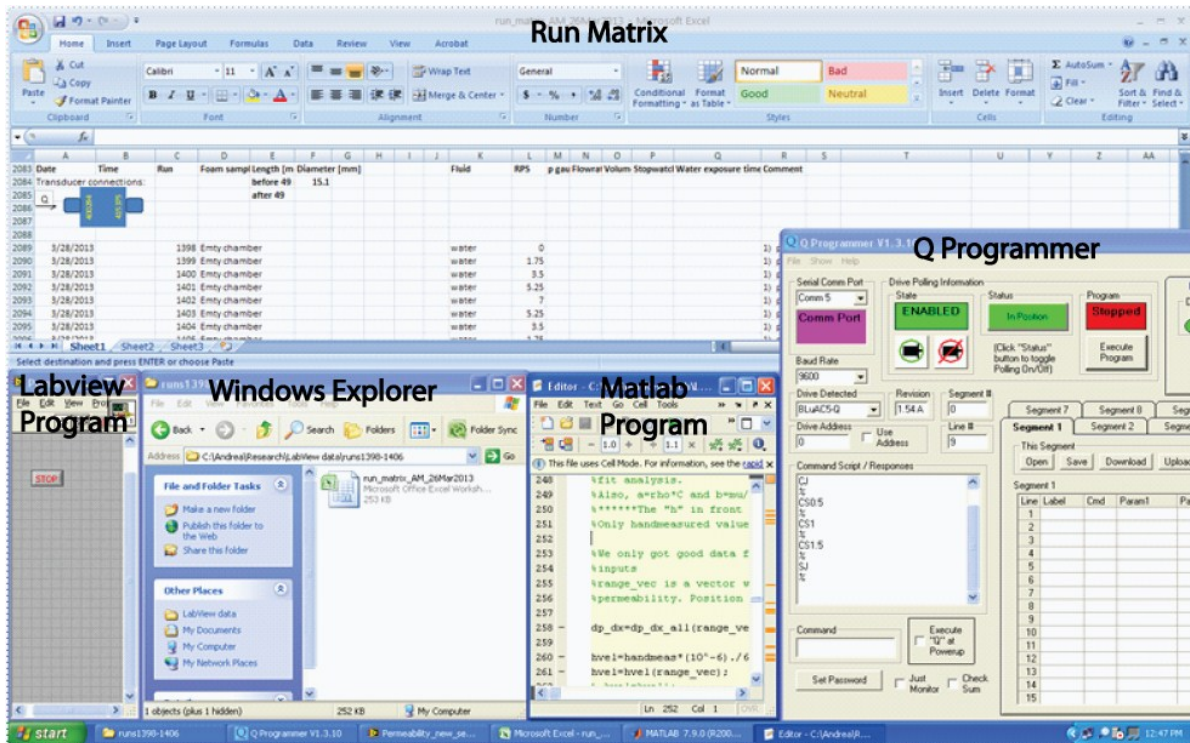


Figure B9. Windows of all programs that are utilized when collecting data.

2. Loading the sample (using chamber depicted in Figure B10)
 - a. Roll the 4 small o-rings (dash # 016) around the sample holder, one into each groove
 - b. Place the sample holder o-rings into the grooves located on one side of the testing chamber. Rotate the sample holder until the square openings in the sample holder are aligned with the pressure transducer ports on the outside of the chamber
 - c. Place the 3D gasket into grooves located along the length of the chamber side where the sample was inserted as depicted in the image below. To minimize possible leakages, put a layer of Teflon tape over top of the gasket length that

will be inside the chamber, leaving a short piece on the end that can wrap around the gasket on the outer surface of the chamber half as shown in Figure B10 below

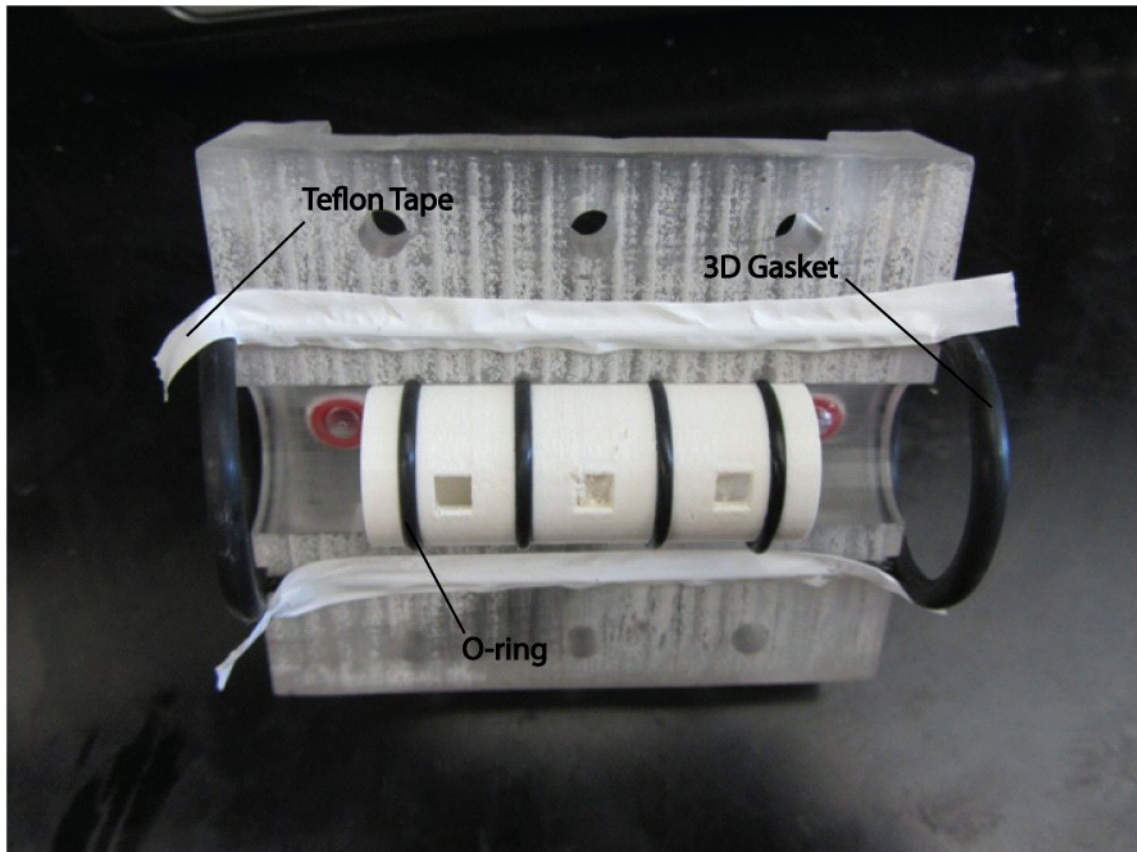


Figure B10. Application of Teflon tape over 3D gasket prior to chamber assembly to minimize possible leakages.

- d. Interlock the empty half of the testing chamber onto the side loaded with the sample and gasket. Wrap the protruding piece of Teflon tape around the gaskets located on the outer faces of the chamber. Place the screws that came

with the chamber into the center holes on opposite sides of the chamber and loosely tighten, just enough to hold the sides of the chamber together.

- e. Loosely tighten each of the other four screws after they are placed into their respective holes.
- f. Begin tightening each individual screw slowly, being careful to maintain a reasonably uniform amount of tightness in all screws. Continue tightening until all screws are secure. **Be careful not to over tighten as this could lead to cracking of the chamber.**
- g. Place the nozzles on the appropriate sides of the chamber body, with the inlet nozzle (marked with an 'I' in sharpie) on the inlet side of the sample. Make sure the excess Teflon is wrapped over the gasket.
- h. Attach screws in opposite corners on one nozzle and loosely tighten. Attach the other two screws and tighten to the same amount as the first two screws. Begin slowly tightening each screw until all screws are secure. Again, maintain a uniform amount of tightness in all screws. **Do not over tighten.**
- i. Repeat h for the nozzle on the other side of the chamber body.

Note: if the chamber is leaking it is likely because the screws are not tight enough. Adjust as necessary. It is best to tighten as required than breaking the chamber by over tightening it before loading it to the flow system, which will be discussed in the next subsection.

3. Attaching loaded chamber to flow system

- a. Begin by making sure which side of the chamber is the inlet. Position the chamber such that it can be accessed quickly for the next step.
- b. Open the upstream valve and wait for the water to fill the entire upstream tube. Take the inlet nozzle of the sample chamber and insert it into the upstream tubing, making sure that no air is left in the tube to form bubbles. Position the chamber vertically to remove bubbles, and gently tap the chamber if needed. Once there are no visible bubbles, bring the chamber back to a horizontal position and orient the pressure transducer openings parallel to the bench top surface as shown in Figure B11.
- c. Let the chamber fill up with water until it is coming out of the downstream nozzle.
- d. Partially open the downstream, valve to allow the water in the tubing connected to the reservoir to come out. Quickly insert the outlet nozzle of the chamber into the outlet tubing, being careful not to trap any air within the flow setup.
- e. Move the small black clamps into place around the tubing surrounding the nozzles on either side. There should be two clamps per nozzle. Use the channel locks to tighten the clamps into place. **Do not over tighten the clamps, as it might crack the chamber.**
- f. Fully open the downstream valve.

- g. Set the starting pump speed by typing in 'JS0.1' and hitting enter into the Q Programmer. This command instructs the motor to set the jogging speed at 0.1 revolutions per second (RPS). Then start the pump by typing 'SJ' into the Q Programmer (**make sure both the upstream and downstream valves are open!**). Slowly increase the speed of the pump by typing 'CS0.3' into the Q Programmer, then 'CS0.5', increasing until 'CS1.0' is reached.
- h. Wait until water begins to flow back into the fluid reservoir.
- i. Record the time at which the sample was fully exposed to water in the appropriate location in the run matrix
- j. Attach the pressure transducers to the quick connect adapters on the sides of the sample chamber, being sure to connect the upstream transducer to the upstream pressure port and the downstream pressure transducer to the downstream pressure port.
- k. Open the air bleed valves on the pressure transducers. Remove each one from its cradle and tap vigorously on the brass portions of the transducer with the channel locks to disturb air bubbles. Bubbles exiting the air bleed valve should be visible. Tap the T connectors and transducer lines to make sure all bubbles are being flushed out. Tilt the transducer in all directions while tapping to ensure removal of bubbles from all areas. Cover the air bleed valve outlet with a paper towel to "catch" the water. Doing this will avoid the transducer wiring from getting wet. Repeat this step for both transducers. Replace the transducers in the cradle and secure them in place. Close the air bleed valves.

l. Figure B11 shows the final assembled and connected chamber

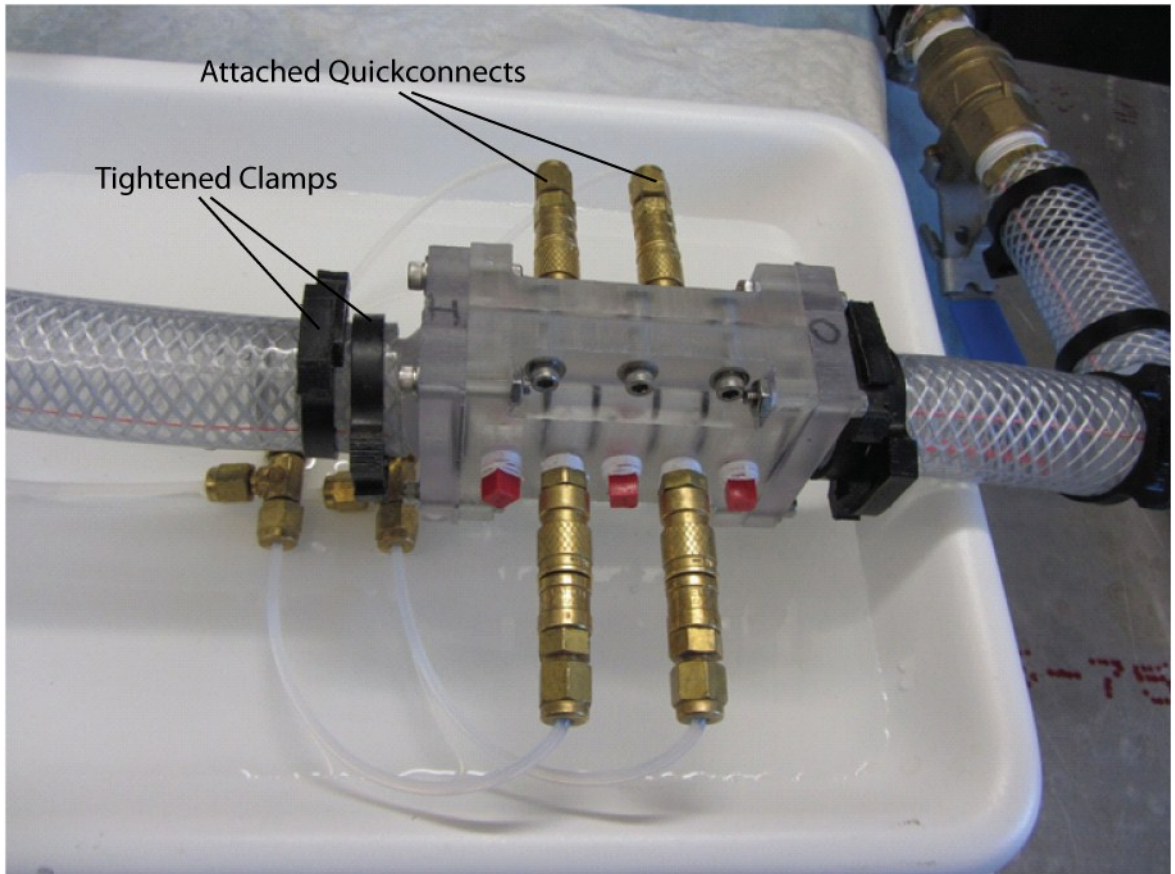


Figure B11. Assembled chamber in horizontal position after flushing air bubbles out.

m. Fill water reservoir up to black line on the side indicating standard filling height. Use RO water.

4. Find maximum motor speed
 - a. Slowly begin ramping up the motor speed (intervals of 0.1-0.5 RPS) by using the CS command in Q programmer (for a speed of 1.5, type 'CS1.5'). Continue ramping up the motor speed until the analog pressure gauge measures 2.5.
 - b. At this point start the Labview code by pressing the black arrow on the commands bar. A window will pop up asking you to input a file name. Save this file as test1. Allow the program to run for 10 seconds before pressing the red stop sign button on the Labview program.
 - c. Open the newly created file. In column F, row 24, make a formula to calculate the pressure being measured at the upstream transducer. Use the calibration equation supplied in line 71 of the Matlab code and the value in column C, row 24 as the voltage value (Do not use the part of the Matlab equation multiplying the sample by 6894.76, that is the conversion factor for Pascals, the equation entered should be $=0.488*V-0.08$, with V being the voltage found in the test page). This will give the pressure at the upstream transducer in pounds per square inch (psi). Copy the formula down column F to view the pressure measurements from each time point.
 - d. The number in column F will eventually need to be equal to 2.5. Most likely, after finding the motor speed that makes the analog pressure 2.5, the pressure will be well under 2.5 in the data taken. At this point, increase the motor speed in 0.1 RPS intervals until the upstream transducer reads a pressure of 2.5.

Note: 2.5 psi is the maximum pressure that both transducers can withstand. Do not go over this pressure.

- e. If the value is less than 2.5, increase the motor speed by a small amount. Repeat steps 4b and 4c, naming the file as test2, and once again finding the pressure in the test2 file.
- f. Repeat step e until the calculated pressure reading in the test is 2.5, making sure to name each new test in incremental order.
- g. Record the motor speed that produces this pressure in the run matrix as the RPS for the fifth run being performed. For the first and last runs the RPS value should be zero. For the second, third, and fourth runs, the RPS should be 0.25, 0.5, and 0.75 times the RPS of run 5 respectively. For the sixth, seventh, and eighth runs, the RPS values should be 0.75, 0.5, and 0.25 time the RPS of run 5 respectively.

5. Data Collection (1st run)

- a. Shut off the pump by gradually reducing the speed in Q Programmer by increments of 0.5 until the speed is less than 1, and then use the command 'SJ' to stop the pump.
- b. Close the upstream valve.
- c. Wait two minutes for the water to stabilize.

- d. Start the Labview program to collect data. Save the name of the file as the name of the run you are performing (e.g., for run 43 save it as '43'). Begin timing using a stopwatch as soon as the save box is closed.
- e. Record the time at which the run was started in the run matrix in the appropriate column (for example, 1:33 PM)
- f. Record the analog pressure gauge reading in the run matrix.
- g. Record the flow speed, volume measured, and time measured in (All should be 0 for the first run)
- h. Wait until 2 minutes have passed on the stopwatch. Do not stop the program until at least two minutes have passed.
- i. Stop the Labview program.
- j. Open the data file just created.
- k. Insert into row 22 a new row containing the headers contained in the headers file included in the attached files. Simply highlight the row in the headers file, hit control C, switch to the data file, select row 22 and right click on its number, and select insert copied cells.
- l. Click file, save as, excel workbook, and save the file with the same name as the original which will create a new Excel file.
- m. Run the Matlab code by hitting F5. If the data looks uniform continue to the next run. Otherwise repeat the current run.

6. Data Collection (2nd-8th runs)

- a. Start the pump by typing in JS followed by the RPS speed for the second run (for example, for a run speed of 0.5, type 'JS0.8') and hitting enter. Open the upstream valve to allow flow to pass through the sample and immediately afterwards type in CJ to commence running the motor.
- b. Take a beaker and a stop watch over to the outlet of the tubing into the fluid reservoir. Use the beaker to gather fluid, while timing for roughly ten seconds. Stop the stopwatch and pull the beaker out of the water stream simultaneously. Record the time from the stopwatch in the runmatrix in the appropriate column. Leave the beaker off to the side for now, filled with the gathered water.
- c. Start the Labview program, saving the file as the next run number. Immediately start the stopwatch.
- d. Record the time at which the run was started in the appropriate column.
- e. Pour the fluid from the beaker into a graduated cylinder. Record the volume of fluid in the run matrix in the appropriate column.
- f. The flow rate should be calculated in the appropriate column by dividing the volume of fluid by the time duration it was measured in, and dividing by 60, to give flow in mL/min.
- g. Record the analog pressure gauge reading in the appropriate column in the runmatrix.
- h. Change the Matlab code variable b to be the value of the latest run number.

- i. Wait until at least two minutes have passed on the stopwatch.
- j. Stop the Labview Program.
- k. Follow steps 5j through 5m
- l. Pour the fluid from the graduated cylinder back into the fluid reservoir
- m. Use CS to change the speed to the RPS for the next run.
- n. Repeat steps 6b through 6l for each run until the final run.

7. Data Collection (9th run)

- a. Stop the pump by typing in 'SJ' into the Q Programmer and hitting enter. Immediately close the upstream valve.
- b. Wait two minutes.
- c. Follow steps 5d through 5l
- d. On the second sheet of the runmatrix, make the make Column A rows 1 through 9, equal to the run numbers. In Column B and the same rows, make these cells equal to the flow rate for the corresponding run numbers. In column C and the same rows, make these cells equal to the RPS values for each associated run.
- e. Uncomment rows #41-44 and run the Matlab code by hitting F5.
- f. Once data is finished collecting, close the downstream valve, disconnect pressure transducers, close and secure the fluid reservoir, Undo clamps, and

remove chamber. Open the air bleed valve on the pressure transducers and allow the water to drain out.

8. Data Interpretation

- a. On execution of the Matlab code the final time, a graph showing the values for K and C will be displayed, along with their respective errors. An example graph is shown in Figure B12.

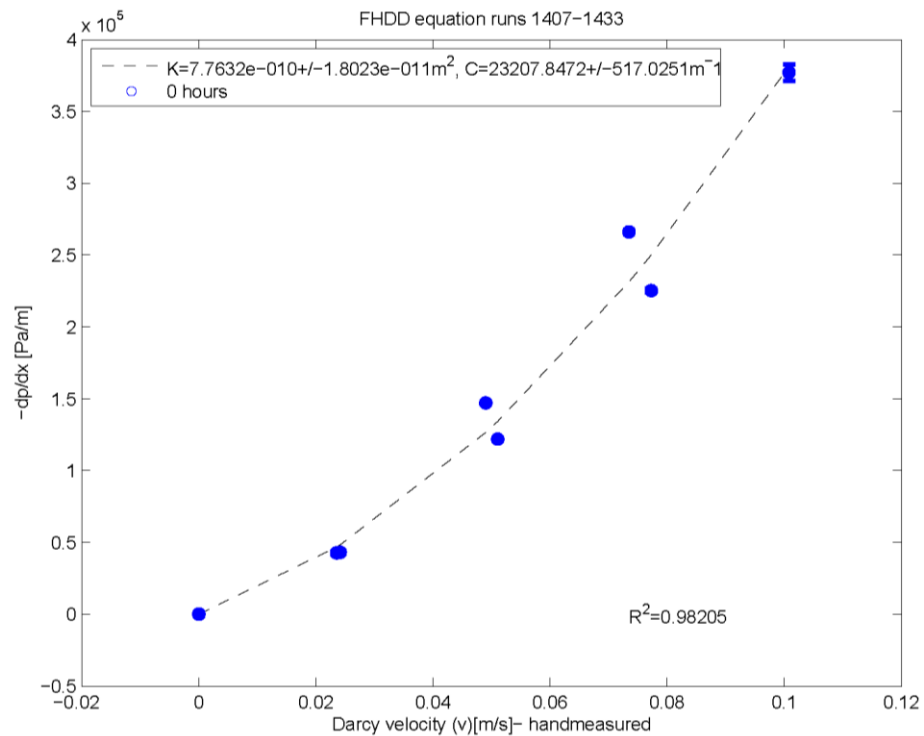


Figure B12. Example graph of FHDD equation showing values of permeability (K) and form factor (C).

- b. Each iteration of the Matlab code previously displayed the pressure readings for all runs taken up to that point. It is important to take note of any wild fluctuations or absurdly high or low values being calculated as this indicates an error in the setup or execution. Figure B13 is an example of a standard pressure reading graph during the runs (Upstream transducer has the higher pressure reading, in green):

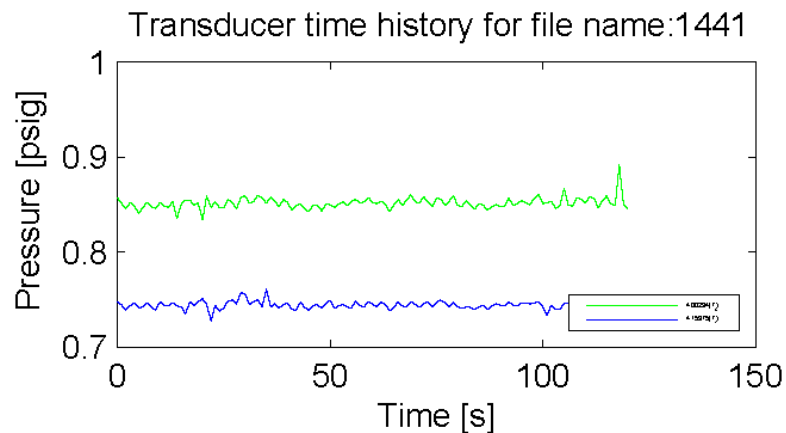


Figure B13. Example of standard pressure transducer time history showing the upstream transducer (green line) above the downstream transducer (blue line).

Matlab code

```
clc, close all, clear all
%% Define all variables:
%p- pressure, v- velocity, A- cross-sectional area, dx-length between
%pressure taps, K- permeability, C- form factor, f=-dp/dx
% From doing the least squares fit and uncertainty analysis, we fit the
```

```

% function  $f=-dp/dx=(\mu/K)*v+\rho*C*v^2$  with the line  $fc=a*v^2+b*v$ . We find
% the constants a and b, and then calculate permeability and form factor
as
%  $K=\mu/b$ ,  $C=a/\rho$ .
%Transducers will be labeled as follows:
%T_3=400294 wire label 1, excel column 3, daq slot 1, upstream
%T_1=415375 wire label 3, excel column 5, daq slot 3, downstream

%Calibration curves as of after the move:
%Transducer S/N 59813:  $P[\text{psi}]=2.3182*\text{voltage}[V]-15.0383$ 
%Transducer S/N 59815:  $P[\text{psi}]=2.3278*\text{voltage}[V]-14.4580$ 

%*****CHANGE EACH TIME*****

% Do a loop to import raw data
%set range of file names:
a=run#x;
b=run#x+ $\Delta x$ ;

%This is the diameter of the black plastic insert piece that goes inside
%the chamber. Be sure to change this value if the diameter is altered to
%get a tighter foam fit. The units are m.
%Alternatively, if using the GDC chamber, this is the inner diameter of
the
%chamber, which is 0.006 m.
insert_diameter=0.0151;

%dx is the length from the first to the last pressure tap. This value
%should be used depending on the chamber used. The new permeability
%chamber is  $dx=0.03$  m and the gdc chamber is  $dx=0.05$  m.
dx=0.015; %m

%Enter filename of the run matrix
str2='run_matrix_Initials_DayMonthYear.xlsx';

% % Using hand measured flow rates instead of the transducer:
data2=xlsread(str2,'sheet2');
handmeas=data2(1:9,2); %*edit to the correct rows/columns of the hand
range_vec=[1:9];
rps_vals=data2(1:9,3);
%*****

%Multiple files

for i=a:b;
str= strcat(int2str(i),'.xlsx');
eval('data=xlsread(str);');

%time is in column 1,transducer 400294 voltage in column 3, and transducer
%415275 voltage in column 5. In the annotated files, the header ends in
row
%23, however, this code will consider data starting at row 22, because
%there is an empty row in the file as exported from labview that matlab
%doesn't count. Take the average of the first 120 seconds.

```

```

time=data(23:143,1); %seconds
T_1_V(i)=mean(data(23:143,5)); %Volts
% T_2_V(i)=mean(data(23:143,4)); %Volts
T_3_V(i)=mean(data(23:143,3)); %Volts
%Get actual flowrate and pressure values:

%Transducer S/N 400335: P[psi]=0.479*voltage[V]-0.030
%Transducer S/N 400294: P[psi]=0.488*voltage[V]-0.08
%Transducer S/N 415375: P[psi]=0.479*voltage[V]-0.037

%Calibration fit for the 0-2 psig transducers:
% T_2(i)=(0.479.*T_2_V(i)-0.030)*6894.76; %Pa
T_3(i)=(0.488.*T_3_V(i)-0.08)*6894.76; %Pa, upstream transducer
T_1(i)=(0.479.*T_1_V(i)-0.037)*6894.76; %Pa, downstream transducer

%f is the vector containing pressure gradient, i.e. T_3-T_1/length.

A=pi*(0.5*insert_diameter)^2; %m^2

%get zero values
f_zero=(T_3(a)-T_1(a))/dx; %Pa/m
f(i)=((T_3(i)-T_1(i))./dx)-f_zero; %Pa/m

%Plot transducers' voltage history for all runs:
if i<(a+6)
    figure (1)
    subplot(3,2,i-a+1)
    plot(time,(0.479.*data(23:143,3)-0.037),'g','LineWidth',0.5)
    str='Transducer time history for file name: ';
    title([str num2str(i)])
    xlabel('Time [s]')
    ylabel(' Pressure [psig]')
    hold on
%    plot(time,(0.479.*data(23:143,4)-0.030),'r','LineWidth',0.5)
    plot(time,(0.488.*data(23:143,5)-0.08),'r','LineWidth',0.5)
    h_legend=legend('400294(T_3)', '415375(T_1)', 'Location', 'SouthEast');
    set(h_legend, 'FontSize', 2);
    hold off
    print('-dpdf', 'runsa_b_transducer_time_history_1.pdf')
elseif (a+6)<=i&&i<(a+12)
    figure (2)
    subplot(3,2,i-a-5)
    plot(time,(0.479.*data(23:143,3)-0.037),'g','LineWidth',0.5)
    str='Transducer time history for file name: ';
    title([str num2str(i)])
    xlabel('Time [s]')
    ylabel(' Pressure [psig]')
    hold on
%    plot(time,(0.479.*data(23:143,4)-0.030),'r','LineWidth',0.5)
    plot(time,(0.488.*data(23:143,5)-0.08),'r','LineWidth',0.5)
    h_legend=legend('400294(T_3)', '415375(T_1)', 'Location', 'SouthEast');
    set(h_legend, 'FontSize', 2);
    hold off
    print('-dpdf', 'runsa_b_transducer_time_history_2.pdf')

```



```

elseif (a+12)<=i&&i<(a+18)
    figure (3)
    subplot(3,2,i-a-11)
    plot(time,(0.479.*data(23:143,3)-0.037),'g','LineWidth',0.5)
    str='Transducer time history for file name: ';
    title([str num2str(i)])
    xlabel('Time [s]')
    ylabel(' Pressure [psig]')
    hold on
%   plot(time,(0.479.*data(23:143,4)-0.030),'r','LineWidth',0.5)
    plot(time,(0.488.*data(23:143,5)-0.08),'r','LineWidth',0.5)
    h_legend=legend('400294(T_3)','415375(T_1)','Location','SouthEast');
    set(h_legend,'FontSize',2);
    hold off
        print('-dpdf','runs1407_1433_transducer_time_history_3.pdf')
elseif (a+18)<=i&&i<(a+24)
    figure (4)
    subplot(3,2,i-a-17)
    plot(time,(0.479.*data(23:143,3)-0.037),'g','LineWidth',0.5)
    str='Transducer time history for file name: ';
    title([str num2str(i)])
    xlabel('Time [s]')
    ylabel(' Pressure [psig]')
    hold on
%   plot(time,(0.479.*data(23:143,4)-0.030),'r','LineWidth',0.5)
    plot(time,(0.488.*data(23:143,5)-0.08),'r','LineWidth',0.5)
    h_legend=legend('400294(T_3)','415375(T_1)','Location','SouthEast');
    set(h_legend,'FontSize',2);
    hold off
        print('-dpdf','runsa_b_transducer_time_history_4.pdf')
elseif (a+24)<=i&&i<(a+30)
    figure (5)
    subplot(3,2,i-a-23)
    plot(time,(0.479.*data(23:143,3)-0.037),'g','LineWidth',0.5)
    str='Transducer time history for file name: ';
    title([str num2str(i)])
    xlabel('Time [s]')
    ylabel(' Pressure [psig]')
    hold on
%   plot(time,(0.479.*data(23:143,4)-0.030),'r','LineWidth',0.5)
    plot(time,(0.488.*data(23:143,5)-0.08),'r','LineWidth',0.5)
    h_legend=legend('400294(T_3)','415375(T_1)','Location','SouthEast');
    set(h_legend,'FontSize',2);
    hold off
        print('-dpdf','runsa_b_transducer_time_history_5.pdf')
elseif (a+30)<=i&&i<(a+36)
    figure (6)
    subplot(3,2,i-a-29)
    plot(time,(0.479.*data(23:143,3)-0.037),'g','LineWidth',0.5)
    str='Transducer time history for file name: ';
    title([str num2str(i)])
    xlabel('Time [s]')
    ylabel(' Pressure [psig]')
    hold on
%   plot(time,(0.479.*data(23:143,4)-0.030),'r','LineWidth',0.5)
    plot(time,(0.488.*data(23:143,5)-0.08),'r','LineWidth',0.5)
    h_legend=legend('400294(T_3)','415375(T_1)','Location','SouthEast');

```

```

    set(h_legend, 'FontSize', 2);
    hold off
        print('-dpdf', 'runsa_b_transducer_time_history_6.pdf')
elseif (a+36)<=i&&i<(a+42)
    figure (7)
    subplot(3,2,i-a-35)
    plot(time, (0.479.*data(23:143,3)-0.037), 'g', 'LineWidth', 0.5)
    str='Transducer time history for file name: ';
    title([str num2str(i)])
    xlabel('Time [s]')
    ylabel(' Pressure [psig]')
    hold on
%     plot(time, (0.479.*data(23:143,4)-0.030), 'r', 'LineWidth', 0.5)
    plot(time, (0.488.*data(23:143,5)-0.08), 'LineWidth', 0.5)
h_legend=legend('400294(T_3)', '415375(T_1)', 'Location', 'SouthEast');
set(h_legend, 'FontSize', 2);
hold off
    print('-dpdf', 'runsa_b_transducer_time_history_7.pdf')
else
    figure (8)
    subplot(3,2,i-a-41)
    plot(time, (0.479.*data(23:143,3)-0.037), 'g', 'LineWidth', 0.5)
    str='Transducer time history for file name: ';
    title([str num2str(i)])
    xlabel('Time [s]')
    ylabel(' Pressure [psig]')
    hold on
%     plot(time, (0.479.*data(23:143,4)-0.030), 'r', 'LineWidth', 0.5)
    plot(time, (0.488.*data(23:143,5)-0.08), 'LineWidth', 0.5)
h_legend=legend('400294(T_3)', '415375(T_1)', 'Location', 'SouthEast');
set(h_legend, 'FontSize', 2);
hold off
    print('-dpdf', 'runsa_b_transducer_time_history_8.pdf')
end

end

rho=1000; %kg/m^3
mu=0.00112; %Pa*s
dp_dx_all=f(a:b); %Pa/m
dp_dx=f(a:b);

figure(17)
scatter(a:linspace(a,b,1), dp_dx.*dx./6894.76)
title('Pressure drop as a function of run#')
xlabel('Run #')
ylabel('Pressure -(dP-dP_0) [psig]')
hold on
plot(a:linspace(a,b,1), dp_dx.*dx./6894.76)
hold off
    print('-dpdf', 'runsa_b_pressure_drop.pdf')

% *****
% measured data
handmeas=handmeas';

```



```

%plot dp_dx vs velocity, and add sigma_dp_dx
rps_vec_hys=rps_vec(runs_hys);
p1_hys=T_1(runs_hys);
p3_hys=T_3(runs_hys);
%If max RPS value was not measured twice
for i=1:(length(p1_hys)-1)/2;
    dif_p1(i)=(p1_hys(i)-(p1_hys(length(p1_hys)+1-i)));
    dif_p3(i)=(p3_hys(i)-(p3_hys(length(p1_hys)+1-i)));
end
sigma_rep=mean(abs([dif_p1,dif_p3]));
% 2. Get sigma_bias and sigma_prec
for i=a:b;
    %reload all data
    str= strcat(int2str(i),'.xlsx');
    eval('data=xlsread(str);');
    eval(['data' num2str(i) '=data']);
    eval(['T_1' num2str(i) '=','(data' ,num2str(i),'(23:143,5)*0.479-
0.037)*6894.76']);%Pa
    eval(['T_2' num2str(i) '=','(data' ,num2str(i),'(23:143,4)*0.479-
0.03)*6894.76']);%Pa
    eval(['T_3' num2str(i) '=','(data' ,num2str(i),'(23:143,3)*0.488-
0.08)*6894.76']);%Pa
    %Uncertainty
    %sigma_bias=0.1/100*mean(120readings)
    eval(['sigma_bias_1(i)=0.1/100*mean(T_1_' num2str(i) ' ')]);
    eval(['sigma_bias_2(i)=0.1/100*mean(T_2_' num2str(i) ' ')]);
    eval(['sigma_bias_3(i)=0.1/100*mean(T_3_' num2str(i) ' ')]);
    %for zero values
    eval(['sigma_bias_1_zero=0.1/100*mean(T_1_' num2str(a) ' ')]);
    eval(['sigma_bias_2_zero=0.1/100*mean(T_2_' num2str(a) ' ')]);
    eval(['sigma_bias_3_zero=0.1/100*mean(T_3_' num2str(a) ' ')]);

for n=1:120;

eval(['dif_T_1_' num2str(i) ' (n)=(T_1_' num2str(i) ' (n)-mean(T_1_'
num2str(i) ' ')).^2']);
eval(['dif_T_2_' num2str(i) ' (n)=(T_2_' num2str(i) ' (n)-mean(T_2_'
num2str(i) ' ')).^2']);
eval(['dif_T_3_' num2str(i) ' (n)=(T_3_' num2str(i) ' (n)-mean(T_3_'
num2str(i) ' ')).^2']);
%for zero values
eval(['dif_T_1_zero=(T_1_' num2str(a) ' -mean(T_1_' num2str(a) ' ')).^2']);
eval(['dif_T_2_zero=(T_2_' num2str(a) ' -mean(T_2_' num2str(a) ' ')).^2']);
eval(['dif_T_3_zero=(T_3_' num2str(a) ' -mean(T_3_' num2str(a) ' ')).^2']);
end

% +/-tv,95*sx/sqrt(N). Use t=1.9801 (infinite degrees of freedom), check
t=1.9801;
eval(['sigma_prec_1(i)=t.*sqrt(1/(120-1).*sum(dif_T_1_' num2str(i)
'))/sqrt(120)']);
eval(['sigma_prec_2(i)=t.*sqrt(1/(120-1).*sum(dif_T_2_' num2str(i)
'))/sqrt(120)']);
eval(['sigma_prec_3(i)=t.*sqrt(1/(120-1).*sum(dif_T_3_' num2str(i)
'))/sqrt(120)']);
%for zero values

```

```

eval(['sigma_prec_1_zero=t.*sqrt(1/(120-
1).*sum(dif_T_1_zero))/sqrt(120)']);
eval(['sigma_prec_2_zero=t.*sqrt(1/(120-
1).*sum(dif_T_2_zero))/sqrt(120)']);
eval(['sigma_prec_3_zero=t.*sqrt(1/(120-
1).*sum(dif_T_3_zero))/sqrt(120)']);

% Now we get sigma_p for each run, for each transducer.

sigma_p_1(i)=sqrt(sigma_bias_1(i)^2 + sigma_prec_1(i)^2 );
sigma_p_2(i)=sqrt(sigma_bias_2(i)^2 + sigma_prec_2(i)^2 );
sigma_p_3(i)=sqrt(sigma_bias_3(i)^2 + sigma_prec_3(i)^2 );
%for zero values
sigma_p_1_zero=sqrt(sigma_bias_1_zero^2+sigma_prec_1_zero^2);
sigma_p_2_zero=sqrt(sigma_bias_2_zero^2+sigma_prec_2_zero^2);
sigma_p_3_zero=sqrt(sigma_bias_3_zero^2+sigma_prec_3_zero^2);
end

sigma_p_1=sigma_p_1(a:b);
sigma_p_2=sigma_p_2(a:b);
sigma_p_3=sigma_p_3(a:b);
sigma_dp=sqrt(sigma_p_1.^2+sigma_p_1_zero.^2+sigma_p_3.^2+sigma_p_3_zero.^
2);
sigma_dp_dx=1/dx.*sigma_dp;

%Select only the numbers that are considered in permeability calculation
%using range_vec:
sigma_dp_dx=sigma_dp_dx(range_vec);

%%Calculating K and C with uncertainty:
%with handmeasured values:
par_ha=(sum((hvel.*dp_dx)./sigma_dp_dx.^2)./sum(hvel.^2./sigma_dp_dx.^2)-
((sum((hvel.^2.*dp_dx)./sigma_dp_dx.^2).*sum(hvel.^3./sigma_dp_dx.^2))./(s
um(hvel.^2./sigma_dp_dx.^2).*sum(hvel.^4./sigma_dp_dx.^2))))./(1-
(sum(hvel.^3./sigma_dp_dx.^2).^2./(sum(hvel.^2./sigma_dp_dx.^2).*sum(hvel.
^4./sigma_dp_dx.^2))));
hK=mu./par_ha;
par_hb=(sum((hvel.^2.*dp_dx)./sigma_dp_dx.^2)-
par_ha.*sum(hvel.^3./sigma_dp_dx.^2))./sum(hvel.^4./sigma_dp_dx.^2);
hC=1/rho.*par_hb;

%calculation of sigma_K and sigma_C: (da stands for partial of a wrt y).
%All variables with h are for handmeasured values

for i=1:length(range_vec);
dhK_df(i)=-
mu.*(sum(hvel.^2./sigma_dp_dx.^2).*sum(hvel.^4./sigma_dp_dx.^2)-
(sum(hvel.^3./sigma_dp_dx.^2)).^2).*sum(hvel(i)./sigma_dp_dx(i).^2.*sum(hvel.
^4./sigma_dp_dx.^2)-
hvel(i).^2./sigma_dp_dx(i).^2.*sum(hvel.^3./sigma_dp_dx.^2))./(sum(hvel.*d
p_dx./sigma_dp_dx.^2).*sum(hvel.^4./sigma_dp_dx.^2)-
sum(hvel.^2.*dp_dx./sigma_dp_dx.^2).*sum(hvel.^3./sigma_dp_dx.^2)).^2;
dha(i)=(hvel(i)./sigma_dp_dx(i).^2.*sum(hvel.^4./sigma_dp_dx.^2)-
hvel(i).^2./sigma_dp_dx(i).^2.*sum(hvel.^3./sigma_dp_dx.^2))./(sum(hvel.^2

```

```

./sigma_dp_dx.^2).*sum(hvel.^4./sigma_dp_dx.^2)-
(sum(hvel.^3./sigma_dp_dx.^2)).^2);
dhC_df(i)=1./rho.*(hvel(i).^2./sigma_dp_dx(i).^2-
dha(i).*sum(hvel.^3./sigma_dp_dx.^2))./sum(hvel.^4./sigma_dp_dx.^2);
end
sigma_hK=sqrt(sum((dhK_df.*sigma_dp_dx).^2));
sigma_hC=sqrt(sum((dhC_df.*sigma_dp_dx).^2));

%hz becomes a vector containing the calculated dp_dx values
hz=(mu./hK.*hvel)+(rho.*hC.*hvel.^2); %if using handmeasured data

% Correlation for non-linear regression
% error vector e=observed values (dp_dx)- fitted values (hz)
% SSE, sum of squared errors. SSE=summation(dp_dxi-hzi)^2
% SST, sum of squared totals. SST=summation(dp_dxi-average(dp_dx))^2.
% R^2=1-SSE/SST.
hRsq=1-(sum((dp_dx-hz).^2)/sum((dp_dx-mean(dp_dx)).^2));
hRsq2=(sum(hz.*dp_dx)-
(sum(hz)*sum(dp_dx))/length(dp_dx))/sqrt((sum(hz.^2)-
(sum(hz))^2/length(hz))*(sum(dp_dx.^2)-(sum(dp_dx))^2/length(dp_dx))))^2;

figure (11)
plot(sort(hvel),sort(hz),'--k')
hold on
aerrorbar=errorbar(hvel(1:9),dp_dx(1:9),sigma_dp_dx(1:9),'ob')
berrorbar=errorbar(hvel(10:18),dp_dx(10:18),sigma_dp_dx(10:18),'sr')
cerrorbar=errorbar(hvel(19:27),dp_dx(19:27),sigma_dp_dx(19:27),'^g')
set(aerrorbar,'MarkerSize',5,'LineWidth',2)
set(berrorbar,'MarkerSize',5,'LineWidth',2)
set(cerrorbar,'MarkerSize',5,'LineWidth',2)
title('FHDD equation runs a-b')
xlabel('Darcy velocity (v) [m/s]- handmeasured')
ylabel('-dp/dx [Pa/m]')
str='K='
unc='+/-'
sstr='m^2, C='
uncc='+/-'
strrr='m^-1'
h_legend=legend([str num2str(hK) unc num2str(sigma_hK) strr num2str(hC)
uncc num2str(sigma_hC) strrr], '0 hours','2 hours','4
hours','Location','NorthWest')
set(h_legend,'FontSize',10)
text(hvel(4),0,['R^2=' num2str(hRsq)])
print('-dpdf','FHDD_eq_runsa_b_errorbars.pdf')

% % get all values in a matrix:
runsnum=['runs' num2str(a) '_' num2str(b) '.xls'];
labels1={'dp_dx [Pa/m]', 'sigma_dp_dx [Pa/m]', 'hvel [m/s]'};
labels2={'hK [m^2]' 'sigma_hK [m^2]' 'hC [m^-1]' 'sigma_hC [m^-1]'};
HDD_vals=[dp_dx',sigma_dp_dx',hvel'];
KC_vals=[hK, sigma_hK, hC, sigma_hC];
xlswrite(runsnum, HDD_vals, 1, 'A5');
xlswrite(runsnum, KC_vals,1, 'A2');
xlswrite(runsnum, labels1, 1, 'A4');
xlswrite(runsnum, labels2, 1, 'A1');

```

Least squares fit and uncertainty analysis calculation

Starting with the generalized Forcheimer-Hazen-Dupuit-Darcy Equation:

$$y_p = ax + bx^2 \quad (\text{B2})$$

With $y_p = \frac{\Delta P}{\Delta x}$, and $x = v$, where $\frac{\Delta P}{\Delta x}$ is the particular pressure gradient and v is the Darcy velocity, the method of least squares was used to calculate the values of a and b . In order to perform the least squares fit analysis, the variable D was defined as:

$$D = \sum [y_i - y_p]^2 \quad (\text{B3})$$

The least squares fit analysis utilizes that the partial derivative of D^2 with respect to a and b must be zero, which allows for a and b to be calculated:

$$\frac{\delta}{\delta a} D^2 = \frac{\delta}{\delta a} \sum_{i=1}^n \left[\frac{1}{\sigma_i} (y_i - ax_i - bx_i^2) \right]^2 = 0 \quad (\text{B4})$$

$$\frac{\delta}{\delta b} D^2 = \frac{\delta}{\delta b} \sum_{i=1}^n \left[\frac{1}{\sigma_i} (y_i - ax_i - bx_i^2) \right]^2 = 0 \quad (\text{B5})$$

With σ_i being the standard deviation of the pressure gradient at the index i . Solving these equations for a and b yields:

$$a = \frac{\sum \left[\frac{x_i y_i}{\sigma_i^2} \right] \sum \left[\frac{x_i^4}{\sigma_i^2} \right] - \sum \left[\frac{x_i^2 y_i}{\sigma_i^2} \right] \sum \left[\frac{x_i^3}{\sigma_i^2} \right]}{\sum \left[\frac{x_i^2}{\sigma_i^2} \right] \sum \left[\frac{x_i^4}{\sigma_i^2} \right] - \left(\sum \left[\frac{x_i^3}{\sigma_i^2} \right] \right)^2} \quad (\text{B6})$$

$$b = \frac{\sum \left[\frac{x_i^2 y_i}{\sigma_i^2} \right] - a \sum \left[\frac{x_i^3}{\sigma_i^2} \right]}{\sum \left[\frac{x_i^4}{\sigma_i^2} \right]} \quad (\text{B7})$$

The material constants that we are interested in for our study, K and C , can be determined by the following formulas:

$$K = \frac{\mu}{a} , \quad (\text{B8})$$

and

$$C = \frac{b}{\rho} . \quad (\text{B9})$$

The uncertainty in any given function $z=m+q+\dots+n$ is calculated by computing

$$\sigma_z = \sqrt{\left(\frac{\partial z}{\partial m} \sigma_m\right)^2 + \left(\frac{\partial z}{\partial q} \sigma_q\right)^2 \dots + \left(\frac{\partial z}{\partial n} \sigma_n\right)^2} . \quad (\text{B10})$$

Following this method, the uncertainty in each pressure measurement is calculated. This is the compound uncertainty resulting from bias (0.1% reading) and precision (standard deviation with $t=1.9801$, for unlimited degrees of freedom) errors in each transducer, yielding:

$$\sigma_P = \sqrt{\sigma_{Bias}^2 + \sigma_{Precision}^2} . \quad (\text{B11})$$

The difference in pressure between the upstream and downstream transducer is calculated as follows:

$$\Delta P = P_{2,n} - P_{2,0} - P_{1,n} + P_{1,0} , \quad (\text{B12})$$

where the first subscript is the position of the transducer (1=upstream, 2=downstream) and the second subscript is the reading of the transducer (0= the reading at zero velocity). Thus

$$\sigma_{\Delta P} = \sqrt{\sigma_{P_{2,n}}^2 + \sigma_{P_{2,0}}^2 + \sigma_{P_{1,n}}^2 + \sigma_{P_{1,0}}^2} . \quad (\text{B13})$$

The uncertainty in the pressure gradient is

$$\sigma_{\frac{\Delta P}{\Delta x}} = \sqrt{\left(\frac{\partial \frac{\Delta P}{\Delta x}}{\partial \Delta P} \sigma_{\Delta P}\right)^2 + \left(\frac{\partial \frac{\Delta P}{\Delta x}}{\partial \Delta x} \sigma_{\Delta x}\right)^2} , \quad (\text{B14})$$

where the second term to the right under the square root is zero assuming there is no uncertainty in the measurement of Δx because this distance was machined precisely using a CNC.

To calculate the uncertainty in K and C, it is required to first compute the partial derivatives of K and C with respect to y:

$$\frac{\partial K}{\partial y_j} = -\mu \frac{\left(\Sigma \left[\frac{x_i^2}{\sigma_i^2} \right] \Sigma \left[\frac{x_i^4}{\sigma_i^2} \right] - \left(\Sigma \left[\frac{x_i^3}{\sigma_i^2} \right] \right)^2 \right) \left(\frac{x_j}{\sigma_j^2} \Sigma \left[\frac{x_i^4}{\sigma_i^2} \right] - \frac{x_j^2}{\sigma_j^2} \Sigma \left[\frac{x_i^3}{\sigma_i^2} \right] \right)}{\left(\Sigma \left[\frac{x_i y_i}{\sigma_i^2} \right] \Sigma \left[\frac{x_i^4}{\sigma_i^2} \right] - \Sigma \left[\frac{x_i^2 y_i}{\sigma_i^2} \right] \Sigma \left[\frac{x_i^3}{\sigma_i^2} \right] \right)^2}, \quad (\text{B15})$$

$$\frac{\partial C}{\partial y_j} = \frac{1}{\rho} \frac{\left(\frac{x_j^2}{\sigma_j^2} \frac{\partial a}{\partial y_j} \right) \Sigma \left[\frac{x_i^3}{\sigma_i^2} \right]}{\Sigma \left[\frac{x_i^4}{\sigma_i^2} \right]}, \quad (\text{B16})$$

where the partial derivative of a with respect to y is:

$$\frac{\partial a}{\partial y_j} = \frac{\frac{x_j}{\sigma_j^2} \Sigma \left[\frac{x_i^4}{\sigma_i^2} \right] - \frac{x_j^2}{\sigma_j^2} \Sigma \left[\frac{x_i^3}{\sigma_i^2} \right]}{\Sigma \left[\frac{x_i^2}{\sigma_i^2} \right] \Sigma \left[\frac{x_i^4}{\sigma_i^2} \right] - \left(\Sigma \left[\frac{x_i^3}{\sigma_i^2} \right] \right)^2}. \quad (\text{B17})$$

Finally, from Eq. A10

$$\sigma_K = \sqrt{\Sigma \left[\left(\frac{\partial K}{\partial y_j} \sigma_{y_j} \right)^2 \right]}, \quad (\text{B18})$$

and

$$\sigma_c = \sqrt{\sum \left[\left(\frac{\partial c}{\partial y_j} \sigma_{y_j} \right)^2 \right]}. \quad (\text{B19})$$